Astronomy & Astrophysics

The GAPS Programme at TNG

XXXV. Fundamental properties of transiting exoplanet host stars[*]

K. Biazzo[1], V. D'Orazi[2], S. Desidera[2], D. Turrini[3,9], S. Benatti[4], R. Gratton[2], L. Magrini[5],
A. Sozzetti[3], M. Baratella[6], A. S. Bonomo[3], F. Borsa[7], R. Claudi[2], E. Covino[8], M. Damasso[3],
M. P. Di Mauro[9], A. F. Lanza[10], A. Maggio[4], L. Malavolta[11,2], J. Maldonado[4], F. Marzari[11],
G. Micela[4], E. Poretti[12,7], F. Vitello[13], L. Affer[4], A. Bignamini[14], I. Carleo[15], R. Cosentino[12], A. F. M. Fiorenzano[12],
P. Giacobbe[3], A. Harutyunyan[12], G. Leto[10], L. Mancini[16], E. Molinari[17], M. Molinaro[14], D. Nardiello[2], V. Nascimbeni[2],
I. Pagano[10], M. Pedani[12], G. Piotto[11], M. Rainer[7], and G. Scandariato[10]

(Affiliations can be found after the references)

ABSTRACT

Context. Exoplanetary properties strongly depend on stellar properties: to know the planet with accuracy and precision it is necessary to know the star as accurately and precisely as possible.

Aims. Our immediate aim is to characterize in a homogeneous and accurate way a sample of 27 transiting planet-hosting stars observed within the Global Architecture of Planetary System program. For the wide visual binary XO-2, we considered both components (N: hosting a transiting planet; S: without a known transiting planet). Our final goal is to widely analyze the sample by deriving several stellar properties, abundances of many elements, kinematic parameters, and discuss them in the context of planetary formation.

Methods. We determined the stellar parameters (effective temperature, surface gravity, rotational velocity) and abundances of 26 elements (Li, C, N, O, Na, Mg, Al, Si, S, Ca, Sc, Ti, V, Cr, Fe, Mn, Co, Ni, Cu, Zn, Y, Zr, Ba, La, Nd, Eu). Our study is based on high-resolution HARPS-N at TNG and FEROS at ESO spectra and uniform techniques. Depending on stellar parameters and chemical elements, we used line equivalent widths or spectral synthesis methods. We derived kinematic properties taking advantage of *Gaia* data and for the first time in exoplanet host stars we estimated ages using elemental ratios as chemical clocks.

Results. The effective temperature of our stars is ~4400–6700 K, while the iron abundance [Fe/H] is within −0.3 and 0.4 dex. Lithium is present in seven stars. The [X/H] and [X/Fe] abundances versus [Fe/H] are consistent with the Galactic chemical evolution. The dependence of [X/Fe] with the condensation temperature is critically analyzed with respect to stellar and kinematic properties. All targets with measured C and O abundances show C/O < 0.8, compatible with Si present in rock-forming minerals. Mean C/O and [C/O] values are slightly lower than for the Sun. Most of targets show 1.0 < Mg/Si < 1.5, compatible with Mg distributed between olivine and pyroxene, and mean Mg/Si lower than for the Sun. HAT-P-26, the target hosting the lowest-mass planet, shows the highest Mg/Si ratio. From our chemodynamical analysis we find agreement between ages and position within the Galactic disk. Finally, we note a tendency for higher-density planets to be around metal-rich stars and hints of higher stellar abundances of some volatiles (e.g., O) for lower-mass planets. We cannot exclude that part of our results could be also related to the location of the stars within the Galactic disk.

Conclusions. We try to trace the planetary migration scenario from the composition of the planets related to the chemical composition of the hosting stars. This kind of study will be useful for upcoming space mission data to get more insights into the formation–migration mechanisms.

Key words. stars: abundances – stars: fundamental parameters – techniques: spectroscopic – planetary systems

1. Introduction

Until around ten years ago many of the known extrasolar planets were revealed by the use of Doppler radial velocity (RV). Alone, the RVs only yield partial information on orbital elements of the planets and their minimum masses, and no insight is obtained about the planetary physical properties, like their true masses, radii, and mean densities. This additional information is available in the case of planetary transits. In recent years, major

planet-search programs using the photometric transit technique started to deliver interesting results, giving new impetus to the study of exoplanets. Now, the known transiting extrasolar planets are growing in number, giving us information about the physical properties of orbiting planets. Complementary follow-up observations of the transits have further permitted us access to the atmospheres of these worlds, giving important clues about the physics of these atmospheres (see, e.g., Charbonneau et al. 2002; Madhusudhan 2019, and references therein). Therefore, transiting exoplanets provide us with unique laboratories to test theories of exoplanet formation and evolution with relatively high precision.

When deriving properties for a statistically significant sample of exoplanets, a precise and homogeneous determination of the stellar parameters is crucial for an accurate characterization

---

of the parent stars and, in turn, of the planet properties. The connection between star and planet is perpetually interweaved, so one cannot be studied without accounting for the other. For instance, when the planet is transiting, it is possible to have hints of the internal planetary structure and the gas and/or ice and/or rock ratios from the bulk planetary density. However, the required accurate estimates of planetary mass and radius and density necessarily rely on precise determination of mass and radius of the hosting star. The derivation of stellar mass (and radius) is strongly connected to the effective temperature (T_{eff}), surface gravity ($\log g$), and iron abundance ([Fe/H]) of the star, and is also dependent on the evolutionary tracks considered. Therefore, planetary properties are critically dependent on the properties of the hosting stars (see, e.g., Torres et al. 2012; Santos et al. 2013; Sousa et al. 2015; Maldonado et al. 2018, 2019). Moreover, several studies have pointed out the existence of correlations between the characteristics of the host stars and the properties and frequencies of their planetary systems, in particular for giant transiting planets, which are the focus of the present work. As a result, the evidence supporting the correlation between the stellar metallicity and occurrence rate of giant planets (e.g., Santos et al. 2004; Valenti & Fischer 2005) and the weakening of this correlation toward lower regimes of planetary mass (e.g., Sousa et al. 2008; Ghezzi et al. 2010) or for wide-orbit planets (Swastik et al. 2021), the connection between planet radius and stellar metallicity (Buchhave et al. 2014), the correlation between stellar metallicity and planetary heavy-metal content (e.g., Guillot et al. 2006), the trend between orbit eccentricity and star metallicity (Dawson & Murray-Clay 2013), the role of the abundances of α-elements (Robinson et al. 2006; Gonzalez 2009; Adibekyan et al. 2012c, 2015) or of the Li depletion observed for massive planet-hosting stars (e.g., Delgado Mena et al. 2015) is becoming more numerous thanks to the constant increase in new planet discoveries.

Again, for the information on the hosting star's chemical composition it is important to separate the signatures left on the planet during its formation and migration from those due to the star. The various physical processes associated with forming giant planets (e.g., planet-disk interaction, planet-planet scattering, in situ formation, multiple generation of embryos) are thought to result in differences in atmospheric composition depending on the enrichment by chemical elements present at the formation site or accreted during migration (Voelkel et al. 2022, and references therein). In particular, some studies suggest that the planetary carbon-to-oxygen ratio and metallicity with respect to the corresponding stellar values could provide constraints on the original formation region of the planet with respect to the H_2O, CO_2, and CO snow lines, and on the time when planet migrated to its present orbit (e.g., Öberg et al. 2011). For instance, an enhanced C/O ratio of the planet compared to its host star was found to be produced when the planet formed far beyond the water snowline, predominantly by gas accretion, and then underwent a subsequent disk-free (high-eccentricity) inward migration (Madhusudhan et al. 2014). Therefore, C/O ratio in planet-host stars can provide key information about the protoplanetary disk regions in which the planet was formed, as abundances of the volatiles in the disk gas and solids are heavily affected by the disk radial temperature profile and, therefore, by the distance from the host star while planets accrete. On the contrary, other elemental ratios, like magnesium-to-silicon (Mg/Si) which governs the distribution of silicates in the protoplanetary disk, do not depend as strongly on the distance to the stars as the C/O ratio does (Thiabaud et al. 2015a). However, recent studies highlighted how the use of multiple elemental ratios involving elements with a high contrast in volatility (e.g., S/N, Si/N, S/O, N/O) can provide more detailed and robust constraints on the formation and migration history of giant planets than is possible with C/O alone (Turrini et al. 2021a,b). The same studies argued how planetary elemental ratios normalized to stellar abundances can provide more unequivocal indications and allow for a more straightforward comparison between different planets orbiting different host stars (Turrini et al. 2021a,b; Kolecki & Wang 2021).

With this in mind, the requirement for homogeneity and precision for the stellar parameters and elemental abundances becomes even more crucial; fundamental parameters of large samples of planet-hosting stars are often found in the literature as the result of analysis performed by different methodologies, resulting in an inhomogeneous census of stars with planets. All these arguments highlight how the homogeneous and precise determination of the fundamental properties and elemental abundances of the hosting stars is pivotal for achieving a comprehensive characterization of exoplanets. We therefore analyzed a sample of transiting planet host stars with the HARPS-N spectrograph at the Telescopio Nazionale *Galileo* (TNG) within the Global Architecture of Planetary Systems (GAPS; Covino et al. 2013) project. Our immediate aims are twofold: to apply an accurate procedure to derive stellar parameters, global properties, abundances of multiple elements, and kinematic properties of transiting planet host stars as homogeneously and precisely as possible using high-quality data, and to study the possible relationships between the astrophysical, kinematic, and chemical parameters of exoplanet host stars and the properties of their transiting planets, thus providing necessary information for future studies of their exoplanets with new facilities. We are aware that our procedure is based on non-automatic tools and therefore it is time consuming, but we think that this type of approach can be used as a benchmark analysis for interpreting the composition, the origin, and evolution of planets with current and future theoretical models and statistical studies. For instance, over the last decades, thanks to the successful photometric space missions (CoRoT, *Kepler*/K2, and TESS), a remarkable synergy has emerged between ground-based spectroscopy and asteroseismic techniques for the accurate determination of the fundamental parameters of exoplanet host stars (e.g., di Mauro et al. 2011; Chaplin et al. 2013). Similarly, the efforts made for a large sample of data applying automatic procedures to derive stellar parameters and iron abundances, like those presented by Sousa et al. (2021), are very useful for the statistical approach.

The outline of this paper is as follows. We first present in Sect. 2 the spectroscopic dataset. In Sect. 3 we describe the measurements of the stellar parameters and elemental abundances for 26 species. We then present our results and discuss the behavior of the elemental abundances of the stars with respect to their kinematic or global properties and with respect to planetary properties in Sect. 4. In Sect. 5 we draw our conclusions.

2. Stellar sample, observations, and data reduction

The stellar sample was selected within two GAPS subprograms aimed at searching for additional companions in known systems and at determining the Rossiter-McLaughlin effect in transiting systems (see, e.g., Bonomo et al. 2017). Within this sample we selected targets with spectral types from F5 to K7 (see Table A.1) and with rotational velocity ($v \sin i$) known from the NASA Exoplanet Archive less than $10 \, km \, s^{-1}$. This was done to avoid strong problems due to line blending or the presence of molecular lines, which must be dealt with via different

procedures than those adopted in this work. In the end, we analyzed a total of 28 targets with $9.3 \lesssim V \lesssim 13.4$ mag, of which 13 from the HATNet Exoplanet Survey (HAT-P; Bakos et al. 2004) in the north, 5 from the Wide Angle Search for Planets (WASP; Kane et al. 2004), 2 in common between HATNet and WASP (i.e., WASP11 or HAT-P-10A and HAT-P-30 or WASP51), 1 from the Kilodegree Extremely Little Telescope survey (KELT; Pepper et al. 2007), 2 from the XO Project (McCullough et al. 2005), 2 from of the Qatar Exoplanet Survey (Alsubai et al. 2013), and 1 from the Trans-Atlantic Exoplanet Survey (TrES; O'Donovan 2007). Twenty-seven stars host massive planets with masses (M_p) from ~0.2 to ~7.3 M_{Jup}, and 1 star (HAT-P-26) hosts a Neptune-mass planet with ~0.06 M_{Jup}. All stars but one (namely, XO-2S, observed as a wide companion of the known planet host; Desidera et al. 2014) host transiting planets. Table A.1 lists the basic information on the final sample taken from the literature, together with some characteristics of the planets. Interestingly, the transits of some of our targets (e.g., HAT-P-12, HAT-P-26, WASP-43) will be observed within Cycle 1 of the Guaranteed Time Observations of the *James Webb* Space Telescope[1] (JWST).

Observations were performed between the end of 2012 and 2016 with the high-resolution HARPS-N at TNG spectrograph ($R \sim 115\,000$, $\lambda \sim 3900$−6900 Å; Cosentino et al. 2012). Solar spectra were also performed through observations of the asteroid Vesta. Spectra reduction was performed using the HARPS-N instrument Data Reduction Software pipeline (see the radial velocity curves of the sample in Bonomo et al. 2017). The standard steps for data reduction and the appropriate cross-correlation masks were applied to each target. The final high signal-to-noise ratios (SNR) merged spectra for each target star and for the Sun were obtained by co-adding, after the proper shift, to the rest frame by the corresponding RV. All individual spectra of the given star and of Vesta reached a SNR (per pixel at $\lambda \sim 6000$ Å) between 100 and 300 for the targets (except for Qatar-2, the faintest one in the sample, with a mean SNR around 50) and $SNR \sim 300$ for the solar spectrum.

Due to the importance of deriving accurate oxygen abundances for as many targets as possible (see, e.g., discussions in Sects. 4.6–4.9), and since very useful oxygen lines like those of the O I triplet at ~777 nm are not present within the HARPS-N spectral range, we decided to search for processed FEROS at ESO spectra ($R \sim 48\,000$, $\lambda \sim 3600$−9000 Å; Kaufer et al. 1999) available in the ESO archive. In the end, we found FEROS spectra for the Sun and seven stars: HAT-P-30, WASP-54, HAT-P-17, HAT-P-26, HAT-P-20, Qatar 2, WASP-43. The typical SNR of these spectra was greater than ~50 at $\lambda \sim 6000$ Å. These spectra also allowed us to derive nitrogen abundances from high-excitation permitted lines (see Sect. 3.2). For homogeneity reasons, we verified that for the targets observed with FEROS and using the same method applied for HARPS-N spectra based on the spectral synthesis of the oxygen $\lambda 6300.3$ Å line and the CN molecule (see Sect. 3.2), we derived O and N abundances very close to those obtained with HARPS-N spectra (within the uncertainties). On the other hand, we verified that for the two targets for which we could measure oxygen and nitrogen both using FEROS and HARPS-N diagnostics we obtained very similar results, within the errors.

We note that for some of the targets within the GAPS project we performed a preliminary analysis of some astrophysical parameters (effective temperature, surface gravity, and iron

abundance), but it was non-homogeneous and based on previous version of tools, model atmospheres, and line lists (see Covino et al. 2013; Desidera et al. 2014; Esposito et al. 2014, 2017; Damasso et al. 2015a,b; Biazzo et al. 2015; Sozzetti et al. 2015; Mancini et al. 2015, 2018, 2022). We note here that the analysis performed in this work is absolutely new, and innovative, homogeneous, and aimed at a characterization of our sample of stars that is as broad as possible.

3. Data analysis

3.1. Stellar parameters and iron abundance

We derived stellar parameters and iron abundances using the code MOOG (Sneden 1973; version 2017) with the driver *abfind*, which assumes local thermodynamic equilibrium (LTE) and treating the radiative and Stark broadenings in a standard way. For collisional broadening, we used the Barklem et al. (2000) prescriptions for damping values. We used plane-parallel model atmospheres linearly interpolated from the ATLAS9 grids of Castelli & Kurucz (2003), with solar-scaled chemical composition and new opacities (ODFNEW).

Effective temperature T_{eff}, surface gravity $\log g$, microturbulence velocity ξ, and iron abundance [Fe/H] were measured through a method based on equivalent widths (EWs) of iron lines. We adopted the list of iron lines by Biazzo et al. (2012) and corrected the atomic parameters of the Fe II line at $\lambda 6516.08$ Å with the most recent NIST values (National Institute of Standards and Technology; Kramida 2019) because they led to the most reliable solar iron abundance measurements. The iron line list was built to minimize potential correlations between the atmospheric parameters, by including lines of different strengths at a given excitation potential and by having a wide distribution of excitation potentials. In addition, we keep in our line list only the iron lines that could be reliably measured at our spectral resolution. In the end, a total of 82 Fe I+11 Fe II lines were considered. The EWs of the target stars were measured by means of a direct integration or Gaussian fitting procedure using the IRAF[2] SPLOT task. We discarded strong lines (EW > 150 mÅ) and those lines with fitting errors larger than 2σ. Each line equivalent width was controlled and measured several times and particular attention was paid to the continuum tracing. The continuum placement of each stellar line was defined looking at the continuum position of the same line in the solar spectrum and the same criteria (both for the continuum definition and the intervals selected for the integration) were adopted. The values of T_{eff} and ξ were determined by imposing the condition that the Fe I abundance does not depend on the excitation potential and equivalent width of the lines, while $\log g$ was obtained from the Fe I/Fe II ionization equilibrium. We used an iterative procedure by changing the parameters at steps of 5 K in T_{eff}, 0.01 km s^{-1} in ξ, and 0.01 dex in $\log g$, and requiring that the slope of the Fe I abundance with respect to the excitation potential (for T_{eff}) or EW (for ξ) was close to zero and that the difference between the mean iron abundance obtained from the Fe I and Fe II lines was lower than 0.01 dex (for $\log g$). We therefore derived stellar parameters with internal accuracy (at 3σ) ranging from 15 to 90 K in T_{eff}, from 0.09 to 0.19 dex in $\log g$, from 0.02 to 0.41 km s^{-1} in ξ, and from 0.07 to 0.15 dex in [Fe/H] (see Table 1). As a sanity

Table 1. Final stellar parameters (effective temperature, surface gravity, microturbulence velocity, rotational velocity), and iron and lithium abundances derived in this work (for Fe I and Fe II the number of lines used to derive the abundances is in parentheses), together with macroturbulence velocity $V_{\rm macro}$ and mean radial velocity $\langle V_{\rm rad}\rangle$.

Name	$T_{\rm eff}$ (K)	$\log g$ (dex)	ξ (km s^{-1})	[Fe I/H] (dex)	[Fe II/H] (dex)	$V_{\rm macro}^{(*)}$ (km s^{-1})	$v \sin i$ (km s^{-1})	$\log n$(Li) (dex)	$\langle V_{\rm rad}\rangle^{(**)}$ (km s^{-1})
HAT-P-3	5175 ± 75	4.52 ± 0.09	0.63 ± 0.04	$0.25 \pm 0.09(70)$	$0.25 \pm 0.12(10)$	2.0	1.4 ± 0.5	<0.5	-23.378 ± 0.018
HAT-P-4	5915 ± 15	4.15 ± 0.12	1.23 ± 0.02	$0.29 \pm 0.08(77)$	$0.29 \pm 0.08(10)$	4.1	5.6 ± 0.5	2.84 ± 0.03	-1.366 ± 0.012
HAT-P-12	4650 ± 70	4.50 ± 0.09	0.49 ± 0.15	$-0.25 \pm 0.09(67)$	$-0.25 \pm 0.12(7)$	1.6	0.5 ± 0.5	...	-40.458 ± 0.002
HAT-P-14	6715 ± 20	4.12 ± 0.15	1.50 ± 0.06	$0.05 \pm 0.08(71)$	$0.05 \pm 0.10(11)$	7.8	8.1 ± 0.3	2.02 ± 0.15	-20.341 ± 0.039
HAT-P-15	5570 ± 90	4.39 ± 0.15	0.59 ± 0.22	$0.26 \pm 0.09(73)$	$0.26 \pm 0.09(10)$	2.8	2.0 ± 0.3	...	31.755 ± 0.003
HAT-P-17	5255 ± 45	4.50 ± 0.15	0.60 ± 0.19	$0.03 \pm 0.08(73)$	$0.03 \pm 0.09(11)$	2.1	1.3 ± 0.3	...	20.200 ± 0.007
HAT-P-18	4825 ± 75	4.43 ± 0.13	0.67 ± 0.30	$0.09 \pm 0.09(69)$	$0.09 \pm 0.09(10)$	1.7	1.3 ± 0.4	...	-11.105 ± 0.009
HAT-P-20	4595 ± 60	4.49 ± 0.09	0.40 ± 0.40	$0.17 \pm 0.10(64)$	$0.17 \pm 0.14(8)$	1.5	2.6 ± 0.3	...	-18.192 ± 0.215
HAT-P-21	5640 ± 25	4.24 ± 0.11	0.98 ± 0.04	$0.04 \pm 0.08(77)$	$0.04 \pm 0.08(11)$	3.0	3.9 ± 0.5	...	-52.978 ± 0.079
HAT-P-22	5290 ± 50	4.35 ± 0.15	0.58 ± 0.26	$0.26 \pm 0.08(70)$	$0.26 \pm 0.09(11)$	2.2	1.8 ± 0.5	...	12.669 ± 0.037
HAT-P-26	5070 ± 80	4.49 ± 0.09	0.43 ± 0.32	$0.02 \pm 0.09(74)$	$0.02 \pm 0.11(11)$	2.0	0.8 ± 0.4	...	13.844 ± 0.001
HAT-P-29	6110 ± 70	4.35 ± 0.13	1.08 ± 0.03	$0.24 \pm 0.08(76)$	$0.24 \pm 0.09(11)$	4.5	4.5 ± 0.7	...	-21.629 ± 0.009
HAT-P-30	6290 ± 60	4.30 ± 0.14	1.05 ± 0.04	$0.10 \pm 0.08(75)$	$0.10 \pm 0.07(10)$	5.2	3.0 ± 0.5	3.04 ± 0.05	44.727 ± 0.018
HAT-P-36	5550 ± 80	4.33 ± 0.16	0.67 ± 0.22	$0.27 \pm 0.09(74)$	$0.27 \pm 0.09(10)$	2.7	3.6 ± 0.3	...	-16.243 ± 0.019
KELT-6	6250 ± 20	3.93 ± 0.13	1.38 ± 0.05	$-0.28 \pm 0.07(76)$	$-0.28 \pm 0.06(11)$	5.8	4.5 ± 0.5	1.19 ± 0.06	1.165 ± 0.007
Qatar-1	4820 ± 85	4.45 ± 0.12	0.69 ± 0.35	$0.16 \pm 0.09(68)$	$0.16 \pm 0.09(10)$	1.7	1.9 ± 0.7	...	-38.034 ± 0.056
Qatar-2	4645 ± 60	4.52 ± 0.10	0.45 ± 0.40	$0.12 \pm 0.10(59)$	$0.12 \pm 0.11(7)$	1.6	2.1 ± 0.4	...	-23.971 ± 0.037
TRES-4	6270 ± 45	4.09 ± 0.17	1.56 ± 0.03	$0.26 \pm 0.09(75)$	$0.26 \pm 0.10(11)$	5.5	9.5 ± 0.8	...	-16.100 ± 0.009
WASP-10	4665 ± 60	4.40 ± 0.13	0.53 ± 0.38	$0.13 \pm 0.09(66)$	$0.13 \pm 0.09(8)$	1.6	3.3 ± 0.5	...	-4.228 ± 0.019
WASP-11	4865 ± 25	4.43 ± 0.12	0.67 ± 0.11	$0.07 \pm 0.09(72)$	$0.07 \pm 0.11(10)$	1.7	1.2 ± 0.3	...	4.911 ± 0.012
WASP-13	5980 ± 50	4.09 ± 0.12	1.11 ± 0.04	$0.10 \pm 0.08(78)$	$0.10 \pm 0.08(10)$	4.5	4.0 ± 0.7	2.05 ± 0.07	9.855 ± 0.010
WASP-38	6295 ± 20	4.27 ± 0.18	1.31 ± 0.05	$0.09 \pm 0.09(79)$	$0.09 \pm 0.10(11)$	5.3	8.3 ± 0.8	1.97 ± 0.04	-9.7317 ± 0.047
WASP-39	5420 ± 20	4.30 ± 0.11	0.73 ± 0.03	$0.00 \pm 0.07(73)$	$0.00 \pm 0.09(11)$	2.4	1.8 ± 0.4	...	-58.443 ± 0.003
WASP-43	4465 ± 90	4.45 ± 0.19	0.68 ± 0.41	$-0.04 \pm 0.15(49)$	$-0.04 \pm 0.14(4)$	1.5	2.6 ± 0.4	...	-3.661 ± 0.041
WASP-54	6155 ± 25	4.02 ± 0.11	1.20 ± 0.03	$-0.09 \pm 0.08(78)$	$-0.09 \pm 0.09(10)$	5.2	3.6 ± 0.9	...	-3.107 ± 0.014
WASP-60	6040 ± 30	4.21 ± 0.11	1.14 ± 0.02	$0.23 \pm 0.07(77)$	$0.23 \pm 0.09(11)$	4.4	3.3 ± 0.6	...	-26.526 ± 0.002
XO-2N	5290 ± 70	4.46 ± 0.10	0.59 ± 0.15	$0.37 \pm 0.10(74)$	$0.37 \pm 0.10(10)$	5.2	1.8 ± 0.4	...	46.920 ± 0.009
XO-2S	5300 ± 80	4.41 ± 0.13	0.60 ± 0.20	$0.32 \pm 0.10(72)$	$0.32 \pm 0.11(10)$	5.2	1.7 ± 0.4	...	46.574 ± 0.005

Notes. $^{(*)}$The macroturbulence velocity $V_{\rm macro}$ was computed from empirical relationships taken from the literature and useful to derive parameters and abundances through the spectral synthesis method (see Sect. 3.2). $^{(**)}$We computed the mean radial velocity $\langle V_{\rm rad}\rangle$ to derive kinematic properties (see Sect. 4.3). As final errors on radial velocities we considered both those in the mean values of the HARPS-N measurements listed here and a typical zero-point level of $0.2\,{\rm km\,s}^{-1}$.

check, the final iron abundance of each target was plotted as a function of stellar $T_{\rm eff}$, $\log g$, and ξ, and $v \sin i$ (for the measurement of the rotational velocity see Sect. 3.2) to look for the possible presence of spurious trends due to line blending, for example.

Our analysis was performed differentially with respect to the solar spectrum, which was used as a reference to minimize errors due to uncertainties in measurements of EWs, continuum definition, atomic parameters, and model atmospheres. We therefore analyzed the co-added spectrum of Vesta, using our line list, imposing the solar effective temperature $T_{\rm eff\odot} = 5770$ K and surface gravity $\log g_\odot = 4.44$ dex, and leaving the microturbulence free to vary. The final optimization was obtained for $\xi_\odot = 0.99\,{\rm km\,s}^{-1}$, leading to $\log n({\rm Fe\,I})_\odot = 7.49 \pm 0.05$ and $\log n({\rm Fe\,II})_\odot = 7.49 \pm 0.05$.

3.2. Abundance of other elements and rotational velocity

For elements other than iron, we applied spectroscopic techniques based on line EWs and spectral synthesis depending of the element. We also measured the rotational velocity through spectral synthesis.

3.2.1. Analysis based on equivalent widths

Once the stellar parameters and iron abundances were measured, we computed the abundances of the other elements ([X/H][3]) using the MOOG code (Sneden 1973; version 2017) and the drivers *abfind* and *blends* for the treatment of the lines without and with hyperfine structure (HFS). In particular, in addition to Fe we computed the abundance of 25 elements: Li, C, N, O, Na, Mg, Al, Si, S, Ca, Sc, Ti, V, Cr, Mn, Co, Ni, Cu, Zn, Y, Zr, Ba, La, Nd, and Eu. As was done for Fe, we measured the abundances of two ionization states also for Ti and Cr, while for the other elements only the abundance of one species (first or second ionization state) was measured (see Table A.2).

As was done for the iron lines, the EW of each spectral line was measured on the one-dimensional spectra interactively using the *splot* task in IRAF. The location of the local continuum was carefully selected tracing as closely as possible the same position for the spectral line of each star and the asteroid Vesta. This was done with the aim of minimizing the error on the selection

---

[3] Throughout the paper the abundance of the X element is given as [X/H] = $\log \frac{\epsilon(X)}{\epsilon(H)} + 12$, where $\log \epsilon(X)$ is the absolute abundance.

of the continuum. We also excluded features affected by telluric absorption.

Following the prescriptions by Biazzo et al. (2015), we started from the line list of Na I, Mg I, Al I, Si I, Ca I, Ti I, Ti II, Cr I, Cr II, Ni I, and Zn I by Biazzo et al. (2012) complemented with additional lines and atomic parameters for Na I, Al I, Si I, Ti I, Ti II, Cr I, Ni I, and Zn I taken from Schuler et al. (2011) and Sozzetti et al. (2006). For the Mg I line at λ4730 Å and the Al I line at λ6698.67 Å we considered the NIST (Kramida 2019) and the Meléndez et al. (2014) atomic parameters. In the cases of C I, S I, Sc II, V I, Mn I, Co I, and Cu I, we considered the line lists by Kurucz (1993), Schuler et al. (2011), Kramida (2019), Johnson et al. (2006), and Scott et al. (2015), where the hyperfine structure by Johnson et al. (2006) and Kurucz (1993) was adopted for Sc, V, Mn, Cu, and Co. Solar isotopic ratios by Anders & Grevesse (1989) were considered for Cu (i.e., 69.17% for ^{63}Cu and 30.83% for ^{65}Cu). For the s-process elements Y II and Zr II (first peak), Ba II and La II (second peak), the mixed s/r-process element Nd II, and the r-process element Eu II we considered the line lists by Johnson et al. (2006), Ljung et al. (2006), Prochaska et al. (2000), Lawler et al. (2001b), and Den Hartog et al. (2003), where the HFS by Gallagher et al. (2010) and Lawler et al. (2001a) was adopted for Ba and La, respectively. Solar isotopic ratios by Anders & Grevesse (1989) were considered for Ba (i.e., 2.417% for ^{134}Ba, 7.854% for ^{136}Ba, 71.70% for ^{138}Ba, 6.592% for ^{135}Ba, and 11.23% for ^{137}Ba) and Eu (i.e., 47.8% for ^{151}Eu and 52.2% for ^{153}Eu).

For the targets observed also with FEROS, we measured oxygen and nitrogen abundances through line EWs. The oxygen abundance was estimated using the O I triplet of permitted lines at λ7771.94, λ7774.17, λ7775.39 Å with atomic parameters by NIST (Kramida 2019), and considering the non-LTE (NLTE) corrections by Amarsi et al. (2015). To our knowledge, no NLTE correction are present for [Fe/H] > 0 and for $T_{\rm eff}$ < 5000 K, and the effect is important for $T_{\rm eff}$ differences also of 50 K (while it is negligible for [Fe/H] differences within 0.4 dex). This is why we considered the O I abundances measured for the Sun and the stars WASP-54, HAT-P-17, HAT-P-26, and the slightly metal-rich star HAT-P-30, while we excluded from the analysis the other (cooler) targets observed with FEROS (i.e., HAT-P-20, Qatar-2, and WASP-43). The importance of these effects has been also demonstrated for hot exoplanetary atmospheres (Borsa et al. 2021).

Thanks to the FEROS spectra, we also measured nitrogen abundance using three high-excitation permitted lines (e.g., λ7442.3, λ7468.3, λ8216.3 Å), considering the atomic parameters by Caffau et al. (2009). Stars with $T_{\rm eff} \lesssim 5200$ K are too cool to have detectable N I lines, while within the warmer targets observed with FEROS only the spectra of Vesta and HAT-P-30 had sufficient SNR to measure the nitrogen abundance. No correction for NLTE effects was applied for the N abundance of our sample because to our knowledge it is only available for the Sun (see Caffau et al. 2009).

In addition to O I, due to the relatively wide range in the stellar parameters of our targets (mainly $T_{\rm eff}$ and [Fe/H]), we also applied NLTE corrections to each line abundance of C I, Na I, Mn I, and Co I, following the prescriptions given by Amarsi et al. (2019), Lind et al. (2011), Bergemann & Gehren (2008), and Bergemann et al. (2010), respectively. For the other elements, no NLTE departure was considered because corrections were negligible or not reported in the literature for the lines used in this work and for the $T_{\rm eff}$ and [Fe/H] ranges of our targets. As for the iron lines, the final elemental abundance of each target was

plotted as a function of stellar $T_{\rm eff}$, $\log g$, ξ, and $v \sin i$ to look for possible trends, for example due to line blendings. When trends were found for a specific element (in particular at lower and higher $T_{\rm eff}$), each line of that element was plotted as a function of $T_{\rm eff}$, $\log g$, ξ, and $v \sin i$ to recognize the presence of effects due mainly to line blending or the bad quality of the spectrum for that specific line, which was then removed. In the end, no trend was found for the final abundances and stellar parameters, with the exception of Cr II and C I for which a residual trend with effective temperature remained. These two elements are discussed in the next paragraph.

3.2.2. Analysis based on spectral synthesis

The projected rotational velocity ($v \sin i$) and the lithium abundance ($\log n$(Li)) were measured by applying the spectral synthesis technique. We used the *synth* driver within the MOOG code (Sneden 1973; version 2017) and considered synthetic spectra obtained from the Castelli & Kurucz (2003) grids of model atmospheres at the stellar parameters ($T_{\rm eff}$, $\log g$, ξ, [Fe/H]) derived in Sect. 3.1. We applied the same method to derive the abundances of carbon, nitrogen, and oxygen, which are also elements analyzed through line EWs. In particular, we convolved the synthetic spectra with a Gaussian profile corresponding to the resolution of HARPS-N of $R \sim 115\,000$, taking into account the optical limb-darkening coefficients by Claret (2019) at the stellar $T_{\rm eff}$, $\log g$, ξ, and [Fe/H]. Moreover, the empirical relationships obtained using the asteroseismic rotational velocities by Doyle et al. (2014) from the *Kepler* data were used to derive the macroturbulence velocity ($V_{\rm macro}$) for $T_{\rm eff}$ > 5700 K, while empirical relationships by Brewer et al. (2016) were considered for $T_{\rm eff}$ < 5700 K[4].

For the $v \sin i$ we synthesized spectral lines in two regions around 6200 and 6700 Å, as done in Barbato et al. (2019), until the minimum of residuals between stellar and synthetic spectra were reached. The final values are listed in Table 1, where the errors take into account uncertainties in stellar parameters ($T_{\rm eff}$, $\log g$, ξ, [Fe/H]) and spectral continuum definition (for the uncertainties in the continuum position, see next paragraph).

The forbidden [O I] line at 6300.3 Å was considered for deriving the O abundance through spectral synthesis and using the above-mentioned code and model atmospheres. Atomic parameters for the O line and the nearby (blended) Ni I line were taken from Caffau et al. (2008) and Johansson et al. (2003), respectively (see also Bertran de Lis et al. 2015, and references therein). Nickel abundances were fixed to the values we derived above. No NLTE correction were made because the λ6300.3 Å line is not affected by deviation from LTE (Caffau et al. 2008).

Then, adopting the estimated O abundance, C was measured from ^{12}CH and ^{13}CH molecular features around 4320 Å (see the example in Fig. 1). Molecular parameters were taken from Masseron et al. (2014). Atomic lines were re-adjusted on the solar spectrum. The C abundances from these CH bands were measured for all targets but two cool stars (Qatar-2 and WASP-43), mainly because of the very critical continuum placement.

Finally, the N abundance was obtained from the CN features at ~4215 Å, adopting the measured C and O abundances derived through spectral synthesis. The fitting procedure was differential

---

[4] This was done because these relationships are not valid for the whole parameter space of our targets, but we verified that in the $T_{\rm eff}$ range in common, the two calibrations are in very good agreement (mean difference in $V_{\rm macro}$ of ~0.5 km s^{-1}).
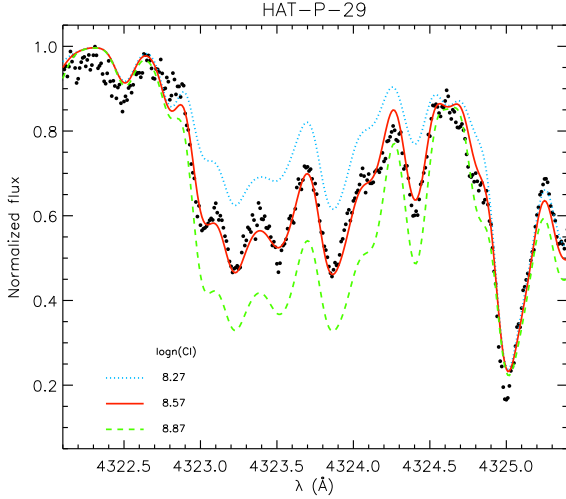
Fig. 1. Comparison between observed (black dots) and synthetic spectra for the target HAT-P-29 in the region around the CH band at ~4320 Å. The shown synthetic spectra were computed for $\log n(C) = 8.57$ (red solid line; best fit), 8.87 (green dashed line), 8.27 dex (blue dotted line).
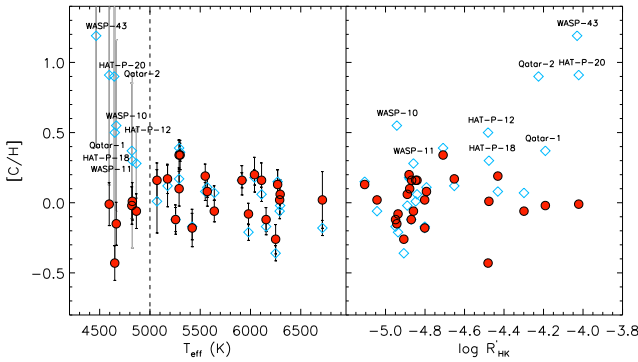

Fig. 2. Carbon abundances as a function of T_{eff} (*left panel*) and the activity index $\log R'_{HK}$ (*right panel*), as derived from C I lines (open diamonds) and the CH band (filled circles). The dashed line in the left panel gives the position at $T_{eff} = 5000$ K. Stars with $T_{eff} < 5000$ K are highlighted in both panels.

(i.e., adopting the same spectral range and features in each star), and it was repeated until the minimum of residuals was obtained. The line lists for the $^{12}C^{14}N$, $^{13}C^{14}N$, and $^{12}C^{15}N$ isotopologues were taken from Sneden et al. (2014). Given the sensitivity to T_{eff}, the N abundance from the CN band was measured for stars in the $4600-5300$ K T_{eff} range.

Since CNO abundances were derived with both EWs and spectral synthesis, as final abundance we considered the weighted average coming from these two methods. In particular, Fig. 2 shows the C abundances derived from C I lines (open diamonds) and those derived from the CH band (filled circles). We find a good agreement between the [C/H] measured from these two diagnostics for $T_{eff} > 5000$ K, with the largest differences for cooler stars, for which the atomic carbon lines provide abundances larger than twice the typical error on [C/H]. Similar results were found by Baratella et al. (2020) and Delgado Mena et al. (2021), among others. The latter authors mentioned a possible dependence of the trend with the metallicity (slight increase in [C/Fe] toward lower metallicity for [C/H] derived through atomic lines, and a flatter trend for abundances obtained from molecular lines). We do not find similar trends, most probably

due to our small stellar sample. We find instead an evident trend with the Mittag chromospheric activity index $\log R'_{HK}$ derived by Claudi et al. (in prep). Similar results were obtained by Baratella et al. (2020), who also found a positive correlation between atomic [C/H] and $\log R'_{HK}$, justified as possible unknown blends in the optical lines becoming more important in active stars than in quiet stars. On the contrary, we do not find any trend between $\log R'_{HK}$ and other abundances or ξ, thus further validating our method of deriving elemental abundances (see also discussion in Baratella et al. 2020). In the end, we decided to consider a weighted average between C abundances derived with the atomic and the CH band for $T_{eff} > 5000$ K, while for $T_{eff} < 5000$ K we considered only the values from the CH band as C abundances[5].

The lithium abundance ($\log n(Li)$) was derived through spectral synthesis of the absorption line at $\lambda 6707.8$ Å, which was present in seven stars (KELT-6, HAT-P-14, WASP-38, HAT-P-30, WASP-13, HAT-P-4, HAT-P-3; see Sect. 4.5). In particular, we used the lithium line list by Reddy et al. (2002) in the vicinity (± 0.5 Å) of the Li 6707.8 Å line, implemented with the VALD database (Kupka et al. 2000) for wavelengths farther from the line center. The line list by Reddy et al. (2002) considers the isotopes ^6Li and ^7Li of the $\lambda 6707.8$ Å line allowing us to estimate the lithium isotopic $^6Li/^7Li$ ratio. The lithium abundance derived through the MOOG code was then corrected for the departure from LTE considering the non-LTE calculation of Lind et al. (2009). A double-check of the final results was done computing the lithium abundances also using the Li equivalent widths and converting them in abundances through the curves of growth by Lind et al. (2009). We found consistent values with both methods within the uncertainties. In Table 1 we list only the results obtained through spectral synthesis. The errors on $\log n(Li)$ were derived by adding quadratically the uncertainties due to the abundance measurements and those due to stellar parameters.

The results for all solar elemental abundances are given in Table 2 together with those given by Asplund et al. (2021) and obtained using a 3D radiative-hydrodynamic model of the solar surface convection and atmosphere, and correction for departures from LTE conditions when necessary. This table shows good agreement between our solar abundance values and the literature results, with a mean difference between values derived in this work and in the literature of 0.00 ± 0.04 dex.

3.2.3. Uncertainties in elemental abundances

Derived abundances are mainly affected by uncertainties in atomic parameters, stellar parameters, and measured EWs (or continuum position when spectral synthesis was applied).

Uncertainties in atomic parameters, such as the transition probability ($\log gf$), should cancel out since our analysis is carried out differentially with respect to the Sun. Errors due to uncertainties in stellar parameters (T_{eff}, ξ, $\log g$, [Fe/H]) were estimated first by assessing errors on stellar parameters themselves and then by varying each parameter separately, while keeping the other two unchanged. As shown in Table 1 and explained in Sect. 3.1, the uncertainties in stellar parameters are

---

[5] We also find some discrepancy in Cr abundances, for which we obtained mean differences of 0.15 dex between Cr I and Cr II for stars cooler than 5000 K. Similar findings were observed in Baratella et al. (2020), for which blendings at low T_{eff} and chromospheric activity effects were invoked as possible reasons of the observed overionization. No similar trends were observed between Ti I and Ti II. Whatever the reason, we decided to use only Cr I and Ti I as abundances of chromium and titanium, respectively.

Table 2. Comparison between our measured solar abundances and the standard values from Asplund et al. (2021).

Species	Z	T_{cond}	$\log n_{This\ work}$	$\log n_{Literature}$
Li I	2	1142	1.04 ± 0.09	0.96 ± 0.06
C I(EW)	6	40	8.43 ± 0.05	
C I(synt)			8.41 ± 0.03	8.46 ± 0.04
N I(EW)	7	123	7.95 ± 0.03	
N I(synt)			...	7.83 ± 0.07
O I(EW)	8	180	8.66 ± 0.03	
O I(synt)			8.69 ± 0.10	8.69 ± 0.04
Na I	11	958	6.21 ± 0.01	6.22 ± 0.03
Mg I	12	1336	7.59 ± 0.06	7.55 ± 0.03
Al I	13	1653	6.42 ± 0.06	6.43 ± 0.03
Si I	14	1310	7.52 ± 0.05	7.51 ± 0.03
S I	16	664	7.13 ± 0.03	7.12 ± 0.03
Ca I	20	1517	6.30 ± 0.06	6.30 ± 0.03
Sc II	21	1659	3.10 ± 0.06	3.14 ± 0.04
Ti I	22	1582	4.95 ± 0.04	4.97 ± 0.05
Ti II			4.95 ± 0.05	
V I	23	1429	3.86 ± 0.04	3.90 ± 0.08
Cr I	24	1296	5.62 ± 0.04	5.62 ± 0.04
Cr II			5.62 ± 0.05	
Mn I	25	1158	5.42 ± 0.04	5.42 ± 0.06
Fe I	26	1334	7.49 ± 0.05	7.46 ± 0.04
Fe II			7.49 ± 0.05	
Co I	27	1352	4.96 ± 0.06	4.94 ± 0.05
Ni I	28	1353	6.24 ± 0.05	6.20 ± 0.04
Cu I	29	1037	4.22 ± 0.09	4.18 ± 0.05
Zn I	30	726	4.56 ± 0.05	4.56 ± 0.05
Y II	39	1659	2.18 ± 0.06	2.21 ± 0.05
Zr II	40	1741	2.57 ± 0.02	2.59 ± 0.04
Ba II	56	1455	2.19 ± 0.05	2.27 ± 0.05
La II	57	1578	1.06 ± 0.01	1.11 ± 0.04
Nd II	60	1602	1.41 ± 0.01	1.42 ± 0.04
Eu II	63	1356	0.50 ± 0.03	0.52 ± 0.04

Notes. Z represents the atomic number and T_{cond} the 50% condensation temperature values derived by Lodders (2003).
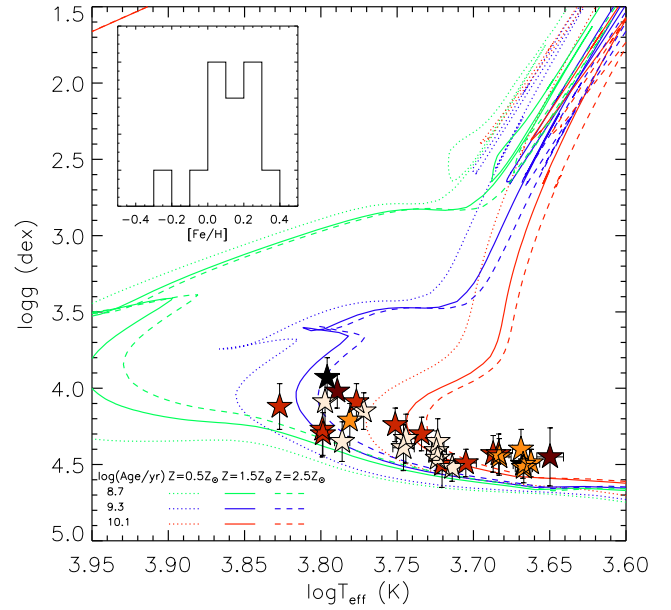

Fig. 3. T_{eff}-$\log g$ diagram for our stellar sample. The green, blue, and red lines are the PARSEC isochrones at ~500 Myr, ~2 Gyr, and ~12.5 Gyr. Dotted, solid, and dashed lines represent three different values of metallicities, as labeled in the bottom left corner. The inset represents the histogram distribution in [Fe/H] of our targets. The star symbols are colored from dark to light and represent the most metal-rich to most metal-poor stars according to four bins: [Fe/H] ≥ +0.24 dex, −0.12 < [Fe/H] ≤ +0.24 dex, −0.15 < [Fe/H] ≤ −0.02 dex, and [Fe/H] ≤ −0.15 dex.

Sun. When only one line was measured, the error on [X/H] is the standard deviation of three independent EW measurements obtained taking different positions of the continuum. The number of lines employed for the abundance analysis is listed in Tables 1 and A.2 in brackets.

For the uncertainties due to the definition of continuum position when spectral synthesis was applied, random errors affecting our best-fit procedure were evaluated by changing the continuum position until the standard deviation (observed minus synthetic spectra) was two times larger than the best-fit value, where residuals of our best-fit solutions are typically smaller than 0.02. These error budgets are listed in Table A.2.

3.3. Final parameters and comparison with previous works

Figure 3 shows the position of our targets in the Kiel T_{eff}-$\log g$ diagram along with stellar model tracks for three different metallicities (i.e., $Z = 0.5\ Z_\odot$, $1.5\ Z_\odot$, $2.5\ Z_\odot$) and ages (i.e., $\log(Age/yr) = 8.7, 9.3, 10.1$) spanning the values of our stellar sample (see Sect. 3.1 for our iron abundance measurement and Sect. 4.4 for our age estimation using chemical clocks). The stars are color-coded with respect to [Fe/H], from approximately −0.3 dex up to +0.4 dex, as shown in the histogram. Our homogeneous procedure led to stellar parameters agreeing with theoretical tracks within the uncertainties. Some evidence that our $\log g$ is slightly greater than that derived from the tracks at a mean level of ~0.1 dex seems to be present for stars cooler than ~4900 K, but this is compatible with the internal error on $\log g$ and is probably due to the smaller number of Fe II lines for lower T_{eff}. Similar findings were obtained by Brucalassi et al. (2021) and Magrini et al. (2022) for targets of the ARIEL mission.

in the range 15–90 K for T_{eff} (with a standard deviation σ of 25 K), 0.09–0.19 dex for $\log g$ ($\sigma = 0.03$ dex), 0.02–0.41 km s^{-1} for ξ ($\sigma = 0.14$ km s^{-1}), and 0.07–0.15 dex for [Fe/H] ($\sigma = 0.02$ dex). Due to the small values of the standard deviations across the wide range of stellar effective temperature for the errors on T_{eff}, $\log g$, and [Fe/H], and due to the smaller influence of errors on ξ for almost all elements, when compared to the other sources of uncertainties, we decided to consider typical uncertainties in stellar parameters of 60 K, 0.10 dex, 0.15 km s^{-1}, and ~0.08 dex in T_{eff}, $\log g$, ξ, and [Fe/H], respectively. We thus assumed these values as uncertainties in stellar parameters. Errors on abundances [X/H] due to uncertainties in stellar parameters are summarized in Table 3 for two different stars in our sample from which we derived all elemental abundances: one of the coolest stars (HAT-P-12 or WASP-10) and one of the warmest stars (HAT-P-30). Total errors on $\log n$(Li) are instead reported in Table 1.

The errors due to uncertainties in EWs are well represented by the standard deviation around the mean abundance determined from all the lines. These errors are listed in Tables 1 and A.2, where the uncertainties in [X/H] were obtained by quadratically adding the error for the target and the error for the

Table 3. Internal errors on abundance determination due to uncertainties in stellar parameters for one of the coolest stars (HAT-P-12 for all elements but C and N; WASP-10 for C and N) and for one of the warmest stars (HAT-P-30) in our sample.

HAT-P-12	$T_{\rm eff}$ = 4650 K	$\log g$ = 4.50 dex	ξ = 0.49 km s^{-1}	[Fe/H] = -0.25 dex
	$\Delta T_{\rm eff}$ = $-/+60$ K	$\Delta \log g$ = $-/+0.10$ dex	$\Delta\xi$ = $-/+0.15$ km s^{-1}	Δ[Fe/H] = $-/+0.08$ dex
[Fe I/H]	0.00/0.00	0.01/-0.01	0.01/-0.02	.../...
[Fe II/H]	0.08/-0.07	-0.03/0.09	0.01/-0.01	.../...
[C I/H]	0.09/-0.09	0.01/-0.01	0.01/-0.01	-0.01/0.01
[N I/H]	0.05/-0.05	0.00/0.00	0.00/0.00	0.00/0.00
[O I/H]	0.08/-0.08	0.05/-0.05	0.00/0.00	0.00/0.00
[Na I/H]	-0.03/0.05	0.03/0.00	0.01/-0.01	-0.01/0.01
[Mg I/H]	0.01/0.00	0.01/0.00	0.00/0.00	-0.02/0.02
[Al I/H]	-0.02/0.04	0.02/0.00	0.01/-0.01	-0.01/0.01
[Si I/H]	0.04/-0.04	-0.01/0.00	0.00/0.00	-0.02/0.02
[S I/H]	0.04/-0.06	-0.02/0.00	0.00/0.00	0.00/0.00
[Ca I/H]	-0.03/0.07	0.04/0.00	0.01/-0.01	-0.02/0.02
[Sc II/H]	0.01/-0.06	-0.03/0.03	0.00/0.00	-0.03/0.03
[Ti I/H]	-0.06/0.08	0.03/0.00	0.02/-0.03	-0.02/0.02
[Ti II/H]	-0.01/0.01	-0.02/0.00	0.02/-0.03	-0.04/0.03
[V I/H]	-0.08/0.09	0.01/-0.01	0.02/-0.03	-0.01/0.01
[Cr I/H]	-0.04/0.05	0.01/0.00	0.02/-0.02	-0.01/0.02
[Cr II/H]	0.03/-0.05	-0.03/0.00	0.01/-0.01	-0.03/0.02
[Mn I/H]	-0.03/0.03	0.02/-0.02	0.02/-0.02	-0.04/0.03
[Co I/H]	-0.01/0.01	-0.02/0.03	0.00/-0.01	-0.03/0.03
[Ni I/H]	0.00/-0.01	-0.01/0.00	0.00/-0.02	-0.03/0.02
[Cu I/H]	0.00/0.00	-0.01/0.03	0.01/-0.01	-0.03/0.03
[Zn I/H]	0.03/-0.04	0.00/0.00	0.01/-0.02	-0.03/0.03
[Y I/H]	-0.03/0.00	-0.02/0.00	0.03/-0.03	-0.03/0.03
[Zr II/H]	-0.04/0.00	-0.04/0.00	0.02/-0.02	-0.03/0.03
[Ba II/H]	-0.02/0.02	0.00/0.00	0.03/-0.04	-0.05/0.05
[La II/H]	-0.02/0.02	-0.04/0.05	0.00/0.00	-0.03/0.03
[Nd II/H]	-0.05/0.02	-0.03/0.00	0.01/-0.01	-0.03/0.03
[Eu II/H]	0.00/0.00	-0.03/0.05	0.00/0.00	-0.03/0.03
HAT-P-30	$T_{\rm eff}$ = 6290 K	$\log g$ = 4.30 dex	ξ = 1.05 km s^{-1}	[Fe/H] = 0.10 dex
	$\Delta T_{\rm eff}$ = $-/+60$ K	$\Delta \log g$ = $-/+0.10$ dex	$\Delta\xi$ = $-/+0.15$ km s^{-1}	Δ[Fe/H] = $-/+0.08$ dex
[Fe I/H]	-0.04/0.04	0.01/-0.01	0.02/-0.03	.../...
[Fe II/H]	0.00/0.00	-0.04/0.03	0.05/-0.02	.../...
[C I/H]	0.04/-0.04	-0.03/0.03	0.02/-0.02	0.00/0.00
[N I/H]	0.04/-0.04	-0.03/0.03	0.00/0.00	-0.01/0.01
[O I/H]	0.04/-0.04	.01/-0.01	0.02/-0.02	0.00/0.00
[Na I/H]	-0.03/0.03	0.01/-0.01	0.01/-0.01	0.00/0.00
[Mg I/H]	-0.03/0.02	0.00/0.00	0.01/-0.01	0.00/0.00
[Al I/H]	-0.02/0.02	0.00/0.00	0.00/0.00	0.00/0.00
[Si I/H]	-0.02/0.02	0.00/0.00	0.01/-0.01	0.00/0.00
[S I/H]	0.01/-0.01	-0.03/0.03	0.00/0.00	0.00/0.00
[Ca I/H]	-0.04/0.04	0.02/-0.02	0.03/-0.03	0.00/0.00
[Sc II/H]	0.00/0.01	-0.04/0.04	0.01/-0.01	-0.02/-0.05
[Ti I/H]	-0.05/0.05	0.00/0.00	0.02/-0.02	0.00/0.00
[Ti II/H]	0.00/0.01	-0.04/0.04	0.04/-0.04	-0.01/0.01
[V I/H]	-0.05/0.05	0.00/0.00	0.00/0.00	0.00/0.00
[Cr I/H]	-0.04/0.04	0.00/0.00	0.02/-0.02	0.00/0.00
[Cr II/H]	0.01/-0.01	-0.04/0.03	0.03/-0.03	-0.01/0.01
[Mn I/H]	-0.05/0.05	0.00/0.00	0.02/-0.02	0.00/0.00
[Co I/H]	-0.05/0.05	0.00/0.00	0.00/0.00	0.00/0.00
[Ni I/H]	-0.04/0.04	0.00/0.00	0.01/-0.02	0.00/0.00
[Cu I/H]	-0.05/0.05	0.00/0.00	0.01/-0.01	0.00/0.00
[Zn I/H]	-0.02/0.02	0.00/0.01	0.06/-0.06	0.00/0.00
[Y I/H]	-0.01/0.01	-0.04/0.04	0.07/-0.06	-0.02/0.02
[Zr II/H]	-0.01/0.01	-0.04/0.04	0.04/-0.03	-0.02/0.02
[Ba II/H]	-0.03/0.03	-0.02/0.02	0.08/-0.08	-0.02/0.02
[La II/H]	-0.02/0.02	-0.04/0.04	0.00/0.00	-0.02/0.02
[Nd II/H]	-0.02/0.02	-0.04/0.04	0.01/-0.01	-0.02/0.02
[Eu II/H]	-0.01/0.01	-0.04/0.04	0.00/0.00	-0.02/0.02

Notes. The numbers refer to the differences between the abundances obtained with ($-$ and $+$) and without the uncertainties in stellar parameters.

Table 4. Mean difference and standard deviation between the values of the atmospheric parameters derived in the literature and those obtained in this work (n is the number of stars in common).

$\Delta T_{\rm eff}$ (K)	$\Delta \log g$ (dex)	Δ[Fe/H] (dex)	$\Delta \xi$ (km s^{-1})	$\Delta v \sin i$ (km s^{-1})	n	Reference
-25 ± 82	0.06 ± 0.07	-0.04 ± 0.11	0.03 ± 0.33 [*]	-0.1 ± 0.7	28	Discovery papers [◇]
20 ± 60	0.06 ± 0.06	0.00 ± 0.08	...	-0.1 ± 0.5	15	Torres et al. (2012)
35 ± 90	0.04 ± 0.21	0.00 ± 0.07	0.21 ± 0.20	...	28	Santos et al. (2013)
-57 ± 85	-0.07 ± 0.09	0.04 ± 0.08	...	-0.3 ± 0.6	5	Brewer et al. (2016)
51 ± 85	-0.04 ± 0.23	0.01 ± 0.04	0.23 ± 0.22	...	28	Sousa et al. (2021)

Notes. [*]ξ in the discovery papers was often fixed. [◇]For the discovery papers, see the NASA Exoplanet Archive.

The comparison of our stellar parameters with those derived in the literature when at least five targets were in common are plotted in Fig. B.1 and shown in Table 4. In particular, we consider the comparisons with the values of the exoplanet discovery papers derived through different methods, the stellar parameters obtained by Torres et al. (2012) averaging three methods based on spectral synthesis, line equivalent widths, and cross-correlation against a library of spectra, the values by Brewer et al. (2016) derived using spectral synthesis, and those listed in the SWEET-Cat (Stars With ExoplanETs Catalogue; Santos et al. 2013; Sousa et al. 2021). SWEET-Cat, for the first time described in Santos et al. (2013), is a continuously updated catalogue of stellar parameters for planet-hosting stars derived, whenever possible, using the same methodology. A very recent version of the catalogue, whose parameters were re-derived using better quality spectra and following the same homogeneous procedure, is available (see Sousa et al. 2021). In the new version of the catalogue, recent *Gaia* EDR3 parallaxes were also considered to derive accurate surface gravity of the host stars.

As a result of the comparison of our $T_{\rm eff}$, $\log g$, and [Fe/H], and $v \sin i$ with the values given by the literature and listed in Table 4, the standard deviation of the difference is $60-90$ K, $0.07-0.23$ dex, $0.04-0.11$ dex, and $\sim 0.5-0.7$ km s^{-1}, respectively. For the microturbulence velocity, small differences are present among the comparisons with the two versions of SWEET-Cat (see Table 4), while within the discovery papers, most values of this parameter were fixed, and thus we cannot make a meaningful comparison; however, we can consider the relationship by Adibekyan et al. (2012a), which is based on the dependence of ξ on $T_{\rm eff}$ and $\log g$ for stars with $4500-6500$ K, $3.0-5.0$ in $\log g$, and $-1.4 <$ [Fe/H] < 0.5 dex. We find a very good agreement between the values computed through the mentioned relationship and those derived through our MOOG analysis, with mean difference of 0.10 ± 0.18 km s^{-1}.

Surface gravities were also derived by Mortier et al. (2013) and Sousa et al. (2021) using alternative methods to those based on spectroscopy. In particular, considering the surface gravities derived by Mortier et al. (2013) for 11 targets in common with our sample using a method based on photometric light curves and the previous version of the SWEET-Cat, the difference with respect to our values is of 0.04 ± 0.11 dex (see the inset in the second panel of Fig. B.1), while considering the $\log g$ derived by Sousa et al. (2021) through *Gaia* parallaxes, the standard deviations strongly improve with respect to the spectroscopic values listed by the authors, becoming 0.09 ± 0.09 dex. Therefore, our analysis based on a careful method leads to $\log g$ results that are very close to the values derived in accurate ways (through transit light curves or *Gaia* parallaxes), even if we are aware that the kind of analysis performed in this work is very

time-consuming and cannot be easily applied to surveys of hundreds to thousands of targets. A similar method to derive trigonometric $\log g$ is applied in Brucalassi et al. (2021) for ~ 150 targets within the ARIEL reference sample (see also Tinetti et al. 2021; Danielski et al. 2021; Magrini et al. 2022). Due to the high quality of the *Gaia* parallax, the authors suggest adopting trigonometric $\log g$ as a viable possibility for big stellar samples for which some spectroscopic methods based on automatic tools tend to under- or overestimate the surface gravity at low and high temperatures.

Concerning the iron abundances, from Fig. B.1 we recognize a presence of most discarding values when the comparison is made with respect to the discovery papers. In particular, the targets with a difference of more than 1σ are those from which the microturbulence velocity was not derived or was fixed (i.e., XO-2S, TRES-4, Qatar-2, HAT-P-20) or for part of the WASP sample. For this subsample of WASP targets (namely, WASP-38, WASP-60, WASP-54, WASP-39), $T_{\rm eff}$ and $\log g$ were derived via a method based on different strong lines; by chance, this method seems to lead to lower $T_{\rm eff}$, and therefore lower [Fe/H] than our values. We do not go deeper into detail because we are aware that these analyses date back to more than ten years ago. Here, we only note that the most recent analysis points toward findings that are more similar to our results.

Mortier et al. (2013) and Brewer et al. (2016) respectively measured abundances of 12 and 14 elements other than iron. For the 11 targets in common with Mortier et al. (2013), we find a mean difference in [X/H] of -0.01 ± 0.07 dex for Al, Ca, Co, Cr, Cr II, Mg, Mn, Na, Ni, Sc II, Si, Ti, Ti II, and V, while for the five targets in common with Brewer et al. (2016) we find a mean difference in elemental abundances of C, N, O, Na, Mg, Al, Si, Ca, Ti, V, Cr, Mn, Ni, and Y of 0.02 ± 0.04 dex. Furthermore, Burke et al. (2007) derived Na, Si, Ti, and Ni abundances for the XO-2 binary components; Teske et al. (2014) measured C, O, and Ni for XO-2N, XO-2S, and TRES-4; and Teske et al. (2019) obtained C, O, Mg, Si, and Ni abundances for HAT-P-15 and HAT-P-17. Comparing our results with those achieved by these authors, we find mean differences of 0.03 ± 0.09, -0.04 ± 0.08, and 0.00 ± 0.07 dex with respect to Burke et al. (2007) and Teske et al. (2014, 2019), respectively. Therefore, a general agreement between our abundance values and those from the literature is obtained for the targets in common.

4. Results and discussion

4.1. [X/H] versus [Fe/H]

The [X/H] (and [X/Fe]) versus [Fe/H] relations are generally used to study the Galactic chemical evolution since iron is a good
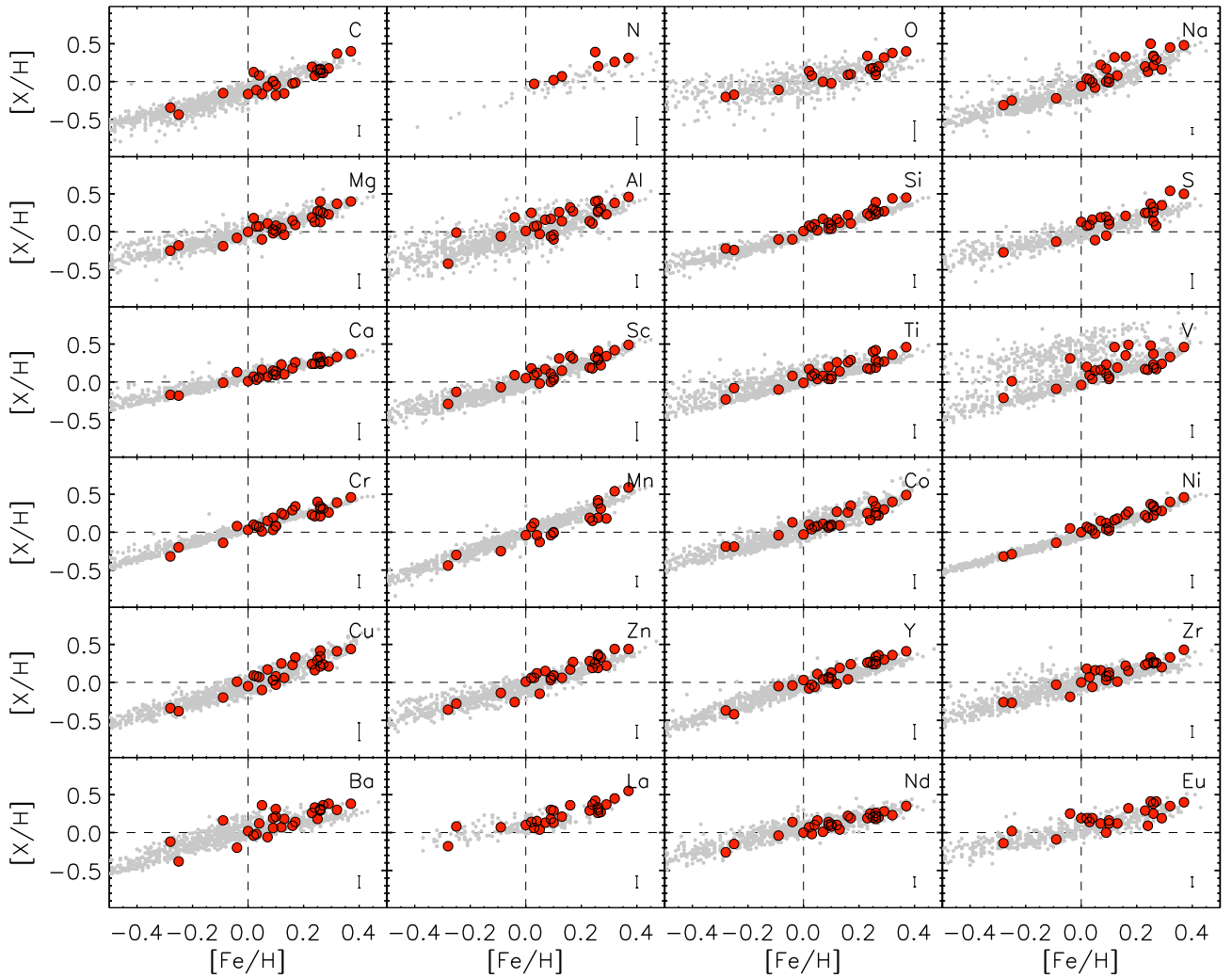
Fig. 4. [X/H] vs. [Fe/H] for our sample. C from Suárez-Andrés et al. (2017) for ∼4400−6800 K warm targets; N from Suárez-Andrés et al. (2016) for stars with $T_{\rm eff}$ ∼ 4500−6500 K; O from Bertran de Lis et al. (2015) for $T_{\rm eff}$ ∼ 5200−6800 K; Na, Mg, Al, Si, Ca, Sc, Ti, V, Cr, Mn, Co, and Ni from Adibekyan et al. (2012c) for targets with $T_{\rm eff}$ around 4500–6800 K; S from Costa Silva et al. (2020) for 4900–6800 K; Cu, Zn, Y, Zr, Ba, Nd, and Eu from Delgado Mena et al. (2018) for stars with 4500–6800 K; and La from Mishenina et al. (2016) for 4800–6200 K warm stars are overplotted with gray points. The La values were shifted by 0.2 dex. Mean error on [X/H] is shown in the bottom right corner of each panel, while solar values are indicated by dashed lines.

chronological indicator of nucleosynthesis. In Fig. 4 we show the [X/H] values for all derived elemental abundances versus [Fe/H]; in Fig. C.1 we show [X/Fe] versus [Fe/H]. We also overplot in gray the abundances of FGK dwarf stars observed within the HARPS at ESO GTO planet search program or with ELODIE at OHP. Studying FGK dwarfs is very useful because they contain information about the history of the evolution of chemical abundances in the Galaxy. Low-mass stars have long lifetimes indeed, and their atmospheres have preserved much of their original chemical composition (e.g., Adibekyan et al. 2012c).

We note that for some iron-peak elements, like [Cr/H] and [Ni/H], which are synthesized by SNIa explosions, and some α-elements (like [Si/H] and [Ca/H]), which are mostly produced in the aftermath of type II SNe explosions with small contributions from type Ia SNe, we obtain low dispersion for the whole range of [Fe/H], as for the dwarfs in the Galactic disk. Other elements, like sodium and aluminum, mostly produced through Ne and Mg burning in massive stars, show greater dispersion, as observed in the literature. Moreover, abundance ratios like [Al/Fe], [Sc/Fe],

[V/Fe], [Co/Fe], and [Ni/Fe] show a rise for [Fe/H] $\gtrsim$ 0.2, as observed in thin disk stars (see Adibekyan et al. 2012c). Here we cannot conclude whether the observed dispersions are intrinsic or due, at least in part, to statistical or methodological reasons (e.g., number of lines, SNR). We only highlight how for all elements the general pattern of [X/H] and [X/Fe] with the iron abundance is similar to those of the sample of dwarf stars in the Galactic disk, without clear evidence of peculiar behavior for our planet-host stars when compared with field stars. Therefore, the [X/H]-[Fe/H] trends of our sample seem to reflect the Galactic chemical evolution in the solar neighborhood.

4.2. Elemental abundance versus condensation temperature

In Fig. 5 we plot for each star the elemental abundance [X/H] as a function of the condensation temperature $T_{\rm cond}$, from the warmest target to the coolest. It was indeed reported that stars hosting high-mass planets are expected to be more enriched in refractory elements (i.e., elements with high condensation
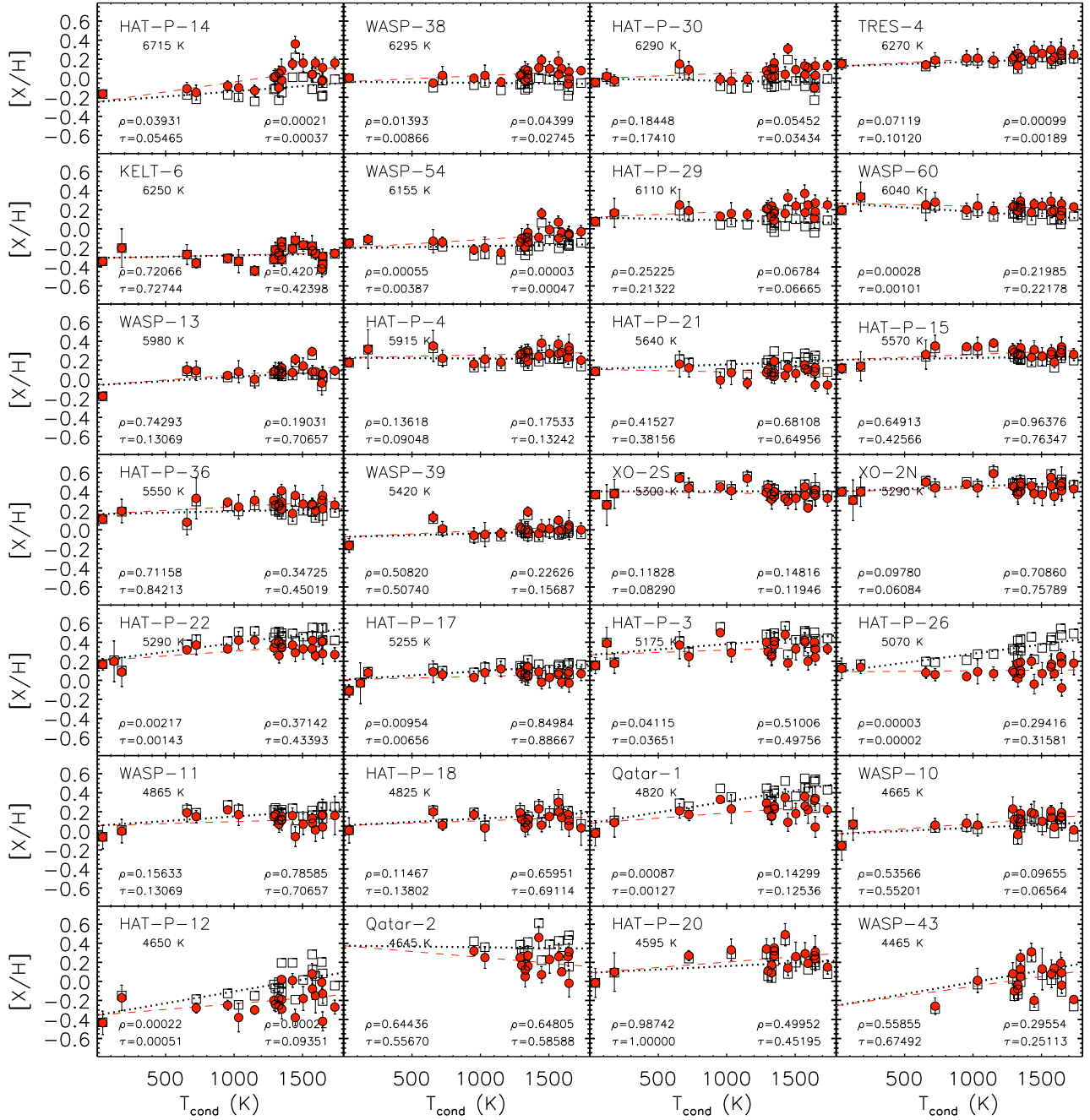
Fig. 5. [X/H] vs. T_{cond} for all targets from the warmest HAT-P-14 to the coolest WASP-43. Open squares (together with black dotted line) and filled dots (together with red dashed line) correspond to the abundance values with and without the GCE correction. ρ and τ in all panels are the Spearman and Kendall significance after (*left corner*) and before (*right corner*) GCE removal.

temperatures) and deficient in low T_{cond} volatile elements (e.g., Smith et al. 2001). This should happen because any accretion event, occurring very close to the star (i.e., in high-temperature environments) would add refractory elements, which condense at high T_{cond} with respect to volatiles (see, e.g., Sozzetti et al. 2006, and references therein). Similarly, Meléndez et al. (2009) concluded that solar twins without close-in giant planets chemically resemble the Sun, with depletion of refractory elements relative to the volatiles, suggesting that the presence of such planets might prevent the formation of an Earth-sized planet. Revealing these trends requires developing a very accurate differential analyses that is precise for binary systems (e.g., Gratton et al. 2001; Ramírez et al. 2011; Liu et al. 2014; Teske et al. 2015;

Biazzo et al. 2015; Maia et al. 2019) and members of stellar clusters (e.g., Yong et al. 2013) or through the use of a set of comparison stars (Liu et al. 2020; Tautvaišienė et al. 2022) because many observational uncertainties can be considered common-mode effects. If no comparison target is available, an unambiguous explanation for these trends is difficult to reach because they could also reflect the wide diversity of exoplanetary systems, as well as a variety of scenarios which could occur within the circumstellar disk (Spina et al. 2016b), or could be associated with the correlation of elemental abundances with the age and birthplace in the Galaxy (e.g., Adibekyan et al. 2014). González Hernández et al. (2013) have found that after removing the Galactic chemical evolution effects from a sample of

main-sequence objects, stars with and without planets show similar mean abundance patterns. We therefore applied an approach similar to the latter authors and adopted Spina et al. (2016a) for the correction of Galactic chemical evolution (GCE). In Fig. 5 we show the [X/H] abundances as a function of T_{cond} before (filled dots and dashed lines) and after (open squares and dotted lines) the removal of the GCE effects. The Spearman (ρ) and Kendall (τ) statistical significance computed with IDL[6] for the linear regression analysis before and after the GCE removal are displayed respectively in the bottom right and bottom left corners of the plots. Excluding Qatar-2 and WASP-43 for which we could not measure the abundances of volatile elements, among the other 26 targets there are 10 showing a trend after the GCE removal, with both ρ and τ lower than 0.05, and a wide range of planetary masses (from $0.06\,M_J$ to $2.6\,M_J$) and effective temperatures (from 4650 to 6715 K). In particular, HAT-P-12 and HAT-P-26, respectively hosting planets with $M_p \sim 0.2\,M_J$ and $0.06\,M_J$, show the most pronounced significant trend at a level of $\rho \sim \tau \sim 2$–3×10^{-5} up to 2–5×10^{-4} and among the highest values of positive slopes, while WASP-60 (with a planet of $0.5\,M_J$) is the only one within this subsample of ten targets showing a negative trend (i.e., decreasing refractory-to-volatile abundance ratios). On the one hand, we note that HAT-P-26 and HAT-P-12 are also targets with kinematic properties consistent with transition thin-thick disk (see Sect. 4.3) and with high values of [α/Fe] and Mg/Si (see Sect. 4.7), which, together with the possible [X/H]-T_{cond} trend, could indicate a pattern in the formation of the nuclei of their planets. On the other hand, we note that the binary components XO-2N and XO-2S, here analyzed as single stars, do not show a reliable correlation between elemental abundances and T_{cond}, while precise and accurate differential analysis demonstrated that the difference in elemental abundance between these two binary components shows a trend with the condensations temperature indicating possible ingestion of material by XO-2N or depletion in XO-2S (see Teske et al. 2015; Biazzo et al. 2015). Finally, excluding Qatar-2 and WASP-43 for which we could not measure elemental abundance of volatiles, we find higher values of T_{cond}-[X/H] slopes for cooler and older stars (see Sect. 4.4) with higher $\log g$, regardless of planetary mass and not evident without the GCE removal. We also find tentative evidence that stars with smaller galactocentric distance and greater Galactic eccentricity (see Sect. 4.3) have steeper slopes. Similar results were also found by other authors (e.g., Adibekyan et al. 2014; Tautvaišienė et al. 2022). In other words, stellar parameters and Galactic position are crucial to establishing the stellar chemical pattern of the stars and only a strictly differential analysis (like those performed for binary stars) can remove spurious trends and help to draw definitive conclusions, which is not the case in this work.

4.3. Chemical and kinematic properties

To study possible chemokinematic peculiarities of planet-hosting stars, we computed the stellar Galactic space velocities. The space velocity components UVW were derived with respect to the local standard of rest (LSR), correcting for the solar motion derived by Coşkunoğlu et al. (2011): ($U_\odot$, $V_\odot$, $W_\odot$) = (−8.50, 13.38, 6.49) km s^{-1}. Parallaxes (π) and propers motions (μ_α, μ_δ) were taken from *Gaia* EDR3 (Gaia Collaboration 2016, 2021), mean radial velocities ($\langle V_{rad} \rangle$) were obtained from the HARPS-N spectra, and ICRS coordinates

at epoch=2000 were taken from the SIMBAD Astronomical Database. We considered the general outline of Johnson & Soderblom (1987) in a left-hand coordinate system (i.e., with U pointing toward the Galactic anti-center, V toward the local direction of rotation in the plane of the Galaxy, and W toward the north Galactic pole). The uncertainties were obtained considering the prescriptions by Gagné et al. (2014), thus we used the full covariance matrix taking into account the error contributions of V_{rad}, π, μ_α, and μ_δ. Combining the measurement errors on parallaxes, proper motions, and radial velocities, the resulting average uncertainties in the U, V, W velocities are about 0.15 km s^{-1}. The values derived for each target are listed in Table A.3 and the Boettlinger diagram in the (U, V) plane is shown in the left panel of Fig. 6, where the boundary separating the young disk (YD) and the old disk (OD) stars according to Eggen (1996) is displayed with a solid line. The YD locus contains associations younger than ~1 Gyr (see Gagné et al. 2018). Nine targets, namely HAT-P-14, TRES-4, WASP-54, WASP-13, HAT-P-3, WASP-11, HAT-P-18, WASP-10, and HAT-P-20, seem to belong to the young disk, and three others (WASP-43, HAT-P-4, WASP-38) are very close to the YD boundary. In the right panel of the same figure we show the Toomre diagram, which is a representation of the combined vertical and radial kinetic energies versus the rotational energy. Low-velocity stars, within a total velocity $v_{tot} = (U_{LSR}^2 + V_{LSR}^2 + W_{LSR}^2)^{1/2} = 50$ km s^{-1} are, to a first approximation, mainly thin disk stars, while stars with $70 \lesssim v_{tot} \lesssim 180$ km s^{-1} are likely to be thick disk stars (see Bensby et al. 2014, and references therein). Eleven of our targets, namely HAT-P-14, WASP-38, HAT-P-29, WASP-54, WASP-13, HAT-P-3, WASP-11, HAT-P-18, WASP-10, HAT-P-20, and WASP-43, are very close to the Sun, with $v_{tot} \lesssim 20$ km s^{-1}, while five exoplanet-hosting stars (XO-2N, XO-2S, Qatar-2, HAT-P-26, HAT-P-12) have $v_{tot} > 70$ km s^{-1}, compatible with thick disk stars.

We also calculated the thick-to-thin disk probability ratios. In particular, we considered the prescriptions of Bensby et al. (2014) for the Gaussian distributions of random velocities of the different stellar populations. To get the probability D and TD for the thin and thick disk that a given star belongs to a specific population, we considered the asymmetric drift, the velocity dispersion, and the fractions of each population listed in their Table A.1. By then dividing the thick disk probability with the thin disk probability, we get the probability for the thick disk-to-thin disk (TD/D) membership. Bensby et al. (2014) require that for a star to be a candidate thick disk star its probability must be at least twice that of being a thin disk star (i.e., $TD/D > 2$), and vice versa for a candidate thin disk star $TD/D < 0.5$. All our targets show $TD/D < 0.5$ with the exception of five stars: two targets with probability ratios between the thin and thick disks (i.e., HAT-P-21 and HAT-P-26) with $TD/D \sim 0.5$; three targets with probabilities consistent with the thick disk, namely the star HAT-P-12 with a value of ~3.7, and the XO-2 binary system with $TD/D \sim 13$. All targets within or near the YD boundary show TD/D close to zero. The same occurs for targets with $v_{tot} \lesssim 20$ km s^{-1}.

Following Bensby et al. (2014), with the aim to further investigate the chemokinematic properties of our sample, we show in Fig. 7 the [Fe/Ti]–[Ti/H] abundance trend. All targets with $TD/D > 0.5$ (XO-2N, XO-2S, HAT-P-21, HAT-P-26, HAT-P-12) are placed below [Fe/Ti] = 0. Moreover, we have also coded the symbols with an empty yellow star when the chemical stellar age is greater than the median value of the entire sample (i.e., ~5.5 Gyr; see Sect. 4.4 for the age determination). It is evident that the [Fe/Ti] abundance signature has the same structure as
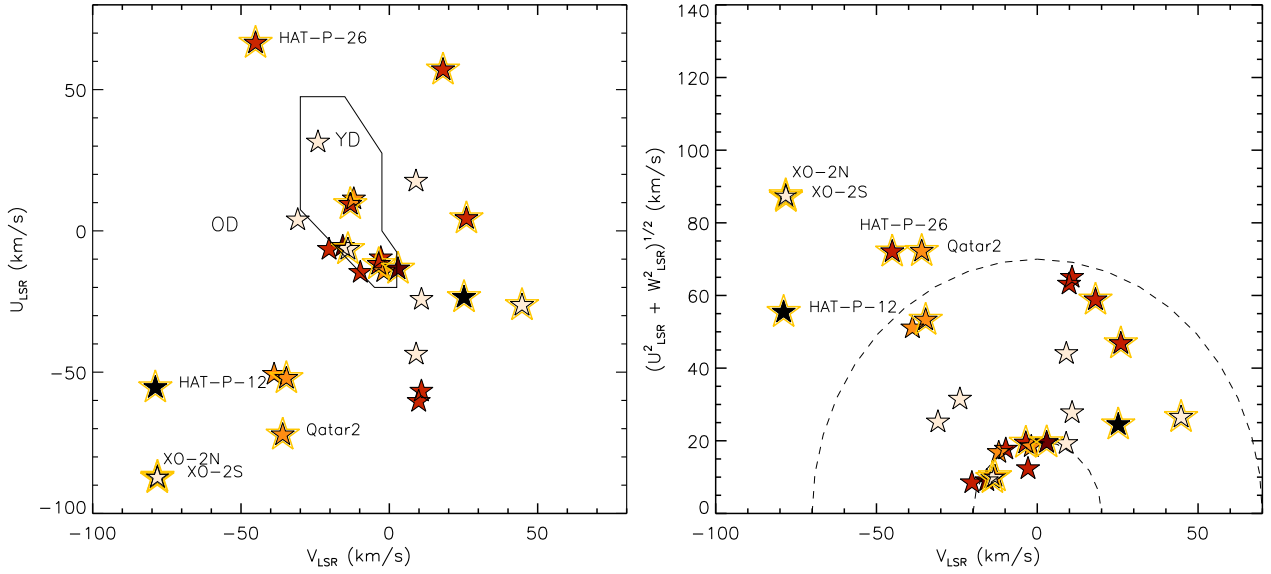

Fig. 6. Boettlinger and Toomre diagrams for our planet-hosting stars. Star symbols are color-coded following the same [Fe/H] bins as in Fig. 3. Empty yellow stars surround the targets with stellar ages greater than the median value of the sample (i.e., ~5.5 Gyr). The errors in both panels are within the symbol dimension. *Left panel*: solid line represents the boundary separating young disk (YD) and old disk (OD) stars in the (U, V) plane according to Eggen (1996). *Right panel*: dashed lines indicate constant peculiar total velocities $v_{tot} = (U^2_{LSR} + V^2_{LSR} + W^2_{LSR})^{1/2} = 20$ and $70\,km\,s^{-1}$. Stars with $v_{tot} > 70\,km\,s^{-1}$ are labeled.
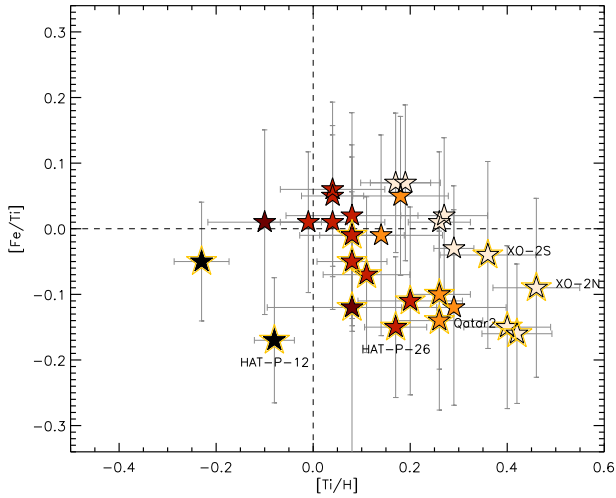
Fig. 7. [Fe/Ti] vs. [Ti/H] abundance trends. The stars are color-coded according to their [Fe/H], as in Fig. 3. Empty yellow stars surround the targets with stellar ages greater than the median value of the sample (i.e., ~5.5 Gyr). Dashed lines represent the solar values. Stars with $v_{tot} > 70\,km\,s^{-1}$ are labeled.

the age, with stars older than ~5.5 Gyr having [Fe/Ti] < 0.0. Moreover, most of the targets with [Fe/Ti] < 0.0 show different kinematic positions in the Toomre diagram when compared to the targets with [Fe/Ti] ≥ 0.0, with mean v_{tot} greater than about 20 km s^{-1}, with few exceptions. Hence, there are kinematically hot stars that are older and α-enhanced (i.e., with higher values of Ti), as well as kinematically cold stars that are younger and less α-enhanced, in line with what found by Bensby et al. (2014) for dwarf thin and thick disk stars in the solar neighborhood. We also note that within the four stars hosting planets with masses smaller than 5 M_{Nep} (i.e., XO-2S, HAT-P-26, HAT-P-18, HAT-P-12) all but HAT-P-18 show $v_{tot} > 20$ km s^{-1}. Moreover, their

mean distance from the Sun is smaller (by more than 60 pc) than that of stars hosting planets with higher masses. Similar results were found by Adibekyan et al. (2012b), who noted that, as expected, low-mass planets are easier to find at smaller distances due to the higher apparent magnitudes of their hosts. We therefore used a similar approach to that proposed by these authors. In particular, we calculated the maximum height a star can reach above the Galactic plane (Z_{max}), the current Galactic eccentricity (e_G), the peri-/apo- (R_{peri}, R_{apo}) center radii of an orbit, and the galactocentric distance (R_{GC}) with the `galpy`[7] package, a python package for Galactic-dynamics calculations. We assumed the built-in model `MWpotential2014` for the Milky Way's gravitational potential (see Bovy 2015). We set the distance of the Sun from the Galactic center to $R_0 = 8.0$ kpc (Bovy et al. 2012) and its height above the plane to $z_0 = 0.025$ kpc (Jurić et al. 2008), and used the parallaxes and proper motions from *Gaia* EDR3 to transform the celestial coordinates in galactocentric radius and height above the Galactic plane. We also used our mean radial velocities from HARPS-N to obtain the orbital parameters and considered the chemical ages as derived in Sect. 4.4. Table A.3, together with *UVW* velocities and *TD/D* probabilities, also lists the output results from the `galpy` package.

First, we note that all targets with $TD/D \gtrsim 0.5$ also show $|\Delta(R_{mean} - R_{GC})| \gtrsim 1$, where R_{mean} is the mean position of the stellar Galactic orbits (calculated as the average of R_{peri} and R_{apo}). This could indicate that stars with R_{mean} very different from R_{GC} could have experienced greater migration and therefore could have a higher probability of belonging to the thin-thick disk transition or thick disk (see Magrini et al. 2022; and references therein). Then, we find that on average stars hosting planets with masses lower than 5 M_{Nep} have higher Galactic eccentricity (by ~0.2) and greater age (by ~5 Gyr), while the difference in Z_{max} of only ~45 pc is within the average uncertainties (of around 150 pc). These low-mass planet-hosting stars also have
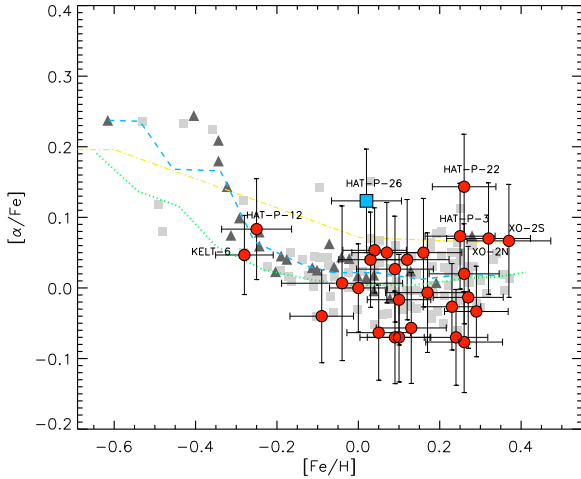
---

[7] http://github.com/jobovy/galpy

Fig. 8. [α/Fe] vs. [Fe/H] for our exoplanet-hosting sample. Dots refer to the massive-planet hosts, while the square is the position of the Neptunian host HAT-P-26 ($M_p < 30\,M_\oplus$). The gray squares and triangles refer to the Jovian hosts and the stars hosting exclusively Neptunians and super-Earths, respectively, by Adibekyan et al. (2012b). The dashed blue and dotted green lines respectively represent the mean distributions of the planet host and non-host samples by the same authors. The dot-dashed yellow line separates the stars with high- and low-α content, as found by Adibekyan et al. (2012c). The positions of the two most metal-poor and α-enhanced targets within our sample are labeled.

lower V_{LSR} and W_{LSR} space velocity components than stars hosting higher-mass planets. Moreover, comparing their [Mg/Fe], [Si/Fe], and [Ti/Fe] ratios, we find that the stars with $M_p < 5\,M_{Nep}$ planets are more enhanced by Mg (with a difference of 0.09 dex), by Si (difference of 0.04 dex), and Ti (difference of 0.09 dex) when compared to stars with higher-mass planets. These elements are all tracers of the rocky component of the cores of the Neptune-mass planets, thus possibly indicating that Neptunian and/or super-Earth host stars tend to belong to the thicker disk when compared with Jupiter-mass hosting stars. Even if we are cautious about these findings because they could depend on several selection effects (e.g., stellar magnetic activity), our results seem to give support to the findings by Adibekyan et al. (2012b), according to which stars hosting low-mass planets tend to belong to a thicker disk.

In Fig. 8 we plot [α/Fe][8] against [Fe/H] for our sample, where the position of the star HAT-P-26 hosting a Neptunian or super-Earth planet (i.e., with mass <30 $M_\oplus$) is represented with a blue square. In the same plot, we show the results by Adibekyan et al. (2012b), who analyzed 1111 nearby FGK dwarfs observed in the context of the HARPS GTO program, 135 of which hosting high-mass planets (gray squares), and Neptunians and/or super-Earths with masses <30 $M_\oplus$ (gray triangles). They found that planet-hosting stars show a continuous increase in [α/Fe] with decreasing [Fe/H] at metallicities from −0.2 to −0.3 dex (starting from the thin disk, they rise toward the thick disk), while the thin and thick disk stars without planets are separated very well by their [α/Fe] ratios (see dashed and dotted lines). In this metallicity regime we have two targets (KELT-6 and HAT-P-12). KELT-6 shows UV values compatible with the Galactic young disk, it is close to the circle with total velocity

---

[8] The α index refers to the average abundance of Mg, Si, and Ti, i.e., [α/Fe] = $\frac{1}{3}$([Mg/Fe]+[Si/Fe]+[Ti/Fe]). Calcium was not included because for [Fe/H] > 0 the [Ca/Fe] trend for dwarf stars in the Galactic disk differs from that of Mg, Si, and Ti (see Adibekyan et al. 2012c).

of 20 km s^{-1} in the Toomre diagram, and the TD/D ratio is very low (∼0.02), thus appearing to belong to the thin disk (see Fig. 6). HAT-P-12 shows a relatively high proper motion, it is compatible with thick disk stars in the Toomre diagram, and $TD/D \sim 3.7$ (i.e., slightly higher than the thick disk threshold). In conclusion, our chemokinematic analysis for these two targets seems to be consistent with KELT-6 clearly belonging to the thin disk and HAT-P-12 between the thin and thick disk. Moreover, our findings support the conclusion by Adibekyan et al. (2012b), according to which planet-hosting metal-poor stars (like KELT-6) can have high [α/Fe] even belonging to the thin disk.

Furthermore, we note that the only target within our sample hosting a Neptunian and/or super-Earth planet, namely the solar-metallicity star HAT-P-26, shows the highest value of [α/Fe], when compared to the sample by Adibekyan et al. (2012b) with similar planetary masses and iron abundance (triangles in Fig. 8). The relatively high abundance values of α elements for this target are similar to those of their Neptunian–super-Earth host stars with iron abundance values around −0.3 dex. Its position in Fig. 8 is indeed consistent with the stars with high-α content, as defined by Adibekyan et al. (2012c). Again, this target shows high space velocities (see Fig. 6) and in the Toomre diagram, accordingly to Bensby et al. (2014), it is in the region populated by thick disk stars. Finally, its Z_{max} is around 565 pc (one of the highest in the sample) and the TD/D ratio is ∼0.5. Therefore, the chemokinematic analysis for this target seems to be consistent with a star close to the thin–thick disk transition, also supported by its relatively old age (see Sect. 4.4).

Two other targets with α content higher than the limit defined by Adibekyan et al. (2012c) are HAT-P-22 and HAT-P-3. The kinematic position in the (U, V) plane and the Toomre diagram for the super-solar star HAT-P-3 are consistent with the thin disk, also supported by the TD/D ratio close to zero. HAT-P-22 shows $v_{tot} \sim 50$ km s^{-1} and a TD/D ratio of ∼0.08. Again, both components of the XO-2 binary system are slightly above the above-mentioned chemical limit and also have high Galactic space velocities. Moreover, their position in the Toomre diagram is within the locus of the thick disk stars, and the TD/D ratio is ∼13, higher than the threshold established by Bensby et al. (2014) for potential thick disk stars. From the analysis of the Galactic orbits we find an eccentric orbit ($e_G \sim 0.44$) with a maximum height above the Galactic plane of ∼104 pc. The relatively low Z_{max} led in the past to conclude that the binary system is confined to the Galactic thin disk (see Burke et al. 2007; Damasso et al. 2015a), but the other chemokinematic indicators suggest that the XO-2 binary system is at least in the thin disk–thick disk transition.

4.4. Chemical and isochronal ages

We computed stellar ages using elemental abundance ratios. It was indeed demonstrated that abundance ratios of pairs of elements produced over different timescales (e.g., [Y/Mg], [Y/Al]) can be used as valuable indicators of stellar age (Nissen 2015). Their [X/Fe] ratios show opposite behaviors with respect to stellar age (e.g., [Mg/Fe] and [Y/Fe] abundances respectively decrease and increase with stellar age). Therefore, their ratio, for instance [Y/Mg], shows a steep increasing trend with stellar age (see Casali et al. 2020, and references therein). The latter authors derived relations in the form [A/B] = $c + x_1 \cdot$ [Fe/H] + $x_2 \cdot Age$, with [A/B] generic abundance ratio used as a chemical clock (see their paper for a wide description of the method). Here we considered the multivariate linear regression parameters c, x_1, and x_2 for all abundance ratios in common
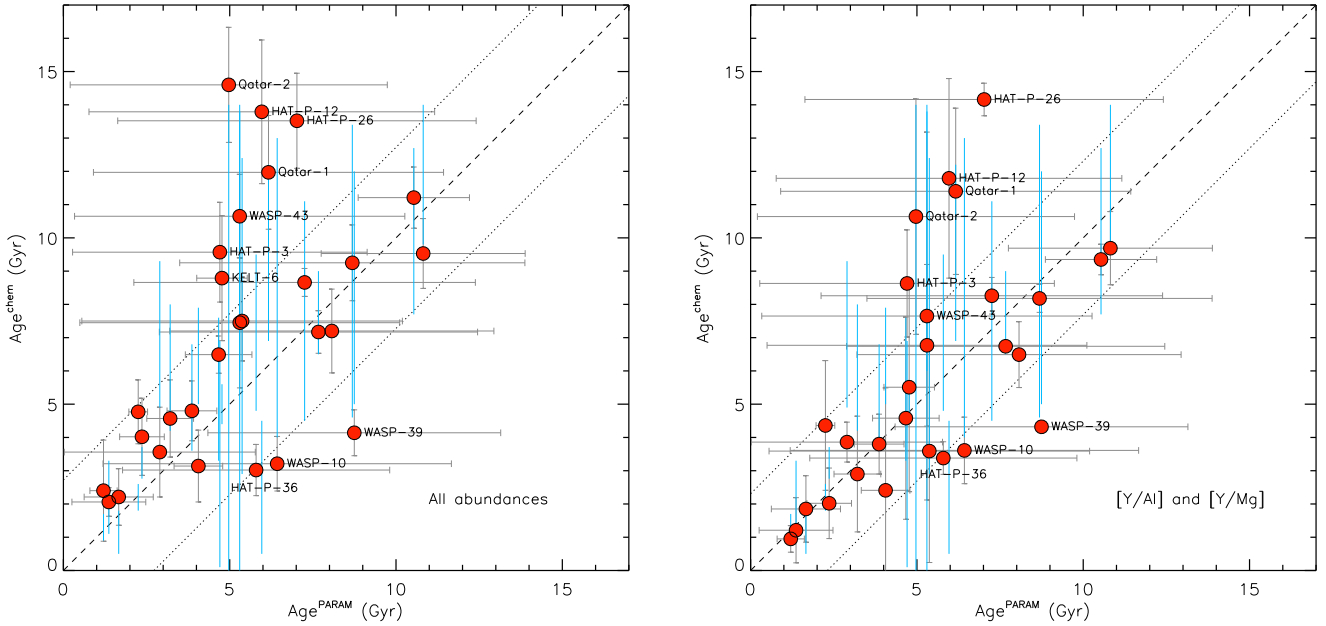
Fig. 9. Comparison of the ages derived through abundance ratios and those inferred from the PARSEC models. We plot the results obtained considering all abundance ratios in common with Casali et al. (2020) (*left panel*) and the two best abundances ratios [Y/Al] and [Y/Mg] (*right panel*). Dashed line are the 1:1 relation, while the dotted lines represent the $\pm 1\sigma$ levels from the average. Stars outside the $\pm 1\sigma$ locus are marked. Light blue bars represent the range of values by Bonomo et al. (2017) obtained through Yonsei-Yale evolutionary tracks.

with Casali et al. (2020): [Y/Mg], [Y/Al], [Y/Ti], [Y/Ca], [Y/Si], [Y/Sc], [Y/V], [Y/Co], [Y/Zn], and [Zn/Fe] (see their Table 6). We derived mean ages from all the abundance ratios and rejected those values discrepant by more than 1σ from the average.

Moreover, we also computed stellar ages (and masses) from isochrone fittings (and evolutionary tracks). We therefore considered the PARSEC[9] models by Bressan et al. (2012) and the PARAM interface[10] (version 1.3; da Silva et al. 2006). This code considers as input some observational parameters (effective temperature, parallax, apparent V magnitude, and iron abundance) to perform a Bayesian determination of the most likely stellar intrinsic properties, appropriately weighting all the isochrone sections that are compatible with the observational parameters. A flat distribution of ages with a range of 0.1–15 Gyr was considered as priors for the analysis. We considered as effective temperature and iron abundance those values we derived as described in Sect. 3.1. The parallax was taken from *Gaia* EDR3, while the V magnitude was computed from the *Gaia* EDR3 G magnitudes, G_{BP} and G_{RP} colors using the appropriate photometric relationships (Gaia Collaboration 2021) and the reddening maps by Capitanio et al. (2017).

In Fig. 9 the comparison between the ages obtained with all the abundance ratios as a function of the isochronal ages obtained from PARSEC models is shown. In the same figure the range of ages listed in Bonomo et al. (2017) for each star and derived through stellar evolutionary tracks is shown for comparison. We tried multiple combinations of abundance ratios to find the mean chemical ages by using the best abundance ratios discussed in Casali et al. (2020), and the better agreement with isochronal ages from PARSEC was found considering the two ratios [Y/Al] and [Y/Mg]. In Table 5 we list the chemical ages obtained by using all abundances and these two abundance ratios, together with the isochronal ages from the PARAM tool.

In particular, we find a mean difference between the ages derived from all the available abundance ratios and those obtained through PARSEC models of 2.7 Gyr with a standard deviation of 2.4 Gyr. Six targets (Qatar-2, HAT-P-12, HAT-P-26, Qatar-1, HAT-P-3, WASP-43) fall outside the 1σ limit, while three (KELT-6, WASP-10, WASP-39) are close to it. The comparison with Bonomo et al. (2017) gives an age difference of 2.9 Gyr with a standard deviation of 2.7 Gyr. If we consider the two best abundance ratios ([Y/Al] and [Y/Mg]; see, e.g., Casali et al. (2020), and references therein) the agreement is even better than that obtained using all abundance ratios, with a mean age difference of 2.0 Gyr and a standard deviation of 2.0 Gyr. In this case the position of Qatar-2, HAT-P-12, WASP-43, and KELT-6 is closer to that of the isochronal age, with a visibly improved general agreement. The comparison with Bonomo et al. (2017) in this case gives an age difference of 2.5 Gyr with a standard deviation of 2.3 Gyr. We note here that the most discrepant target, HAT-P-26, is also one of the stars with high values of space velocities (see Sect. 4.3), with $v_{tot} > 70\,\mathrm{km\,s^{-1}}$, and with the [$\alpha$/Fe] and TD/D ratios compatible with the thin to thick disk transition. This justifies its chemically old origin. Other stars (HAT-P-12, Qatar-1, Qatar-2) are in a region of the $\log g$-T_{eff} diagram for which the age determination from both the isochrones and the chemical indicators is problematic mainly due to their relatively cool effective temperature.

4.5. Lithium abundance

We find that seven targets show lithium in their spectra, with HAT-P-3 the most uncertain case (see Fig. 10). KELT-6 shows a value of ~1.2 dex; WASP-38, HAT-P-14, and WASP-13 have lithium abundances around 2 dex; and HAT-P-4 and HAT-P-30 have values $\log n(\mathrm{Li}) \sim 2.8$–3.0 dex. Lithium in WASP-38, WASP-13, HAT-P-4, and HAT-P-30 was also detected by Mortier et al. (2013) and Enoch et al. (2011), who measured abundances very close to our values. Our targets with lithium

---

[9] PAdova and TRieste Stellar Evolutionary Code.
[10] http://stev.oapd.inaf.it/cgi-bin/param_1.3

Table 5. Chemical ages derived through all abundance ratios (Col. (2)) and through [Y/Al] and [Y/Mg] ratios (Col. (3)).

Name	$\text{Age}_{\text{all}}^{\text{chem}}$ (Gyr)	$\text{Age}_{\text{[Y/Al],[Y/Mg]}}^{\text{chem}}$ (Gyr)	$\text{Age}^{\text{PARAM}}$ (Gyr)	$M_\star$ ($M_\odot$)
HAT-P-3	9.6 ± 1.5	8.6 ± 1.6	4.7 ± 4.4	0.88 ± 0.03
HAT-P-4	4.8 ± 0.9	3.8 ± 0.9	3.8 ± 0.7	1.28 ± 0.05
HAT-P-12	13.8 ± 2.2	11.8 ± 3.0	6.0 ± 5.2	0.69 ± 0.02
HAT-P-14	2.4 ± 1.5	1.0 ± 0.4	1.2 ± 0.4	1.41 ± 0.03
HAT-P-15	3.6 ± 1.4	3.9 ± 0.6	2.9 ± 2.9	0.98 ± 0.04
HAT-P-17	8.7 ± 0.4	8.3 ± 0.6	7.3 ± 5.1	0.87 ± 0.04
HAT-P-18	7.4 ± 2.0	6.8 ± 2.4	5.3 ± 4.8	0.78 ± 0.03
HAT-P-20	7.5 ± 1.2	3.6 ± 3.4	5.4 ± 4.9	0.74 ± 0.02
HAT-P-21	11.2 ± 0.9	9.4 ± 0.5	10.5 ± 1.7	0.97 ± 0.04
HAT-P-22	9.5 ± 1.1	9.7 ± 1.1	10.8 ± 3.1	0.92 ± 0.03
HAT-P-26	13.5 ± 1.4	14.2 ± 0.5	7.0 ± 5.4	0.84 ± 0.03
HAT-P-29	2.1 ± 0.4	1.2 ± 1.0	1.4 ± 1.1	1.20 ± 0.03
HAT-P-30	2.2 ± 0.8	1.9 ± 1.0	1.7 ± 1.0	1.25 ± 0.04
HAT-P-36	3.0 ± 0.8	3.3 ± 0.5	5.8 ± 4.0	1.00 ± 0.05
KELT-6	8.8 ± 1.9	5.5 ± 3.1	4.8 ± 0.8	1.14 ± 0.05
Qatar-1	12.0 ± 1.7	11.4 ± 2.5	6.2 ± 5.3	0.81 ± 0.03
Qatar-2	14.6 ± 1.7	10.6 ± 3.5	5.0 ± 4.8	0.74 ± 0.02
TRES-4	4.8 ± 1.0	4.4 ± 2.0	2.2 ± 0.3	1.46 ± 0.02
WASP-10	3.2 ± 0.8	3.6 ± 1.0	6.4 ± 5.2	0.77 ± 0.02
WASP-11	9.2 ± 1.1	8.2 ± 0.4	8.7 ± 5.2	0.81 ± 0.03
WASP-13	6.5 ± 0.6	4.6 ± 3.0	4.7 ± 1.0	1.19 ± 0.05
WASP-38	4.0 ± 1.2	2.0 ± 1.1	2.4 ± 0.7	1.27 ± 0.04
WASP-39	4.1 ± 0.7	4.3 ± 0.1	8.7 ± 4.4	0.89 ± 0.04
WASP-43	10.6 ± 1.3	7.7 ± 5.5	5.3 ± 5.0	0.65 ± 0.02
WASP-54	3.1 ± 1.1	2.4 ± 3.1	4.1 ± 0.7	1.23 ± 0.06
WASP-60	4.6 ± 1.2	2.9 ± 1.7	3.2 ± 0.7	1.24 ± 0.03
XO-2N	7.2 ± 0.6	6.7 ± 0.1	7.7 ± 4.8	0.94 ± 0.04
XO-2S	7.2 ± 1.3	6.5 ± 1.0	8.1 ± 4.9	0.94 ± 0.04

Notes. Columns 4 and 5 list the stellar ages and masses obtained from the PARAM tool.

are outside the region known as the lithium desert, located at $\sim$5900−6200 K and $\log n(\text{Li}) < 2$ dex (see Fig. 11), in agreement with Ramírez et al. (2012) and López-Valdivia et al. (2015). By chance, the number of stars with $T_{\text{eff}} > 5900$ K with lithium content higher than $\sim$2.0 dex (i.e., 5) exceeds the number of stars with depleted lithium (i.e., 1), in accordance with Pavlenko et al. (2018), and justified by their thinner envelopes. On the other hand, all targets with clearly detected lithium have $TD/D \leq 0.05$, with the most metal-poor KELT-6 having the lower value of $\log n(\text{Li})$. This behavior could also reflect the pattern observed for Galactic thin stars, in addition to the depletion dependences related to their different stellar parameters (see Ramírez et al. 2012).

We find, as expected, that the targets with lithium show on average higher $v \sin i$ ($\sim$5.0 km s^{-1}) than stars without lithium detected ($\sim$2.6 km s^{-1}), higher T_{eff} ($\sim$6090 K vs. $\sim$5260 K), and higher stellar mass ($\sim$1.10 $M_\odot$ vs. $\sim$0.97 $M_\odot$), lower $\log g$ (4.2 dex vs. 4.4 dex), lower [Fe/H] (0.08 dex vs. 0.13 dex), lower chemical age (3.9 Gyr vs. 6.7 Gyr), and lower planetary mass (1.1 M_{Jup} vs. 1.5 M_{Jup}). Moreover, within the sample with detected lithium, we recognize a tendency for the star with lower Li content (KELT-6) to be also that with a chemically derived older age. Similar dependence on lithium abundance on stellar parameters were also found by Delgado Mena et al. (2014) for solar twins observed with HARPS and by Pavlenko et al. (2018)

for CHEOPS dwarf stars. The dependence of Li abundance on T_{eff} and on stellar mass is mainly due to the fact that high T_{eff} (and therefore higher-mass) stars have thinner envelopes, which naturally leads to higher Li, while cooler stars have deeper convective envelopes which allow for Li to get into hot enough regions for processing to occur (see, e.g., the pioneering work by Boesgaard et al. 1998). The barely noticeable effect on $\log g$ could be due to stronger lithium depletion in the atmospheres of older stars (and therefore with higher surface gravity) or enhanced mixing in stars with deeper convective envelopes; alternatively, those stars with lower $\log g$ could be slightly evolved and thus their T_{eff} at the main sequence could have been higher; therefore, they did not destroy so much Li due to their thinner convective envelopes (see Pavlenko et al. 2018). The slightly lower mean [Fe/H] of stars with Li compared to stars without detectable lithium could be caused by deeper convective envelopes expected for high opacities or Galactic chemical evolution (see Delgado Mena et al. 2014, 2015). Even if our sample is biased toward relatively slow rotating stars, we observe a difference in $v \sin i$ between targets with and without lithium compatible with depletion induced by rotation, as suggested in the rotational evolution models by Bouvier (2008) and observed by Pavlenko et al. (2018) for CHEOPS dwarf stars with planets. We also find higher planetary masses for stars without lithium detected, which seems to indicate that destruction of Li is greater when the planet is more massive. Similar results were found by Delgado Mena et al. (2014), who suggested that this could be justified within a scenario where the disk is affecting the evolution of angular momentum, with a stronger effect for a more massive disk, a condition needed to form a giant planet (Bouvier 2008). Moreover, when a giant planet forms in the disk, the accretion processes are expected to be more frequent and violent and produce Li destruction because of the temperature increase at the base of the convective envelope (Baraffe et al. 2015).

In Fig. 11 we plot the lithium abundance versus T_{eff} and stellar age derived through chemical indicators. Despite the relatively wide T_{eff} range ($\sim$5200−6700 K), the plot shows an evident negative trend of Li abundance versus age, in which stars with higher lithium content show younger chemically derived ages. For the chemically old ($\sim$8 Gyr) star HAT-P-3 we cannot make conclusions about the possible age derived through the Li because of its upper limit in $\log n(\text{Li})$. KELT-6 is placed on the left of the warmest part of M67 members with similar T_{eff} and its age derived through [Y/Al] and [Y/Mg] elemental abundance ratios is 5.5 Gyr, consistent with the open cluster M67 (Pasquini et al. 2008). The position of WASP-13 within the T_{eff}-$\log n(\text{Li})$ diagram is compatible with M67 stars, giving support to the chemically derived age of $\sim$4.6 Gyr. HAT-P-4 and HAT-P-30 are placed close to the Hyades group, while their chemical age is $\sim$2−4 Gyr, with HAT-P-4 older than HAT-P-30. Finally, HAT-P-14 and WASP-38 appear to be respectively in the warm and in the cool side of the Hyades Li dip, with a chemical age of $\sim$1−2 Gyr.

Finally, in our fit of the lithium line we tried to include the ^{6}Li/^{7}Li ratio as a free parameter. This was done because the inclusion of this isotopic ratio improves the fit of the λ6707.8 Å line and also because the determination of ^{6}Li/^{7}Li would improve our knowledge of the stars in our sample. Standard and non-standard stellar evolution models predict in solar-type stars a destruction of ^{6}Li at the base of the convective envelope (Talon & Charbonnel 2005, and references therein), and hence the presence of ^{6}Li in the atmosphere of a planet-hosting star has been justified as indication of an external pollution process, like planetary material accretion or superflares around stars with hot Jupiters (e.g., Cuntz et al. 2000;
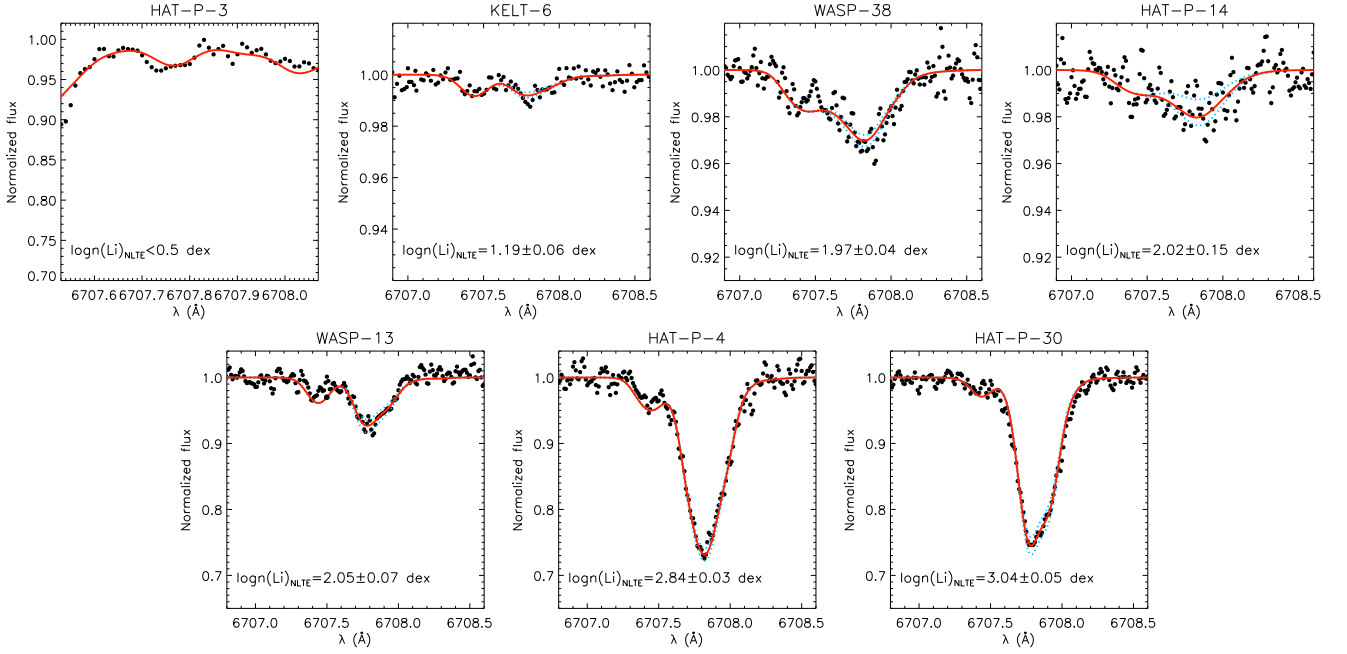
Fig. 10. Spectral synthesis around the Li region for the seven stars with detected lithium (with the exception of HAT-P-3 for which only an upper limit in Li abundance was derived). The best-fit NLTE $\log n(\text{Li})$ and its margins of error superimposed on the observed spectrum are shown with solid red and dotted light blue lines, respectively.

Israelian et al. 2001; Mott et al. 2017). On the other hand, no $^6\text{Li}/^7\text{Li}$ was detected in other stars with planets (Reddy et al. 2002; Ghezzi et al. 2009; Harutyunyan et al. 2018). Unfortunately, our spectra are not of sufficiently high SNR to determine $^6\text{Li}/^7\text{Li}$ ratio with high enough precision. Usually, the $^6\text{Li}/^7\text{Li}$ isotopic ratio is determined from analysis of spectra with $SNR >$ 600 (Mott et al. 2017). Trying to derive the $^6\text{Li}/^7\text{Li}$ ratio from our MOOG analysis (see Sect. 3.2), we tentatively find a $^6\text{Li}/^7\text{Li}$ value of around 0.07 for the solar spectrum, which is between the values of ∼0.05 and ∼0.08 derived for the Sun by Asplund et al. (2021) and Lang (1974), respectively. For our subsample with lithium detected, we infer from our analysis a $^6\text{Li}/^7\text{Li}$ lower than the solar value, with typical values ranging from ∼0.01−0.02 for HAT-P-3, KELT-6, and WASP-38 up to ∼0.03 for HAT-P-4, HAT-P-14, HAT-P-30, and WASP-13. Similar low values of $^6\text{Li}/^7\text{Li}$ ratios are compatible with null results, in the sense that we do not find a significant amount of ^6Li in our sample of stars with detected Li. We tried to use other line lists (like that by Meléndez et al. 2012) and obtained similar findings; therefore, we think that higher SNR is needed for more reliable $^6\text{Li}/^7\text{Li}$ measurements, as suggested by Mott et al. (2017).

4.6. Stellar carbon, nitrogen, oxygen, and sulfur abundances

As shown in Fig. 4, [C/H], [N/H], [O/H], and [S/H] abundances scale with iron, which is expected because massive-planet host stars are statistically enhanced in Fe. In Fig. 12 we plot the [C/α], [N/α], [O/α], and [S/α] ratios versus [Fe/H]. The figure shows that the position of our targets in the [X/α]–[Fe/H] plots for these elements are similar to those found in the literature for nearby FGK stars by Suárez-Andrés et al. (2017) for C, Suárez-Andrés et al. (2016) for N, Bertran de Lis et al. (2015) for O, and Costa Silva et al. (2020) for S. In particular, [C/α] for our targets is almost constant for super-solar metallicity, as also observed by Suárez-Andrés et al. (2017) for solar-type stars.

[O/α] shows a possible decreasing trend (with a Spearman statistical significance $\rho \sim 0.2$) with increasing iron abundance, as also found for FG-type stars observed within the HARPS GTO (gray dots; Bertran de Lis et al. 2015). This kind of trend is expected if O abundance scales with the iron abundance, as suggested above. Finally, hints of enhancements in sulfur are observed for the components of the XO-2 binary system (at [Fe/H] ∼ 0.3−0.4 dex).

As mentioned in the introduction, volatile elements like C, N, O, and S, can be used as proxy of the star–planet formation history (Turrini et al. 2021a). These authors have found that using the ratios of C/N, N/O, and C/O for the planets and for their hosting stars breaks the degeneracy in the formation and migration tracks of giant planets, while the ratio S/N provides an additional independent probe into the metallicity of giant planets and their accretion of solids. We computed for our stellar sample the mean elemental ratios for two different stellar metallicity regimes around the iron abundance peak of our targets, which is [Fe/H] ∼ 0.12 dex (see Table 6). As the comparison of these mean values highlights, the elemental ratios of interest for planetary studies can vary by as much as ∼10–20% between stars with different metallicity, for example with C/N going from values of around ∼2.8 for solar-metallicity or metal-poor targets up to ∼3.1 for super metal-rich targets. As such, the use of reference solar values would introduce significant biases in the interpretation of the planetary compositional data (see Turrini et al. 2021a,b). As an illustrative example, a planet with a C/N ratio of ∼3.4 or C/O ratio of ∼0.6 orbiting a star with metallicity belonging to the ≤1.3 $Z_\odot$ group would be interpreted as possessing a solar value of this ratio when compared to the Sun, while its C/N value could actually be ∼1.2 times and ∼1.3 times sub-stellar in C/N and C/O, respectively. Similar conclusions were recently drawn also by Jorge et al. (2022) for other elemental ratios (Fe/O, Si/O, Fe/S). The authors claim that planet formation scenarios should include the chemical abundance data of the host star and not
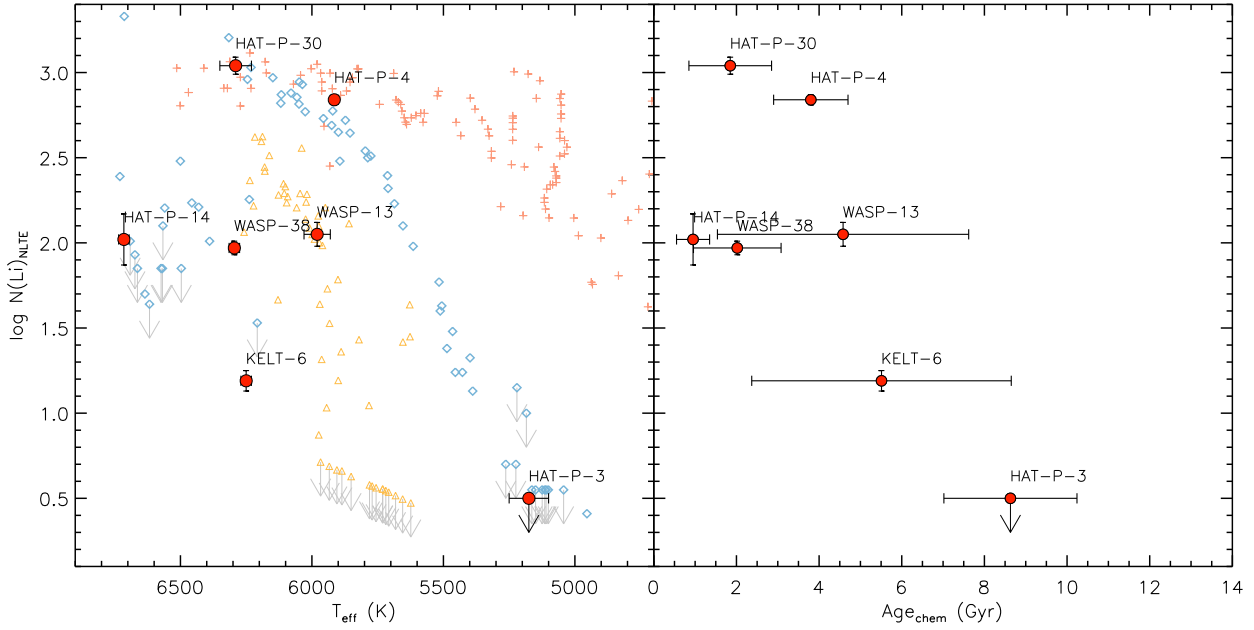
Fig. 11. Li abundance vs. effective temperature and chemical age derived considering the [Y/Al] and [Y/Mg] ratios as chemical clocks. In the *left panel* the position of members in the Pleiades (~100 Myr; Sestito & Randich 2005), Hyades (~600 Myr; Cummings et al. 2017), and M 67 (~4.5 Gyr; Pasquini et al. 2008) clusters are overplotted with red crosses, blue diamonds, and yellow triangles, respectively. Only the stars in our sample with the presence of the Li line are plotted.
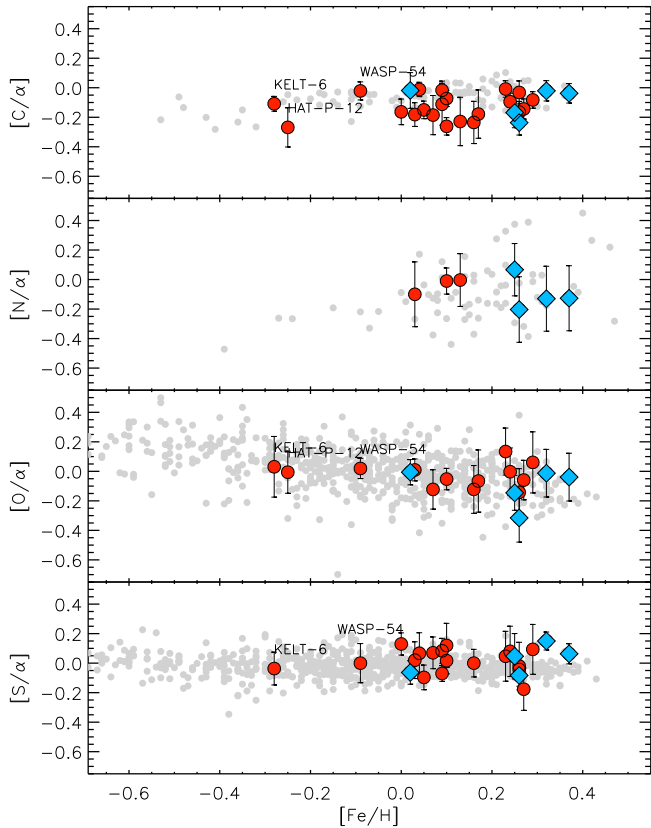

Fig. 12. Ratios of [C/α], [N/α], [O/α], and [S/α] vs. [Fe/H] for our targets. Blue diamonds indicate stars with a high content of [α/Fe] (as defined by the dot-dashed line in Fig. 8): HAT-P-26, HAT-P-22, XO-2N, XO-2S, and HAT-P-3. The overplotted gray points represent the values obtained by Suárez-Andrés et al. (2017), Suárez-Andrés et al. (2016), Bertran de Lis et al. (2015), and Costa Silva et al. (2020) for C, N, O, and S, respectively. Targets with [Fe/H] < 0.0 are labeled.

Table 6. Peak of the distributions of S/N, N/O, C/N, and C/O ratios for the targets divided into two different metallicity intervals around the mean [Fe/H] of our sample.

[Fe/H]	$Z_\star/Z_\odot$	S/N	N/O	C/N	C/O
		Solar Values			
0.00 ± 0.05	1	0.17 ± 0.08	0.17 ± 0.08	3.35 ± 0.08	0.57 ± 0.04
		Sample divided into two metallicity bins			
≤ 0.12	≤ 1.3	~0.23	~0.16	~2.84	~0.45
>0.12	>1.3	~0.25	~0.19	~3.09	~0.50

Notes. Mean solar values are also shown.

impose solar abundance values to study the bulk exoplanetary properties.

4.7. [Mg/Si] vs. [Fe/H] and Mg/Si vs. C/O

In Fig. 13 we show how the [Mg/Si] ratio depends on stellar iron abundance. We also overplot the results by Adibekyan et al. (2015) for planet-hosting stars, keeping in mind that the authors declared that they were not able to find differences between stars with and without high-mass planets. Our targets show values consistent with those by Adibekyan et al. (2015), with a few outliers that are placed at similar positions of undetected planet-hosting stars by the same authors (see their Fig. 1). Moreover, we note that the lowest-mass planet-hosting star in our sample, HAT-P-26, shows the highest [Mg/Si] ratio, in agreement with Adibekyan et al. (2015), who declare that low-mass planets are more prevalent around stars with high [Mg/Si]. This could be due to the fact that [Mg/Si] probably plays a very important role in the formation of low-mass planets; for example, high Mg abundances could mitigate the lower iron abundances or metallicities and make core accretion comparatively more efficient. Moreover,
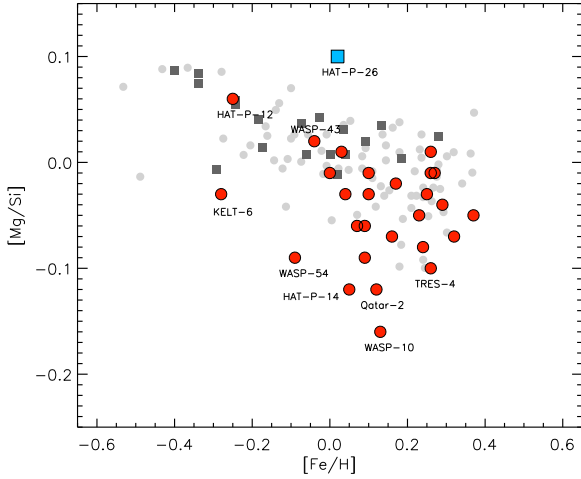
Fig. 13. [Mg/Si] vs. [Fe/H]. The blue square gives the position of the star hosting the planet with the lowest mass in the sample: HAT-P-26. The other labeled stars are those with [Fe/H] < 0.0 or with [Mg/Si] < −0.1. Mean errors on [Mg/H], [Si/H], and [Fe/H] are similar to each other (∼0.07 dex). Overplotted in gray are the results by Adibekyan et al. (2015) for stars hosting low-mass planets (squares) and high-mass planets (circles).
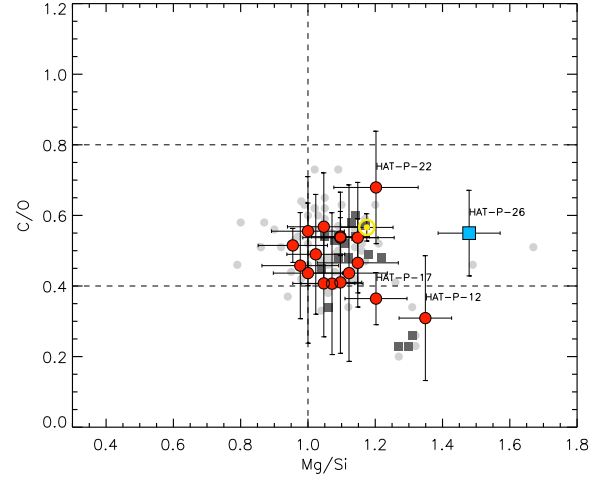

Fig. 14. C/O vs. Mg/Si. The blue square highlights the only star in our sample hosting a planet with mass less than $30\,M_\oplus$. Targets with the highest values of Mg/Si are highlighted. Overplotted in gray are the results by Suárez-Andrés et al. (2018) for stars hosting low-mass planets ($<30\,M_\oplus$; squares) and high-mass planets ($>30\,M_\oplus$; circles). The vertical line represents Mg/Si = 1.0, while horizontal lines are plotted for C/O = 0.4, 0.8, as defined by Suárez-Andrés et al. (2018). Our solar values of $(C/O)_\odot = 0.57$ and $(Mg/Si)_\odot = 1.17$ are also represented with a solar symbol (in yellow).

there could be also a dependence of the planetary structure on the Galactic chemical evolution, as for this target we recognized from chemodynamical diagnostics a possible thin to thick disk transition origin within the Galactic plane (see Sect. 4.3).

A clearer picture can become evident if we also consider volatile elements. While refractory elements (as traced by the abundance ratios Mg/Si[11] and Fe/Si) condense close to the star and their abundance ratios remain constant throughout most of the disk, the same is not true for volatile elements like C/O (see Thiabaud et al. 2015b). Such elemental ratios are important because they govern the distribution and formation of chemical species in the protoplanetary disk, and hence the mineralogy of planets. In Fig. 14 we show how our stars are distributed in a C/O against Mg/Si plot with respect to the sample of planet-hosting stars in Suárez-Andrés et al. (2018). Our stars, for which all C, O, Mg, Si abundances were measured, are mainly concentrated at mean C/O values of 0.48 ± 0.09, with a steep drop-off at super-solar values, and mean Mg/Si values of 1.11 ± 0.13; a similar value is found considering the whole sample for which Mg and Si were derived. These values, together with the wider distribution of Mg/Si when compared with C/O, are indeed consistent with the C/O and Mg/Si ratios found by Brewer et al. (2016) for FGK stars in the solar neighborhood. We also note a tendency for stars cooler than $T_{\rm eff} < 5000\,{\rm K}$ to have mean C/O ratios smaller than those of warmer stars, with a difference of ∼0.08. No clear difference is evident for the Mg/Si ratio.

In regions of high C/O, planets form primarily from carbonates, and in regions of low C/O, the Mg/Si determines the types of silicates that dominate the compositions (e.g., Brewer et al. 2016, and references therein). This means that the C/O ratio controls the distribution of Si among carbide and oxide species. If C/O is greater than 0.8, Si exists in solid form primarily as SiC, and also graphite and TiC will be formed; for C/O ratios below 0.8, Si is present in rock-forming minerals as SiO_4^{4-} or SiO_2, serving as seeds for Mg silicates for which the exact

composition will be controlled by the Mg/Si value (Bond et al. 2010; Thiabaud et al. 2015b). Moreover, Thiabaud et al. (2015a) have shown that the condensation of volatile species as a function of radial distance allows for C/O enrichment in specific parts of the protoplanetary disk of up to four times the solar values, leading to the formation of planets that can be enriched in C/O in their envelope up to three times the solar value. This is the case of HD209458b observed by Giacobbe et al. (2021) for which a scenario of planet formation beyond the water snowline and migration toward its host star through disk or disk-free migration was hypothesized (see also Brewer et al. 2017). At the same time, Mg/Si governs the distribution of silicates: for Mg/Si < 1, Mg forms orthopyroxene ($MgSiO_3$) and the excess Si is present as other silicate species such as feldspars ($CaAl_2Si_2O_8$, $NaAlSiO_8$) or olivine (Mg_2SiO_4); for Mg/Si values ranging from 1 to 2, Mg is distributed between olivine and pyroxene; for Mg/Si > 2, all available Si is consumed to form olivine with excess Mg available to bond with other minerals, mostly oxides such as MgO or MgS (Bond et al. 2010; Thiabaud et al. 2015b). The peak of the Mg/Si-C/O distribution for our targets is therefore consistent with Si which will take solid form as SiO_4^{4-} and SiO_2 and Mg equally distributed between pyroxene and olivine.

Considering the whole sample of 28 targets for which Mg/Si was determined, the star hosting the planet with mass $<30\,M_\oplus$ (HAT-P-26) has the highest Mg/Si value (∼1.5)[12], while 75% of the higher-mass companion host sample show Mg/Si values between 1.0 and 2.0, which means that Mg is equally distributed between pyroxene and olivine. For the 25% of high-mass planet hosts with Mg/Si values below 1.0, Mg and Si will form mainly orthopyroxene, whereas the remaining Si will take other forms, such as feldspars or olivine. No stars with Mg/Si > 2.0 were found. We note here that targets like HAT-P-26 and HAT-P-12, with their high values of Mg/Si, are also among those resulting

---

[11] Hereafter the X_1/X_2 ratio refers to the elemental number ratio: $X_1/X_2 = 10^{\log \epsilon(X_1)}/10^{\log \epsilon(X_2)}$, with $\log \epsilon(X_1)$ and $\log \epsilon(X_2)$ absolute abundances.

[12] HAT-P-26 shows the higher values of Mg/Fe and Mg/Ca that have also been proposed as proxies for low-mass planet composition (see Hinkel & Unterborn 2018).
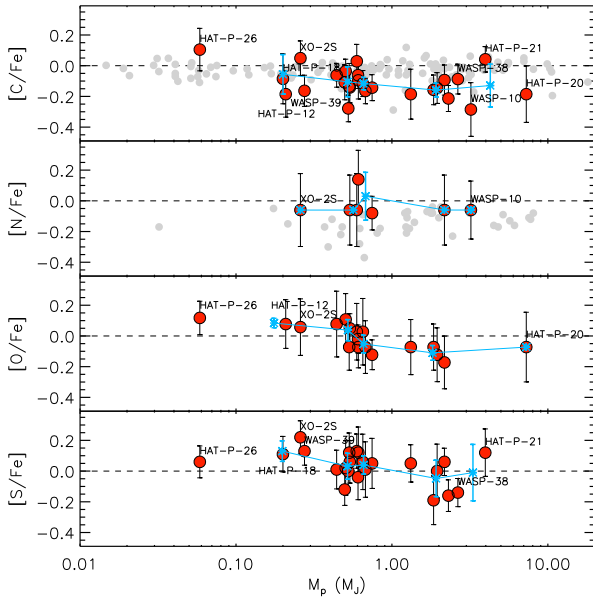
Fig. 15. [C/Fe], [N/Fe], [O/Fe], and [S/Fe] vs. $M_{\rm p}$. Asterisks represent binned values for $M_{\rm p}$ (< 0.4, 0.4–0.6, 0.6–1.2, 1.2–2.4, > 2.4 $M_{\rm Jup}$) and the error bars show the standard deviation for each bin. The targets with $M_{\rm p} < 0.4\,M_{\rm Jup}$ and $M_{\rm p} > 2.4\,M_{\rm Jup}$ are labeled. The gray points for carbon and nitrogen are the values obtained for planet-hosting stars by Suárez-Andrés et al. (2016, 2017), respectively. The dashed lines represent the solar values.

chemically older in our sample. We indeed find a weak trend between Mg/Si and isochronal ages, which could mean that the determination of this chemical ratio could be favored for older (and chromospherically less active) stars (see Sect. 4.4 for the measurement of chemical and isochronal ages). Conclusions of this kind should be confirmed by statistically more significant samples.

If we consider the sample of 18 targets for which both Mg/Si and C/O ratios were measured, 100% of our planet-hosting stars have C/O values lower than 0.8, and 11% of the sample stars have C/O < 0.4. This means that Si will be present in rock-forming minerals as SiO_4^{4-} and SiO_2. In these cases, silicate mineralogy will be controlled by the Mg/Si ratio. Within these 18 targets, 15 high-mass planet hosts show Mg/Si values between 1.0 and 2.0, two targets have Mg/Si < 1.0, and the low-mass planet-hosting star HAT-P-26 shows a value of ~1.5. This supports the finding by Suárez-Andrés et al. (2018), who claimed that low-mass planets are likely to be found in the 1.0–1.5 Mg/Si regime, although mixed with stars with high-mass planets.

We also note here that most targets in our sample show sub-solar values of Mg/Si and C/O ratios. In particular, if we consider the solar values of Mg/Si$_\odot$ = 1.17 ± 0.08, C/O$_\odot$ = 0.57 ± 0.04, we find that 18/28 (i.e., 64%) and 11/18 (i.e., 61%) of our targets show respectively Mg/Si and C/O ratios lower than the solar values at the 1σ level. As already mentioned in Sect. 4.6, this highlights once again how the use of solar values as reference stellar abundances could introduce biases in the interpretation of the planetary compositional models (see Turrini et al. 2021a,b).

4.8. Stellar abundances versus planetary properties

We show in Fig. 15 [X/Fe] versus planetary mass[13] for some volatile elements (i.e., C, N, O, S), with the aim of looking

---

[13] In the cases of multiple planets, such as KELT-6, XO-2S, and HAT-P-17, we considered the planet b, which is the closest planet and that

for possible relations between stellar abundances and planetary properties. The masses of the planets range between 0.058 and 7.27 $M_{\rm Jup}$. In the figure, to better visualize possible trends, we represent with asterisks bins at increasing mass steps (i.e., 0.4, 0.6, 1.2, 2.4 $M_{\rm Jup}$) in order to have similar number of targets per bin. Due to the few targets for which we could measure N abundances, we are not able to draw any conclusion for this element. For the other elements, we see a probable decreasing trend of [C/Fe], [O/Fe], and [S/Fe] with increasing $M_{\rm p}$. For these trends we calculated the Spearman associated statistical significance (ρ), finding $\rho \sim 9 \times 10^{-6}$ for the [O/Fe]–$M_{\rm p}$ relation and $\rho \sim 0.07$ for sulfur and carbon. We note that for the planet XO2-Sb we plot $M_{\rm p} \sin i_{\rm p}$ (instead of $M_{\rm p}$), but we find similar results also when excluding this target, in particular for oxygen. Again, since at least part of these trends could be due to the star hosting the lowest-mass planet, we computed the same statistical significance after excluding HAT-P-26 and we find ρ around 0.18, 6×10^{-5}, and 0.07 for C, O, S, respectively. This means that a more significant correlation is present for the [O/Fe] ratio versus $M_{\rm p}$ with respect to S and C versus $M_{\rm p}$, with an evident decreasing step toward low [O/Fe] values for $M_{\rm p} > 0.5\,M_{\rm Jup}$. A flat tendency was found for C by Suárez-Andrés et al. (2017) and a probable increasing trend was found by Suárez-Andrés et al. (2016) for N. We note that most of the targets hosting low-mass planets and showing higher [O/Fe] are also those resulting chemically old and possibly belonging to the thin–thick disk transition. Moreover, we note that the number of stars in those papers and in this work is not statistically significant, but if our findings are confirmed through bigger samples it could imply that the formation of low-mass planets is favored at the highest values of stellar volatile elements. A possible, yet speculative, interpretation of these trends could be offered by the giant planet formation process in the framework of the pebble accretion scenario. Giant planets of Jovian or super-Jovian mass are expected to form early in the lifetime of circumstellar disks, when the high disk mass accretion rate is capable of supporting the rapid growth of their cores and sustaining their gas accretion rates (see Johansen et al. 2019; Tanaka et al. 2020 for a discussion). As a result, such massive planets can also form in disks comparatively poor in the abundant volatile elements O and C. Less massive planets are expected to form over longer timescales, in circumstellar disks characterized by lower mass accretion rates (Hartmann et al. 1998; Johansen et al. 2019). Such planets may therefore form more easily around volatile-rich stars, so that the higher abundance of ices can partly compensate the lower disk mass accretion rates supporting their growth. In this framework, the stronger trend observed between the planetary mass and the [O/Fe] ratio could be explained by the larger contribution of O to the mass fraction of heavy elements in stars and their disks (in the Sun O provides about 45% of the mass of heavy elements, while C and S only 16 and 2% respectively; Lodders 2010), and its lower volatility compared to C (e.g., Turrini et al. 2021a, and references therein). This means that any increase in the abundance of O would affect wider orbital regions and would have a larger impact on the availability of solid material of planet-forming disks than equal increases in the abundance of C and S, thus resulting more effective in promoting the formation of low-mass planets. On the contrary, the possible trends discussed above cannot be explained as easily in terms of effects linked to the planetary multiplicity, for example by the more massive giant planets blocking the flux of pebbles and promoting the

---

causing the transit (in the cases of KELT-6 and HAT-P-17). We verified that this choice, motivated by homogeneity reasons, does not change our results and conclusions.
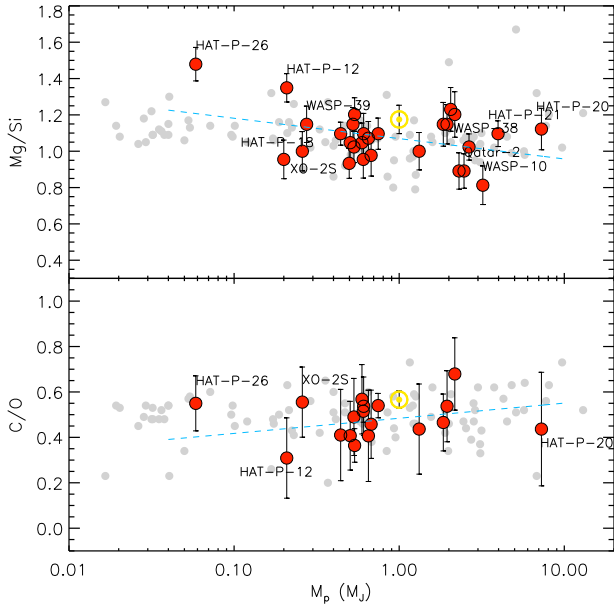
Fig. 16. Mg/Si and C/O elemental abundance ratios as a function of the planetary mass. Correlation fits are shown with dashed lines. The targets with $M_p < 0.4\,M_{Jup}$ and $M_p > 2.4\,M_{Jup}$ are labeled. The position of our solar values is given by the yellow Sun symbol. The gray points are the values of Suárez-Andrés et al. (2018) for planet-hosting stars.

formation of low-mass planets on outer orbits. All giant planets in the sample, with the possible exclusion of HAT-P-26, are significantly more massive than the pebble isolation masses typical of the inner regions of circumstellar disks (Johansen et al. 2019), so they should all be capable of blocking the pebble flux at some point during their migration. Furthermore, due to the lower volatility of S with respect to O (e.g., Turrini et al. 2021a,b and references therein), this process should result in lower values of S/Fe than O/Fe at higher planetary masses, a signature which is not observed in the data. Specifically, the sublimation of the O frozen as ice in the pebbles (e.g., water ice sublimating once the inward-drifting pebbles cross the water snowline) results in a smaller fraction of O being trapped in the pebbles with respect to S and Fe (which remain in solid form until closer to the star), making the trapping process less effective for O than for S and Fe.

We also analyzed Mg/Si and C/O as a function of planetary mass. In Fig. 16 we see a hint of a trend between Mg/Si and M_p (with slope of ~ -0.18 and a Spearman associated statistical significance $\rho \sim 0.3$, which became ~ -0.09 and 0.6 after excluding HAT-P-26) and a still less evident C/O–M_p relation (slope of ~ 0.16 and $\rho \sim 0.5$, which became ~ 0.31 and ~ 0.2 if we do not consider the lowest-mass planet HAT-P-26b). Similar results are obtained after excluding XO-2S for which we know $M_p \sin i_p$ (and not M_p). A possible downward trend of Mg/Si–M_p and a slight increasing trend of C/O–M_p relationships were reported by Mishenina et al. (2021), but no conclusion was drawn because of the large scatter of the ratios at certain planetary mass ranges. Very recently, Tautvaišienė et al. (2022) find a weak negative C/O slope and a slightly more negative Mg/Si slope toward stars with high-mass planets. Here, we note that for icy and giant planets, Mg/Si (and also Fe/Si) in stars should be a direct information about the planetary composition, as no differences are expected between star and planet in terms of Mg/Si, as proposed by Thiabaud et al. (2015a). This is because giant planets are mainly formed outside the ice line, a region where all refractory material

has condensed. Our findings could imply higher values of Mg/Si for lower-mass planets, like HAT-P-26b and HAT-P-12b, which indeed were found to have respectively super-solar and either solar or super-solar metallicity (see Kawashima & Min 2021). We note here that the solar-metallicity star HAT-P-26 and the metal-poor HAT-P-12 are also targets for which we find old chemical ages and the possibility of belonging to the Galactic thin–thick disk transition (see Sects. 4.4, 4.3); therefore, their relatively high Mg/Si ratios could be related to their position in the Galactic disk. Regarding C/O, an indirect relation between the planet and the star should be present. This is mainly because final planetary C/O depends on the location and timescale of formation, how much of the atmosphere is accreted from gas versus solids, and how isolated the atmosphere is from mixing with core materials (see, e.g., Teske et al. 2014 and Giacobbe et al. 2021, and references therein). In Sect. 4.9 we try to give some possible pathways for exoplanets in common with our hosting stars for which C/O and N/O elemental ratios were computed in the literature.

In Fig. 17 we show the distribution of the iron abundance of our stellar sample in terms of the planetary orbit eccentricity, mass, radius, density, and stellar mass. We find a tendency for high-eccentricity planets to be around more metal-rich stars, as also found by Dawson & Murray-Clay (2013) and Mills et al. (2019). Even if we are aware of our not statistically significant sample, we note that the mean [Fe/H], and also the mean values of [α/H] and Mg/Si, are greater by $\sim 0.03-0.05$ dex for planets with $e > 0.1$ when compared with lower-eccentricity planets. This tendency appears not to be influenced by the planetary radii because the planet radii of our sample are within a range $(6-21\,R_E)$ for which no stellar metallicity-planet radius correlation was found (see Buchhave et al. 2014). In order to assign a confidence level of our result, we used a one-side 2×2 Fisher's exact test[14] (Agresti 1992). Choosing the divisions at $e = 0.1$ for high- and low-eccentricity orbits and [Fe/H] = 0.00 dex for metal-poor and metal-rich stars, we find a p-value of 0.29 as the chance that random data would yield this trend, indicating a probability of correlation of 71%. With this in mind, we also find some evidence that our metal-rich stars have wider ranges of planetary masses and denser planets (mean $\rho_P = 1.68\,g\,cm^{-3}$) are around stars with greater [Fe/H] (and therefore in more eccentric orbits) when compared with planets around more metal-poor stars with $e < 0.1$ (mean $\rho_P = 1.11\,g\,cm^{-3}$). We note here that we are cautious about these possible trends both because the number of our targets is relatively small and also because each correlation depends on the interplay of many planetary parameters and stellar properties.

4.9. Can we trace the planet formation scenario?

Turrini et al. (2021a) demonstrated how the joint use of planetary C/N, N/O, and C/O ratios provides useful diagnostics to trace the formation and migration history of giant planets. This result is the direct consequence of the relative volatility of C, O, and N in protoplanetary disks: the bulk of O is trapped in solids already in the inner disk regions; the bulk of N remains in gas form until the outermost regions; C shows an intermediate behavior. The disk gas therefore becomes enriched in N with respect to O and C the farther we move from the star, while solids become increasingly enriched in C and O with respect to N. As a result, the farther from the host star the giant planets start their migration, the more

---

[14] We used the following web calculator (Langsrud et al. 2007): http://www.langsrud.com/fisher.htm

Table 7. Stellar elemental ratios derived in this work (Cols. (2)–(4)), planetary elemental ratios computed by Kawashima & Min (2021) (Cols. (5)–(7)), and planetary-to-stellar elemental ratios defined by Turrini et al. (2021a) (Cols. (8)–(10)).

Name	C/N$_\star$	C/O$_\star$	N/O$_\star$	C/N$_p$	C/O$_p$	N/O$_p$	C/N*	C/O*	N/O*
HAT-P-12	2.09 ± 0.16	0.31 ± 0.18	0.15 ± 0.16	5.33 ± 0.18	0.80 ± 0.15	0.15 ± 0.10	2.55 ± 0.24	2.58 ± 0.23	1.00 ± 0.19
WASP-10	2.00 ± 0.21	0.37 ± 0.18	0.19 ± 0.18	6.31 ± 0.32	0.82 ± 0.30	0.13 ± 0.10	3.16 ± 0.38	2.22 ± 0.35	0.68 ± 0.21
HAT-P-26	3.80 ± 0.15	0.55 ± 0.12	0.14 ± 0.12	1.79 ± 0.16	0.25 ± 0.13	0.14 ± 0.10	0.47 ± 0.22	0.45 ± 0.18	1.00 ± 0.16
WASP-39	3.73 ± 0.12	0.51 ± 0.12	0.14 ± 0.14	1.73 ± 0.16	0.26 ± 0.12	0.15 ± 0.10	0.46 ± 0.20	0.51 ± 0.17	1.07 ± 0.17

Notes. *i.* Planetary C/N were derived by dividing C/O by N/O; *ii.* When we were not able to measure one of the C, N, O stellar abundances, we considered as [X/H] a value consistent with the abundance of elements with the closer T_{cond} (within the volatile elements C, N, and O; see Table 2 and Sect. 4.2).
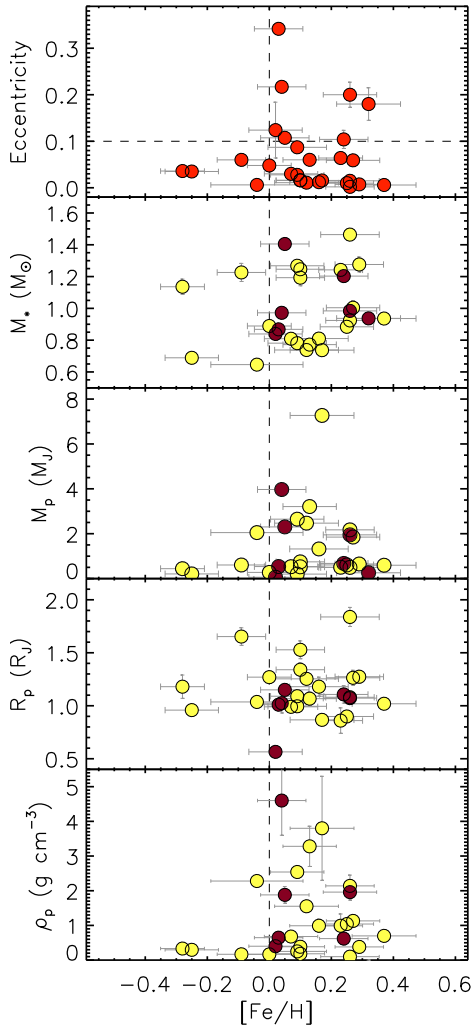

Fig. 17. Orbital eccentricity, stellar mass, planetary mass and radius, and planet density vs. stellar [Fe/H] (from top to bottom). The horizontal line in the first panel is plotted for $e = 0.1$, while the vertical dashed lines indicate [Fe/H] = 0.0. The darker dots in the bottom four panels represent stars with $e > 0.1$. Planet XO-2Sb is shown in the first and third panels, while it is not plotted in the two bottom panels because it is not a transiting planet.

their C/N and N/O ratios will diverge from the stellar values due to the different accretion efficiencies of gas and solids.

The use of planetary elemental ratios normalized to the respective stellar ratios makes it easier to extract the information on the nature of giant planets and constrain whether their metallicity is dominated by the accretion of gas or of solids (see Turrini et al. 2021a,b for additional discussion). Four of the stars analyzed in the present work (HAT-P-26, WASP-10, HAT-P-12, and WASP-39) host planets for which Kawashima & Min (2021) derived metallicity, N/O, and C/O through the spectral disequilibrium retrieval models. Dividing these planetary ratios by those we derived for the hosting stars (which we label X/Y^{*15}), we can therefore gain insights into the formation pathways of these planets.

We list in Table 7 the elemental ratios as defined by Turrini et al. (2021a). Values of C/N* > C/O* > N/O* imply that the budget of heavy elements is dominated by the accretion of solids, while N/O* > C/O* > C/N* implies its accretion is mostly from the disk gas. The authors also claim that in both cases, the separation between the values of the three normalized ratios will increase with the extent of disk-driven migration experienced by the giant planet. Specifically, the farther from the star a giant planet starts its formation, the more significant the difference between its C/N*, C/O*, and N/O*. For our sample of four targets we note that large uncertainties associated with the measurements of the X/Y* ratio cannot allow us to draw a definitive conclusion, and therefore our discussion is mainly qualitative and indicative of possible planetary formation scenarios.

The pattern of the abundance ratios observed for HAT-P-26 and WASP-39 points toward C/N* lower than N/O*, with possible constant and increasing trends between C/N* and C/O*, respectively. Given their C/N* and N/O* abundance patterns, these planets likely underwent migration to get to their present orbits (both at ~0.048 au) and accreted mostly gas along their path (Turrini et al. 2021a). The comparison of the C/N*, C/O*, and N/O* values is consistent with a scenario where both planets started forming outside the CO_2 snowline and accreted most of their gas inward of it (Turrini et al. 2021a), but where the gas was enriched in O by the evaporation of O-rich ices from the inward drifting dust (Booth & Ilee 2019). The two host stars have solar iron abundances, while their planets show super-solar and solar metallicity, respectively for HAT-P-26b and WASP-39b (see MacDonald & Madhusudhan 2019; Kawashima & Min 2021). Since the accretion of non-enriched gas would result in substellar metallicity values (Turrini et al. 2021a,b), the metallicity of these planets appears consistent with the accretion of gas enriched in heavy elements. The estimated abundance patterns tentatively favor the accretion of gas in a disk that underwent chemical reset (Pacetti et al., in prep.).

For the planets orbiting HAT-P-12 and WASP-10 we find C/N* greater than N/O*, with possible constant and decreasing trends between C/N* and C/O*, respectively. The C/N*, C/O*,

---

[15] The X/Y* refers to planetary elemental ratio over stellar elemental ratio: $X/Y^* = \frac{X/Y_P}{X/Y_\star}$.

and N/O* abundance patterns of the planet orbiting WASP-10 are consistent with extensive migration toward its present orbit (at ~0.038 au) and the accretion of heavy elements being dominated by the accretion of solids (Turrini et al. 2021a). The high value of the C/O* ratio is suggestive of an additional contribution to the planetary C budget by the accretion of C-enriched gas, which would favor the accretion of gas between the CO_2 and CH_4 snowlines (Booth & Ilee 2019). The C/N*, C/O*, and N/O* abundance patterns of the planet orbiting HAT-P-12 are also consistent with extensive migration and the accretion of heavy elements being dominated by the accretion of solids. In this case, however, the higher values of the C/O* and N/O* ratios suggest that the planetary budgets of both C and N were affected by the accretion of gas enriched by the evaporation of ices from the inward drifting dust. This would point toward the planet accreting a significant fraction of its gas between the N_2 and CO_2 snowlines (Booth & Ilee 2019). In such a scenario, the planet orbiting HAT-P-12 would have started its formation farther out than its counterpart orbiting WASP-10.

5. Conclusions

In this paper we presented for the first time a wide and comprehensive characterization of a sample of 27 transiting planet host stars within the GAPS programme obtained through a homogeneous and accurate spectroscopic procedure, which is mainly based on high-resolution HARPS-N at TNG spectra (and a few FEROS at ESO spectra). We analyzed this sample for the first time with the aim of deriving different stellar properties, abundances of many elements, and kinematic information. Our main results can be summarized as follows:

- We obtained the atmospheric parameters and the abundances of 26 elements from lithium to europium, together with their kinematic properties. The chemokinematic analysis allowed us to recognize that most of the targets appear to belong to the Galactic thin disk, and a few stars likely belong to a thin–thick disk transition. The lithium line is present in seven stars.
- From the analysis of some elemental ratios, most of them including s-process elements and α-elements, we derived, for the first time in exoplanet hosts, stellar ages often consistent with those obtained through theoretical isochrones.
- From the analysis of the Mg/Si ratios, we find that most of the targets show values consistent with a distribution of Mg between olivine and pyroxene, and a few show Mg forming orthopyroxene. The C/O ratio for all targets is lower than 0.8, compatible with Si present in rock-forming minerals, with a slight tendency of higher values for stars hosting lower-mass planets, even if we note that at least part of this trend could be related to the position of these targets in the Galactic disk.
- We find a tendency for some volatile elements, in particular for the [O/Fe] ratio, to be lower for higher-mass planets. Also in this case, most of the targets hosting low-mass planets and showing high values of [O/Fe] are also those resulting chemodynamically old and possibly belonging to the thin–thick disk transition.
- We find some evidence for high-eccentricity planets to be around more metal-rich stars, and also for denser planets to be around stars with higher [Fe/H].
- From our chemokinematic analysis, the five most interesting targets that can motivate immediate high-precision studies are: *i*. The target hosting the lowest-mass planet in the sample (i.e., HAT-P-26), with solar [Fe/H] and C/O, high [α/Fe],

and the highest values of [Mg/Si] and Mg/Si; it shows UV, TD/D, e_G, and Z_{max} compatible with thin-thick disk transition and seem to have migrating from the Galactic inner disk; *ii*. The relatively metal-poor ([Fe/H] = −0.25) HAT-P-12 and the metal-rich ([Fe/H] ∼ 0.3−0.4) XO-2 binary system show enhancements in [α/Fe]; they have UV and TD/D compatible with thick disk stars, high Galactic eccentricity and large R_{mean} compatible as originating from the inner Galactic disk; *iii*. The solar-metallicity HAT-P-21 shows TD/D and Z_{max} compatible with thin–thick disk transition and seems to originate from the outer Galactic disk.

- Finally, since detailed knowledge of the formation of a planet requires accurate knowledge of chemical abundances of its host star, we tried to discuss the formation and migration mechanisms of those targets for which abundances of planets hosted by stars analyzed in the present work were obtained for the same elemental ratios. We suggest that the planets orbiting HAT-P-26 and WASP-39 started forming outside the CO_2 snowline, while those around HAT-P-12 and WASP-10 probably formed between the CO_2 and CH_4 showlines and between the N_2 and CO_2 showlines, respectively.

We think that analyses like those performed in this work will be necessary for future studies on planetary composition that take into account host star composition, in particular for transiting planet host stars, for which more information about the system formation, migration, and evolution can be retrieved. Metallicity and Mg/Si, C/O, C/N, S/N, N/O ratios are important indicators of planet formation; therefore, future high-precision observations are essential to further explore the trend between stellar and planetary properties toward understanding the formation mechanisms of planets. For instance, some of the planets will be observed by JWST, and therefore this kind of studies are motivated by the prospects of the chemical characterization of exoplanets, and how the chemical compositions of planet host stars relate to those of their planets. Forthcoming JWST observations and other upcoming infrared spectroscopic missions (like ARIEL) will allow us to draw more robust conclusions, in particular regarding the level of precision for planetary abundances, useful to provide definitive conclusions, for example on planetary formation and evolution. Similarly, precise spectroscopic studies together with high-quality photometric data like those acquired with TESS or in the near future with PLATO will be useful to clarify evolutionary stages and to better characterize planetary systems in a global way.

References

Adibekyan, V. Z., Delgado Mena, E., Sousa, S. G., et al. 2012a, A&A, 547, A36

Adibekyan, V. Z., Santos, N. C., Sousa, S. G., et al. 2012b, A&A, 543, A89

Adibekyan, V. Z., Sousa, S. G., Santos, N. C., et al. 2012c, A&A, 545, A32

Adibekyan, V. Z., González Hernández, J. I., Delgado Mena, E., et al. 2014, A&A, 564, L15

Adibekyan, V., Santos, N. C., Figueira, P., et al. 2015, A&A, 581, L2

Agresti, A. 1992, Stat. Sci., 7, 131

Alsubai, K. A., Parley, N. R., Bramich, D. M., et al. 2013, Acta Astron., 63, 465

Amarsi, A. M., Asplund, M., Collet, R., & Leenaarts, J. 2015, MNRAS, 454, L11

Amarsi, A. M., Nissen, P. E., & Skúladóttir, Á. 2019, A&A, 630, A104

Anders, E., & Grevesse, N. 1989, Geochim. Cosmochim. Acta, 53, 197

Asplund, M., Amarsi, A. M., & Grevesse, N. 2021, A&A, 653, A141

Bakos, G., Noyes, R. W., Kovács, G., et al. 2004, PASP, 116, 266

Baraffe, I., Homeier, D., Allard, F., & Chabrier, G. 2015, A&A, 577, A42

Baratella, M., D'Orazi, V., Biazzo, K., et al. 2020, A&A, 640, A123

Barbato, D., Sozzetti, A., Biazzo, K., et al. 2019, A&A, 621, A110

Barklem, P. S., Piskunov, N., & O'Mara, B. J. 2000, A&AS, 142, 467

Bensby, T., Feltzing, S., & Oey, M. S. 2014, A&A, 562, A71

Bergemann, M., & Gehren, T. 2008, A&A, 492, 823

Bergemann, M., Pickering, J. C., & Gehren, T. 2010, MNRAS, 401, 1334

Bertran de Lis, S., Delgado Mena, E., Adibekyan, V. Z., Santos, N. C., & Sousa, S. G. 2015, A&A, 576, A89

Biazzo, K., D'Orazi, V., Desidera, S., et al. 2012, MNRAS, 427, 2905

Biazzo, K., Gratton, R., Desidera, S., et al. 2015, A&A, 583, A135

Boesgaard, A. M., Deliyannis, C. P., Stephens, A., & King, J. R. 1998, ApJ, 493, 206

Bond, J. C., O'Brien, D. P., & Lauretta, D. S. 2010, ApJ, 715, 1050

Bonomo, A. S., Desidera, S., Benatti, S., et al. 2017, A&A, 602, A107

Booth, R. A., & Ilee, J. D. 2019, MNRAS, 487, 3998

Borsa, F., Fossati, L., Koskinen, T., Young, M. E., & Shulyak, D. 2021, Nat. Astron., 6, 226

Bouvier, J. 2008, A&A, 489, L53

Bovy, J. 2015, ApJS, 216, 29

Bovy, J., Allende Prieto, C., Beers, T. C., et al. 2012, ApJ, 759, 131

Bressan, A., Marigo, P., Girardi, L., et al. 2012, MNRAS, 427, 127

Brewer, J. M., Fischer, D. A., Valenti, J. A., & Piskunov, N. 2016, ApJS, 225, 32

Brewer, J. M., Fischer, D. A., & Madhusudhan, N. 2017, AJ, 153, 83

Brucalassi, A., Tsantaki, M., Magrini, L., et al. 2021, Exp. Astron., 53, 511

Buchhave, L. A., Bizzarro, M., Latham, D. W., et al. 2014, Nature, 509, 593

Burke, C. J., McCullough, P. R., Valenti, J. A., et al. 2007, ApJ, 671, 2115

Caffau, E., Ludwig, H. G., Steffen, M., et al. 2008, A&A, 488, 1031

Caffau, E., Maiorca, E., Bonifacio, P., et al. 2009, A&A, 498, 877

Capitanio, L., Lallement, R., Vergely, J. L., Elyajouri, M., & Monreal-Ibero, A. 2017, A&A, 606, A65

Casali, G., Spina, L., Magrini, L., et al. 2020, A&A, 639, A127

Castelli, F., & Kurucz, R. L. 2003, IAU Symp., 210, A20

Chaplin, W. J., Sanchis-Ojeda, R., Campante, T. L., et al. 2013, ApJ, 766, 101

Charbonneau, D., Brown, T. M., Noyes, R. W., & Gilliland, R. L. 2002, ApJ, 568, 377

Claret, A. 2019, Res. Notes Am. Astron. Soc., 3, 17

Cosentino, R., Lovis, C., Pepe, F., et al. 2012, SPIE Conf. Ser., 8446, 84461V

Coşkunoğlu, B., Ak, S., Bilir, S., et al. 2011, MNRAS, 412, 1237

Costa Silva, A. R., Delgado Mena, E., & Tsantaki, M. 2020, A&A, 634, A136

Covino, E., Esposito, M., Barbieri, M., et al. 2013, A&A, 554, A28

Cummings, J. D., Deliyannis, C. P., Maderak, R. M., & Steinhauer, A. 2017, AJ, 153, 128

Cuntz, M., Saar, S. H., & Musielak, Z. E. 2000, ApJ, 533, L151

da Silva, L., Girardi, L., Pasquini, L., et al. 2006, A&A, 458, 609

Damasso, M., Biazzo, K., Bonomo, A. S., et al. 2015a, A&A, 575, A111

Damasso, M., Esposito, M., Nascimbeni, V., et al. 2015b, A&A, 581, L6

Danielski, C., Brucalassi, A., Benatti, S., et al. 2021, Exp. Astron., 53, 473

Dawson, R. I., & Murray-Clay, R. A. 2013, ApJ, 767, L24

Delgado Mena, E., Israelian, G., González Hernández, J. I., et al. 2014, A&A, 562, A92

Delgado Mena, E., Bertrán de Lis, S., Adibekyan, V. Z., et al. 2015, A&A, 576, A69

Delgado Mena, E., Adibekyan, V. Z., Figueira, P., et al. 2018, PASP, 130, 094202

Delgado Mena, E., Adibekyan, V., Santos, N. C., et al. 2021, A&A, 655, A99

Den Hartog, E. A., Lawler, J. E., Sneden, C., & Cowan, J. J. 2003, ApJS, 148, 543

Desidera, S., Bonomo, A. S., Claudi, R. U., et al. 2014, A&A, 567, L6

di Mauro, M. P., Cardini, D., Catanzaro, G., et al. 2011, MNRAS, 415, 3783

Doyle, A. P., Davies, G. R., Smalley, B., Chaplin, W. J., & Elsworth, Y. 2014, MNRAS, 444, 3592

Eggen, O. J. 1996, AJ, 111, 1615

Enoch, B., Anderson, D. R., Barros, S. C. C., et al. 2011, AJ, 142, 86

Esposito, M., Covino, E., Mancini, L., et al. 2014, A&A, 564, L13

Esposito, M., Covino, E., Desidera, S., et al. 2017, A&A, 601, A53

Gagné, J., Lafrenière, D., Doyon, R., Malo, L., & Artigau, É. 2014, ApJ, 783, 121

Gagné, J., Mamajek, E. E., Malo, L., et al. 2018, ApJ, 856, 23

Gaia Collaboration (Prusti, T., et al.) 2016, A&A, 595, A1

Gaia Collaboration (Brown, A. G. A., et al.) 2021, A&A, 649, A1

Gallagher, A. J., Ryan, S. G., García Pérez, A. E., & Aoki, W. 2010, A&A, 523, A24

Ghezzi, L., Cunha, K., Smith, V. V., et al. 2009, ApJ, 698, 451

Ghezzi, L., Cunha, K., Smith, V. V., et al. 2010, ApJ, 720, 1290

Giacobbe, P., Brogi, M., Gandhi, S., et al. 2021, Nature, 592, 205

Gonzalez, G. 2009, MNRAS, 399, L103

González Hernández, J. I., Delgado-Mena, E., Sousa, S. G., et al. 2013, A&A, 552, A6

Gratton, R. G., Bonanno, G., Claudi, R. U., et al. 2001, A&A, 377, 123

Guillot, T., Santos, N. C., Pont, F., et al. 2006, A&A, 453, L21

Hartmann, L., Calvet, N., Gullbring, E., & D'Alessio, P. 1998, ApJ, 495, 385

Harutyunyan, G., Steffen, M., Mott, A., et al. 2018, A&A, 618, A16

Hinkel, N. R., & Unterborn, C. T. 2018, ApJ, 853, 83

Israelian, G., Santos, N. C., Mayor, M., & Rebolo, R. 2001, Nature, 411, 163

Johansen, A., Ida, S., & Brasser, R. 2019, A&A, 622, A202

Johansson, S., Litzén, U., Lundberg, H., & Zhang, Z. 2003, ApJ, 584, L107

Johnson, D. R. H., & Soderblom, D. R. 1987, AJ, 93, 864

Johnson, J. A., Ivans, I. I., & Stetson, P. B. 2006, ApJ, 640, 801

Jorge, D. M., Kamp, I. E. E., Waters, L. B. F. M., Woitke, P., & Spaargaren, R. J. 2022, A&A, 660, A85

Jurić, M., Ivezić, Ž., Brooks, A., et al. 2008, ApJ, 673, 864

Kane, S. R., Collier Cameron, A., Horne, K., et al. 2004, MNRAS, 353, 689

Kaufer, A., Stahl, O., Tubbesing, S., et al. 1999, The Messenger, 95, 8

Kawashima, Y., & Min, M. 2021, A&A, 656, A90

Kolecki, J. R., & Wang, J. 2021, AAS, submitted [arXiv:2112.02031]

Kramida, A. 2019, APS Meeting Abs., 2019, N09.004

Kupka, F. G., Ryabchikova, T. A., Piskunov, N. E., Stempels, H. C., & Weiss, W. W. 2000, Balt. Astron., 9, 590

Kurucz, R. L. 1993, Phys. Scr. T, 47, 110

Lang, K. R. 1974, Astrophysical Formulae: a Compendium for the Physicist and Astrophysicist (Berlin: Springer)

Langsrud, O., Jørgensen, K., Ofstad, R., & Næs, T. 2007, J. Appl. Stat., 34, 1275

Lawler, J. E., Bonvallet, G., & Sneden, C. 2001a, ApJ, 556, 452

Lawler, J. E., Wickliffe, M. E., den Hartog, E. A., & Sneden, C. 2001b, ApJ, 563, 1075

Lind, K., Asplund, M., & Barklem, P. S. 2009, A&A, 503, 541

Lind, K., Asplund, M., Barklem, P. S., & Belyaev, A. K. 2011, A&A, 528, A103

Liu, F., Asplund, M., Ramirez, I., Yong, D., & Melendez, J. 2014, MNRAS, 442, L51

Liu, F., Yong, D., Asplund, M., et al. 2020, MNRAS, 495, 3961

Ljung, G., Nilsson, H., Asplund, M., & Johansson, S. 2006, A&A, 456, 1181

Lodders, K. 2003, ApJ, 591, 1220

Lodders, K. 2010, Astrophys. Space Sci. Proc., 16, 379

López-Valdivia, R., Hernández-Águila, J. B., Bertone, E., et al. 2015, MNRAS, 451, 4368

MacDonald, R. J., & Madhusudhan, N. 2019, MNRAS, 486, 1292

Madhusudhan, N. 2019, ARA&A, 57, 617

Madhusudhan, N., Amin, M. A., & Kennedy, G. M. 2014, ApJ, 794, L12

Magrini, L., Danielski, C., Bossini, D., et al. 2022, A&A, 663, A161

Maia, M. T., Meléndez, J., Lorenzo-Oliveira, D., Spina, L., & Jofré, P. 2019, A&A, 628, A126

Maldonado, J., Villaver, E., & Eiroa, C. 2018, A&A, 612, A93

Maldonado, J., Villaver, E., Eiroa, C., & Micela, G. 2019, A&A, 624, A94

Mancini, L., Esposito, M., Covino, E., et al. 2015, A&A, 579, A136

Mancini, L., Esposito, M., Covino, E., et al. 2018, A&A, 613, A41

Mancini, L., Esposito, M., Covino, E., et al. 2022, A&A, 664, A162

Masseron, T., Plez, B., Van Eck, S., et al. 2014, A&A, 571, A47

McCullough, P. R., Stys, J. E., Valenti, J. A., et al. 2005, PASP, 117, 783

Meléndez, J., Asplund, M., Gustafsson, B., & Yong, D. 2009, ApJ, 704, L66

Meléndez, J., Bergemann, M., Cohen, J. G., et al. 2012, A&A, 543, A29

Meléndez, J., Ramírez, I., Karakas, A. I., et al. 2014, ApJ, 791, 14

Mills, S. M., Howard, A. W., Petigura, E. A., et al. 2019, AJ, 157, 198

Mishenina, T., Kovtyukh, V., Soubiran, C., & Adibekyan, V. Z. 2016, MNRAS, 462, 1563

Mishenina, T., Basak, N., Adibekyan, V., Soubiran, C., & Kovtyukh, V. 2021, MNRAS, 504, 4252

Mortier, A., Santos, N. C., Sousa, S. G., et al. 2013, A&A, 558, A106
Mott, A., Steffen, M., Caffau, E., Spada, F., & Strassmeier, K. G. 2017, A&A, 604, A44
Nissen, P. E. 2015, A&A, 579, A52
Öberg, K. I., Murray-Clay, R., & Bergin, E. A. 2011, ApJ, 743, L16
O'Donovan, F. T. 2007, PASP, 119, 1207
Pasquini, L., Biazzo, K., Bonifacio, P., Randich, S., & Bedin, L. R. 2008, A&A, 489, 677
Pavlenko, Y. V., Jenkins, J. S., Ivanyuk, O. M., et al. 2018, A&A, 611, A27
Pepper, J., Pogge, R. W., DePoy, D. L., et al. 2007, PASP, 119, 923
Prochaska, J. X., Naumov, S. O., Carney, B. W., McWilliam, A., & Wolfe, A. M. 2000, AJ, 120, 2513
Ramírez, I., Meléndez, J., Cornejo, D., Roederer, I. U., & Fish, J. R. 2011, ApJ, 740, 76
Ramírez, I., Fish, J. R., Lambert, D. L., & Allende Prieto, C. 2012, ApJ, 756, 46
Reddy, B. E., Lambert, D. L., Laws, C., Gonzalez, G., & Covey, K. 2002, MNRAS, 335, 1005
Robinson, S. E., Laughlin, G., Bodenheimer, P., & Fischer, D. 2006, ApJ, 643, 484
Santos, N. C., Israelian, G., & Mayor, M. 2004, A&A, 415, 1153
Santos, N. C., Sousa, S. G., Mortier, A., et al. 2013, A&A, 556, A150
Schuler, S. C., Flateau, D., Cunha, K., et al. 2011, ApJ, 732, 55
Scott, P., Grevesse, N., Asplund, M., et al. 2015, A&A, 573, A25
Sestito, P., & Randich, S. 2005, A&A, 442, 615
Smith, V. V., Cunha, K., & Lazzaro, D. 2001, AJ, 121, 3207
Sneden, C. 1973, ApJ, 184, 839
Sneden, C., Lucatello, S., Ram, R. S., Brooke, J. S. A., & Bernath, P. 2014, ApJS, 214, 26
Sousa, S. G., Santos, N. C., Mayor, M., et al. 2008, A&A, 487, 373
Sousa, S. G., Santos, N. C., Mortier, A., et al. 2015, A&A, 576, A94
Sousa, S. G., Adibekyan, V., Delgado-Mena, E., et al. 2021, A&A, 656, A53
Sozzetti, A., Yong, D., Carney, B. W., et al. 2006, AJ, 131, 2274
Sozzetti, A., Bonomo, A. S., Biazzo, K., et al. 2015, A&A, 575, L15
Spina, L., Meléndez, J., Karakas, A. I., et al. 2016a, A&A, 593, A125
Spina, L., Meléndez, J., & Ramírez, I. 2016b, A&A, 585, A152
Suárez-Andrés, L., Israelian, G., González Hernández, J. I., et al. 2016, A&A, 591, A69
Suárez-Andrés, L., Israelian, G., González Hernández, J. I., et al. 2017, A&A, 599, A96
Suárez-Andrés, L., Israelian, G., González Hernández, J. I., et al. 2018, A&A, 614, A84
Swastik, C., Banyal, R. K., Narang, M., et al. 2021, AJ, 161, 114
Talon, S., & Charbonnel, C. 2005, A&A, 440, 981
Tanaka, H., Murase, K., & Tanigawa, T. 2020, ApJ, 891, 143
Tautvaišienė, G., Mikolaitis, Š., Drazdauskas, A., et al. 2022, ApJS, 259, 45
Teske, J. K., Cunha, K., Smith, V. V., Schuler, S. C., & Griffith, C. A. 2014, ApJ, 788, 39
Teske, J. K., Ghezzi, L., Cunha, K., et al. 2015, ApJ, 801, L10
Teske, J. K., Thorngren, D., Fortney, J. J., Hinkel, N., & Brewer, J. M. 2019, AJ, 158, 239
Thiabaud, A., Marboeuf, U., Alibert, Y., Leya, I., & Mezger, K. 2015a, A&A, 580, A30
Thiabaud, A., Marboeuf, U., Alibert, Y., Leya, I., & Mezger, K. 2015b, A&A, 574, A138
Tinetti, G., Eccleston, P., Haswell, C., et al. 2021, ArXiv e-prints [arXiv:2104.04824]
Torres, G., Fischer, D. A., Sozzetti, A., et al. 2012, ApJ, 757, 161
Turrini, D., Schisano, E., Fonte, S., et al. 2021a, ApJ, 909, 40
Turrini, D., Codella, C., Danielski, C., et al. 2021b, Exp. Astron., 53, 225
Valenti, J. A., & Fischer, D. A. 2005, ApJS, 159, 141
Voelkel, O., Klahr, H., Mordasini, C., & Emsenhuber, A. 2022, A&A in press, https://doi.org/10.1051/0004-6361/202141830
Yong, D., Meléndez, J., Grundahl, F., et al. 2013, MNRAS, 434, 3542

[1] INAF – Osservatorio Astronomico di Roma, Via Frascati 33, 00040 Monte Porzio Catone (RM), Italy,
e-mail: `katia.biazzo@inaf.it`
[2] INAF – Osservatorio Astronomico di Padova, Vicolo dell'Osservatorio 5, 35122 Padova, Italy
[3] INAF – Osservatorio Astrofisico di Torino, Via Osservatorio 20, 10025 Pino Torinese, Italy
[4] INAF – Osservatorio Astronomico di Palermo, Piazza del Parlamento 1, 90134 Palermo, Italy
[5] INAF – Osservatorio Astrofisico di Arcetri, Largo E. Fermi 5, I-50125 Firenze, Italy
[6] Leibniz-Institut für Astrophysik Potsdam, An der Sternwarte 16, 14482 Potsdam, Germany
[7] INAF – Osservatorio Astronomico di Brera, Via E. Bianchi 46, 23807 Merate (LC), Italy
[8] INAF – Osservatorio Astronomico di Capodimonte, Salita Moiariello 16, 80131 Napoli, Italy
[9] INAF – Istituto di Astrofisica e Planetologia Spaziali, Via del Fosso del Cavaliere 100, 00133 Roma, Italy
[10] INAF – Osservatorio Astrofisico di Catania, Via S. Sofia 78, 95123 Catania, Italy
[11] Dipartimento di Fisica e Astronomia, Università di Padova, Vicolo dell'Osservatorio 2, 35122 Padova, Italy
[12] Fundación Galileo Galilei – INAF, Rambla José Ana Fernandez Pérez 7, 38712 Breña Baja (TF), Spain
[13] INAF – Istituto di Radioastronomia, Via Gobetti 101, 40127 Bologna, Italy
[14] INAF – Osservatorio Astronomico di Trieste, Via Tiepolo 11, 34143 Trieste, Italy
[15] Astronomy Department, 96 Foss Hill Dr, Van Vleck Observatory, Wesleyan University, Middletown, CT-06459, US
[16] Dipartimento di Fisica, Università di Roma Tor Vergata, Via della Ricerca Scientifica 1, 00133 Roma, Italy
[17] INAF – Osservatorio di Cagliari, Via della Scienza 5, 09047 Selargius (CA), Italy

Appendix A: Additional tables

Table A.1. Basic information and parameters of our targets taken from the literature and used in this work. Right ascensions, declinations, Gaia EDR3 magnitudes and colors, proper motions, and parallaxes were taken from Gaia Collaboration (2021); spectral types were retrieved from the NASA Exoplanet Archive and SIMBAD; Galactic latitudes and longitudes from SIMBAD; planetary masses and eccentricities from Bonomo et al. (2017) and the NASA Exoplanet Archive; and the Mittag chromospheric indicators log R'_{HK} from Claudi et al. (in prep.).

Name	α (deg)	δ (deg)	Sp.T.	G (mag)	G_{BP} (mag)	R_{BP} (mag)	μ_α (mas/yr)	μ_δ (mas/yr)	π (mas)	l_{gal} (deg)	b_{gal} (deg)	M_p (M_{Jup})	e	$\log R'_{HK}$
HAT-P-3	206.094	+48.028	K1	11.279	11.740	10.662	-19.62 ± 0.01	-23.973 ± 0.02	7.42 ± 0.01	100.167	+66.693	0.609	0.010	-4.652
HAT-P-4	229.991	+36.229	G1	11.063	11.370	10.596	-21.51 ± 0.01	-24.255 ± 0.02	3.11 ± 0.02	58.480	+57.336	0.651	0.007	-4.868
HAT-P-14	260.116	+38.242	F5	9.878	10.106	9.492	$+2.35\pm0.01$	-6.679 ± 0.01	4.45 ± 0.01	62.589	+33.538	2.303	0.107	-4.802
HAT-P-12	209.389	+43.493	K4	12.408	12.992	11.683	$+134.79\pm0.01$	-44.229 ± 0.01	7.04 ± 0.01	87.993	+68.876	0.208	0.035	-4.481
HAT-P-15	66.248	+39.460	G5	11.716	12.252	11.024	$+14.23\pm0.02$	-9.407 ± 0.02	5.19 ± 0.02	161.559	-6.892	1.949	0.200	-4.793
HAT-P-17	324.536	+30.488	K0	10.279	10.695	9.694	-80.28 ± 0.02	-127.037 ± 0.02	10.82 ± 0.02	80.851	-16.177	0.537	0.342	-4.870
HAT-P-18	256.346	+33.012	K2	12.358	12.906	11.666	-14.00 ± 0.01	-36.751 ± 0.01	6.19 ± 0.01	55.652	+35.562	0.200	0.087	-4.477
HAT-P-20	111.916	+24.336	K3	10.991	11.641	10.223	-5.10 ± 0.02	-96.090 ± 0.02	14.01 ± 0.02	194.415	+18.394	7.270	0.016	-4.022
HAT-P-21	171.275	+41.028	G3	11.557	11.902	11.050	-1.14 ± 0.02	$+13.523\pm0.02$	3.52 ± 0.02	169.325	+67.464	3.970	0.217	-4.299
HAT-P-22	155.681	+50.128	G5	9.525	9.932	8.952	-26.11 ± 0.01	$+83.806\pm0.02$	12.27 ± 0.02	163.647	+53.566	2.172	0.002	-4.878
HAT-P-26	213.157	+04.059	K1	11.462	11.919	10.840	$+37.74\pm0.03$	-142.816 ± 0.02	7.00 ± 0.02	346.513	+59.873	0.059	0.124	-4.847
HAT-P-29	33.131	+51.778	F8	11.728	12.073	11.215	-9.97 ± 0.02	$+1.790\pm0.02$	3.14 ± 0.02	135.471	-9.108	0.676	0.104	-4.841
HAT-P-30	123.950	+05.836	G0	10.304	10.561	9.89	-17.23 ± 0.01	$+23.875\pm0.01$	4.80 ± 0.02	217.412	+21.405	0.746	0.016	-5.043
HAT-P-36	188.266	+44.915	G5	12.085	12.440	11.569	-11.62 ± 0.01	$+8.138\pm0.01$	3.41 ± 0.01	133.414	+71.837	1.850	0.059	-4.431
KELT-6	195.982	+30.640	F8	10.198	10.442	9.791	-4.96 ± 0.01	$+15.722\pm0.01$	4.11 ± 0.02	85.775	+85.550	0.442	0.036	-4.907
Qatar-1	303.382	+65.162	K2	12.465	13.004	11.780	$+12.78\pm0.01$	$+58.064\pm0.01$	5.34 ± 0.01	98.719	+16.424	1.321	0.012	-4.191
Qatar-2	207.655	-06.804	K5	13.015	13.662	12.245	-88.17 ± 0.02	-15.187 ± 0.02	5.48 ± 0.02	327.956	+53.168	2.470	0.011	-4.225
TRES-4	268.304	+37.211	F8	11.470	11.725	11.050	-6.38 ± 0.02	-20.891 ± 0.02	1.97 ± 0.01	63.039	+26.994	0.498	0.015	-5.106
WASP-10	348.993	+31.462	K5	12.164	12.736	11.452	$+25.05\pm0.01$	-25.366 ± 0.01	7.07 ± 0.01	100.112	-27.144	3.210	0.060	-4.943
WASP-11	47.369	+30.673	K3	11.559	12.072	10.873	$+3.33\pm0.07$	-44.433 ± 0.05	7.70 ± 0.06	155.018	-23.463	0.532	0.030	-4.859
WASP-13	140.103	+33.882	G1	10.383	10.675	9.924	-2.28 ± 0.02	-20.072 ± 0.02	4.33 ± 0.02	190.929	+44.536	0.525	0.016	-4.937
WASP-38	243.960	+10.032	F8	9.218	9.485	8.78	-31.14 ± 0.02	-39.167 ± 0.01	7.34 ± 0.02	23.528	+39.033	2.648	0.028	-4.890
WASP-39	217.327	-03.444	G8	11.881	12.280	11.316	-19.04 ± 0.02	$+0.437\pm0.01$	4.64 ± 0.01	344.403	+51.371	0.275	0.048	-4.801
WASP-43	154.908	-09.806	K7	11.894	12.660	11.040	-41.99 ± 0.02	-38.004 ± 0.02	11.47 ± 0.02	252.787	+37.870	2.050	0.006	-4.030
WASP-54	205.454	-00.128	F9	10.248	10.518	9.815	-10.81 ± 0.02	-24.744 ± 0.02	3.99 ± 0.02	328.936	+60.175	0.606	0.060	-4.949
WASP-60	356.667	+31.155	G1	12.010	12.358	11.498	$+30.25\pm0.02$	-6.005 ± 0.01	2.32 ± 0.02	106.985	-29.702	0.505	0.064	-4.881
XO-2N	117.027	+50.225	G9	10.971	11.390	10.392	-29.55 ± 0.02	-154.227 ± 0.01	6.66 ± 0.02	168.290	+29.328	0.595	0.006	-4.709
XO-2S	117.031	+50.216	G9	10.927	11.331	10.362	-29.31 ± 0.02	-154.233 ± 0.01	6.67 ± 0.02	168.300	+29.330	0.259*	0.180	...

Note: * This is the value of $M_p \sin i_p$.

Table A.2. Final elemental abundances derived in this work. Shown in parentheses are the number of lines and the cases for which we applied the spectral synthesis (s).

Name	[C/H] (dex)	[N/H] (dex)	[O/H] (dex)	[Na/H] (dex)	[Mg/H] (dex)	[Al/H] (dex)	[Si/H] (dex)	[S/H] (dex)	[Ca/H] (dex)	[Sc/H] (dex)	[Ti i/H] (dex)	[Ti ii/H] (dex)	[V/H] (dex)
							Elements with Z ≤ 23						
HAT-P-3	0.15±0.09(3,s)	0.39±0.17(s)	0.18±0.10(s)	0.50±0.01(2)	0.27±0.12(3)	0.40±0.06(1)	0.30±0.07(12)	0.37±0.14(3)	0.33±0.12(9)	0.33±0.07(3)	0.40±0.10(17)	0.40±0.09(5)	0.48±0.09(12)
HAT-P-4	0.17±0.03(3,s)	...	0.32±0.20(s)	0.16±0.06(4)	0.23±0.09(4)	0.23±0.07(3)	0.27±0.08(12)	0.35±0.16(3)	0.27±0.08(12)	0.34±0.13(3)	0.27±0.06(19)	0.29±0.09(6)	0.24±0.06(11)
HAT-P-12	-0.44±0.12(s)	...	-0.17±0.13(s)	-0.25±0.05(2)	-0.18±0.08(3)	-0.01±0.07(2)	-0.18±0.08(12)	...	-0.18±0.13(7)	-0.13±0.10(3)	-0.08±0.11(16)	-0.15±0.05(2)	0.01±0.07(11)
HAT-P-14	-0.16±0.03(3,s)	...	...	-0.08±0.05(4)	-0.10±0.10(4)	-0.03±0.06(2)	0.02±0.08(11)	-0.11±0.07(3)	0.16±0.09(13)	-0.02±0.07(3)	0.04±0.08(16)	0.06±0.11(7)	0.15±0.06(3)
HAT-P-15	0.11±0.05(3,s)	...	0.14±0.15(s)	0.34±0.04(2)	0.27±0.11(4)	0.28±0.07(3)	0.28±0.08(12)	0.26±0.15(3)	0.24±0.09(11)	0.31±0.13(2)	0.29±0.07(20)	0.40±0.05(4)	0.23±0.08(12)
HAT-P-17	-0.11±0.06(3,s)	-0.03±0.21(s)	0.08±0.05(3,s)	0.03±0.01(2)	0.07±0.08(4)	0.07±0.07(2)	0.06±0.09(12)	0.09±0.11(3)	0.03±0.11(10)	0.09±0.13(2)	0.08±0.09(21)	0.10±0.08(6)	0.09±0.06(12)
HAT-P-18	0.00±0.13(s)	...	...	0.17±0.05(2)	0.03±0.09(3)	0.17±0.06(1)	0.12±0.09(12)	0.20±0.07(1)	0.15±0.11(8)	0.11±0.06(3)	0.20±0.08(12)	0.16±0.11(3)	0.23±0.10(12)
HAT-P-20	-0.02±0.15(s)	...	0.10±0.20(s)	...	0.09±0.09(3)	0.27±0.09(2)	0.11±0.10(9)	...	0.26±0.15(3)	0.31±0.17(3)	0.29±0.12(13)	0.17±0.11(3)	0.49±0.12(11)
HAT-P-21	0.08±0.03(3,s)	...	...	-0.01±0.08(4)	0.07±0.08(4)	0.08±0.09(3)	0.10±0.07(11)	0.16±0.13(3)	0.06±0.08(13)	0.12±0.11(3)	0.11±0.06(20)	0.13±0.09(5)	0.04±0.06(12)
HAT-P-22	0.17±0.06(3,s)	0.20±0.21(s)	0.09±0.15(s)	0.33±0.01(2)	0.40±0.13(3)	0.41±0.08(3)	0.39±0.08(12)	0.32±0.04(3)	0.33±0.11(9)	0.41±0.17(3)	0.42±0.10(21)	0.47±0.08(5)	0.37±0.06(12)
HAT-P-26	0.12±0.11(2,s)	...	0.14±0.07(3)	0.04±0.04(2)	0.18±0.09(3)	0.25±0.08(2)	0.08±0.08(12)	0.08±0.06(3)	0.07±0.12(9)	0.07±0.12(3)	0.17±0.11(21)	0.20±0.07(4)	0.20±0.07(12)
HAT-P-29	0.08±0.03(2,s)	...	0.17±0.15(s)	0.13±0.03(4)	0.13±0.11(4)	0.11±0.10(3)	0.21±0.09(11)	0.25±0.16(3)	0.24±0.08(13)	0.18±0.10(3)	0.17±0.06(20)	0.20±0.08(5)	0.16±0.09(9)
HAT-P-30	-0.04±0.03(2,s)	0.02±0.08(2)	-0.02±0.06(3)	-0.01±0.06(4)	0.01±0.09(4)	-0.10±0.08(2)	0.04±0.07(11)	0.15±0.14(3)	0.09±0.11(14)	0.03±0.08(3)	0.04±0.06(19)	0.05±0.11(6)	0.04±0.08(7)
HAT-P-36	0.11±0.04(3,s)	...	...	0.29±0.03(2)	0.25±0.11(4)	0.31±0.07(3)	0.26±0.09(11)	0.08±0.13(2)	0.27±0.10(12)	0.22±0.17(3)	0.26±0.06(19)	0.39±0.07(5)	0.17±0.08(12)
KELT-6	-0.34±0.03(2,s)	...	-0.20±0.20(s)	-0.31±0.04(2)	-0.25±0.06(2)	-0.22±0.08(3)	-0.22±0.08(12)	-0.27±0.10(3)	-0.17±0.07(13)	-0.29±0.08(3)	-0.23±0.06(21)	-0.23±0.06(6)	-0.21±0.06(9)
Qatar-1	-0.03±0.13(s)	...	0.09±0.15(s)	0.33±0.03(2)	0.15±0.08(3)	0.32±0.06(2)	0.22±0.10(12)	0.21±0.08(1)	0.18±0.11(7)	0.34±0.13(3)	0.26±0.10(16)	0.27±0.07(2)	0.35±0.09(12)
Qatar-2	...	...	...	0.32±0.05(2)	0.05±0.11(3)	0.26±0.10(3)	0.17±0.06(5)	...	0.23±0.14(3)	0.31±0.09(2)	0.26±0.14(13)	0.15±0.09(3)	0.46±0.12(11)
TRES-4	0.15±0.06(3,s)	...	...	0.21±0.08(4)	0.13±0.06(3)	0.26±0.12(2)	0.23±0.09(11)	0.14±0.04(2)	0.26±0.08(11)	0.26±0.13(2)	0.19±0.08(15)	0.26±0.08(7)	0.19±0.07(6)
WASP-10	-0.16±0.15(s)	...	...	0.08±0.09(2)	-0.04±0.09(3)	0.14±0.07(2)	0.12±0.09(9)	...	0.10±0.14(6)	0.15±0.14(3)	0.14±0.13(18)	0.09±0.13(2)	0.19±0.09(12)
WASP-11	-0.07±0.12(s)	0.07±0.17(s)	-0.00±0.12(s)	0.22±0.03(2)	0.11±0.09(3)	0.16±0.08(2)	0.17±0.07(10)	0.19±0.09(3)	0.07±0.11(8)	0.17±0.16(3)	0.08±0.10(17)	0.10±0.11(4)	0.16±0.08(12)
WASP-13	-0.18±0.04(3,s)	...	...	0.04±0.02(4)	0.08±0.08(4)	0.09±0.09(3)	0.09±0.09(12)	0.10±0.08(3)	0.14±0.08(12)	0.06±0.06(3)	0.08±0.06(19)	0.08±0.14(7)	0.07±0.06(11)
WASP-38	0.00±0.05(3,s)	...	...	0.00±0.03(4)	-0.02±0.07(2)	-0.06±0.08(2)	-0.06±0.08(11)	-0.05±0.03(2)	0.10±0.10(11)	0.00±0.10(3)	0.04±0.07(19)	0.07±0.07(6)	0.11±0.07(9)
WASP-39	-0.16±0.07(3,s)	...	...	-0.06±0.08(3)	0.00±0.08(4)	0.01±0.08(3)	0.01±0.08(12)	0.13±0.06(3)	0.01±0.10(11)	0.05±0.15(2)	-0.01±0.06(21)	0.02±0.09(7)	-0.04±0.06(12)
WASP-43	...	...	...	...	-0.08±0.10(2)	0.19±0.12(3)	-0.10±0.10(9)	...	0.13±0.22(3)	0.09±0.16(3)	0.08±0.15(12)	-0.06±0.18(3)	0.31±0.09(10)
WASP-54	-0.15±0.04(3,s)	...	-0.11±0.05(3,s)	-0.22±0.05(4)	-0.19±0.08(4)	-0.06±0.06(3)	-0.10±0.10(11)	-0.13±0.12(2)	-0.01±0.08(14)	-0.07±0.09(3)	-0.10±0.06(19)	-0.05±0.12(7)	-0.09±0.09(8)
WASP-60	0.19±0.03(3,s)	...	0.34±0.15(s)	0.20±0.07(4)	0.19±0.09(4)	0.14±0.09(3)	0.24±0.08(11)	0.25±0.16(3)	0.24±0.08(13)	0.19±0.13(3)	0.18±0.06(20)	0.18±0.10(6)	0.17±0.08(10)
XO-2N	0.40±0.04(3,s)	0.31±0.21(s)	0.40±0.15(s)	0.48±0.03(2)	0.40±0.11(4)	0.46±0.06(2)	0.45±0.08(10)	0.50±0.04(3)	0.37±0.12(9)	0.49±0.17(3)	0.46±0.09(20)	0.49±0.09(6)	0.46±0.07(12)
XO-2S	0.37±0.05(3,s)	0.26±0.21(s)	0.38±0.15(s)	0.45±0.02(2)	0.37±0.11(4)	0.38±0.07(2)	0.44±0.07(12)	0.54±0.03(3)	0.33±0.12(9)	0.42±0.17(3)	0.36±0.06(20)	0.41±0.10(6)	0.33±0.07(12)

Name	[Cr i/H] (dex)	[Cr ii/H] (dex)	[Mn/H] (dex)	[Co/H] (dex)	[Ni/H] (dex)	[Cu/H] (dex)	[Zn/H] (dex)	[Y/H] (dex)	[Zr/H] (dex)	[Ba/H] (dex)	[La/H] (dex)	[Nd/H] (dex)	[Eu/H] (dex)
							Elements with Z > 23						
HAT-P-3	0.40±0.10(13)	0.40±0.12(6)	...	0.41±0.10(5)	0.37±0.08(37)	0.29±0.10(1)	0.25±0.10(3)	0.24±0.08(5)	0.33±0.05(3)	0.18±0.07(2)	0.42±0.08(2)	0.20±0.09(3)	0.41±0.08(1)
HAT-P-4	0.26±0.07(15)	0.28±0.06(6)	0.18±0.06(3)	0.30±0.07(5)	0.28±0.09(45)	0.21±0.12(4)	0.22±0.09(3)	0.30±0.09(6)	0.20±0.07(3)	0.38±0.08(2)	0.37±0.08(2)	0.28±0.02(2)	0.19±0.08(1)
HAT-P-12	-0.20±0.11(10)	0.14±0.09(1)	-0.30±0.04(2)	-0.19±0.07(4)	-0.29±0.10(40)	-0.38±0.15(2)	-0.28±0.05(3)	-0.42±0.10(3)	-0.27±0.07(1)	-0.38±0.09(2)	0.08±0.11(1)	-0.15±0.18(2)	0.02±0.03(1)
HAT-P-14	0.01±0.07(12)	0.02±0.09(6)	-0.13±0.06(2)	0.08±0.12(2)	-0.02±0.08(33)	0.08±0.13(3)	-0.15±0.08(3)	0.11±0.09(5)	0.16±0.06(3)	0.36±0.06(2)	0.04±0.06(2)	0.16±0.06(2)	...
HAT-P-15	0.31±0.06(14)	0.32±0.09(6)	0.38±0.04(3)	0.26±0.09(5)	0.33±0.08(43)	0.34±0.11(6)	0.35±0.11(3)	0.34±0.11(6)	0.26±0.06(3)	0.31±0.09(2)	0.26±0.06(2)	0.18±0.06(3)	0.25±0.08(1)
HAT-P-17	0.08±0.08(15)	0.08±0.08(6)	0.12±0.08(3)	0.04±0.09(5)	0.05±0.08(43)	0.08±0.11(2)	0.06±0.06(3)	-0.03±0.09(5)	0.07±0.07(3)	-0.02±0.07(2)	0.06±0.08(2)	-0.02±0.06(3)	0.14±0.09(1)
HAT-P-18	0.19±0.10(11)	0.30±0.07(3)	...	0.06±0.10(5)	0.12±0.09(37)	0.03±0.13(2)	0.06±0.05(3)	0.05±0.11(4)	0.03±0.18(2)	0.06±0.07(2)	0.30±0.14(2)	0.14±0.13(3)	...
HAT-P-20	0.34±0.11(9)	0.56±0.07(3)	...	0.35±0.10(4)	0.27±0.09(31)	0.33±0.11(1)	0.27±0.05(2)	0.24±0.13(2)	0.15±0.07(1)	0.14±0.08(2)	...	...	...
HAT-P-21	0.07±0.06(15)	0.05±0.07(6)	-0.04±0.06(3)	0.07±0.08(5)	0.03±0.08(46)	0.07±0.13(4)	-0.06±0.07(6)	-0.06±0.07(6)	-0.06±0.09(3)	0.12±0.06(2)	0.15±0.04(2)	0.19±0.02(1)	0.32±0.05(1)
HAT-P-22	0.34±0.07(13)	0.38±0.12(6)	0.42±0.08(3)	0.34±0.10(5)	0.35±0.08(40)	0.42±0.09(2)	0.37±0.10(3)	0.28±0.11(5)	0.27±0.07(3)	0.29±0.09(2)	0.33±0.06(2)	0.26±0.05(3)	0.19±0.06(1)
HAT-P-26	0.10±0.10(13)	0.13±0.07(5)	0.07±0.07(2)	0.10±0.10(5)	0.07±0.08(42)	0.09±0.13(2)	0.06±0.06(3)	-0.08±0.08(5)	0.18±0.12(3)	-0.04±0.10(2)	0.14±0.12(2)	0.07±0.07(3)	0.38±0.04(1)
HAT-P-29	0.21±0.06(15)	0.21±0.07(6)	0.15±0.06(3)	0.16±0.06(4)	0.19±0.07(46)	0.16±0.11(4)	0.19±0.09(3)	0.27±0.08(6)	0.25±0.07(3)	0.33±0.08(2)	0.37±0.09(2)	0.25±0.03(3)	0.19±0.08(1)
HAT-P-30	0.08±0.08(15)	0.09±0.09(6)	-0.01±0.07(3)	0.10±0.10(2)	0.02±0.07(45)	-0.03±0.12(4)	0.09±0.09(3)	0.13±0.08(6)	0.13±0.05(3)	0.31±0.05(3)	0.13±0.06(2)	0.11±0.05(3)	0.09±0.06(1)
HAT-P-36	0.31±0.06(14)	0.33±0.09(5)	0.31±0.10(3)	0.22±0.10(4)	0.29±0.08(41)	0.24±0.13(4)	0.33±0.22(3)	0.36±0.11(6)	0.36±0.10(2)	0.36±0.10(2)	0.27±0.06(2)	0.20±0.09(2)	0.16±0.09(1)
KELT-6	-0.32±0.07(14)	-0.34±0.06(6)	-0.44±0.05(3)	-0.19±0.09(4)	-0.32±0.06(45)	-0.34±0.12(4)	-0.36±0.05(3)	-0.37±0.07(6)	-0.26±0.04(3)	-0.12±0.08(2)	-0.18±0.11(2)	-0.26±0.06(3)	0.41±0.07(1)
Qatar-1	0.29±0.09(11)	0.45±0.10(3)	...	0.26±0.10(4)	0.23±0.09(38)	0.23±0.15(2)	0.17±0.06(3)	0.04±0.11(3)	0.22±0.07(2)	0.09±0.09(2)	0.36±0.13(1)	0.22±0.14(3)	-0.14±0.05(1)
Qatar-2	0.25±0.12(10)	0.30±0.07(6)	...	0.27±0.10(4)	0.16±0.09(37)	0.25±0.11(2)	...	-0.02±0.14(2)	...	0.07±0.09(2)	...	0.10±0.01(2)	...
TRES-4	0.21±0.07(12)	0.28±0.06(6)	0.19±0.08(3)	0.22±0.07(5)	0.22±0.07(40)	0.21±0.10(4)	0.19±0.08(3)	0.24±0.07(5)	0.25±0.09(3)	0.30±0.09(2)	0.30±0.09(2)	0.22±0.04(3)	...
WASP-10	0.23±0.13(12)	0.49±0.13(6)	...	0.09±0.09(4)	0.18±0.08(38)	0.06±0.11(2)	0.06±0.07(2)	0.19±0.10(3)	0.01±0.03(1)	0.18±0.13(2)	0.21±0.06(1)	0.04±0.02(1)	0.12±0.06(1)
WASP-11	0.15±0.09(12)	0.23±0.07(6)	...	0.11±0.10(5)	0.15±0.09(43)	0.17±0.11(2)	0.15±0.06(3)	0.04±0.12(4)	0.16±0.20(2)	-0.06±0.10(2)	0.13±0.06(1)	0.01±0.12(3)	0.12±0.04(1)
WASP-13	0.08±0.06(15)	0.05±0.06(6)	0.00±0.09(3)	0.08±0.08(4)	0.06±0.07(44)	0.08±0.11(4)	0.09±0.10(3)	0.05±0.08(6)	0.09±0.04(3)	0.21±0.05(2)	0.29±0.04(2)	0.08±0.02(3)	0.12±0.06(1)
WASP-38	0.03±0.06(14)	0.03±0.07(6)	-0.04±0.04(4)	0.08±0.07(4)	0.04±0.07(43)	0.03±0.11(4)	0.07±0.08(5)	0.07±0.08(5)	0.08±0.04(3)	0.19±0.05(2)	0.18±0.10(2)	0.10±0.09(3)	0.00±0.09(1)
WASP-39	0.03±0.07(15)	0.02±0.07(6)	-0.04±0.06(3)	-0.03±0.09(5)	0.00±0.09(46)	-0.05±0.13(4)	0.03±0.10(6)	0.03±0.10(6)	0.00±0.07(3)	0.02±0.09(2)	0.10±0.04(2)	0.00±0.08(3)	0.19±0.05(1)
WASP-43	0.08±0.12(9)	0.04±0.08(1)	...	0.13±0.06(4)	0.05±0.10(28)	0.01±0.13(1)	-0.26±0.09(2)	-0.04±0.08(1)	-0.19±0.04(1)	-0.20±0.07(2)	...	0.14±0.01(1)	0.25±0.08(1)
WASP-54	-0.14±0.07(15)	0.24±0.07(6)	-0.25±0.06(3)	-0.04±0.09(4)	-0.14±0.07(42)	-0.20±0.11(4)	-0.14±0.05(3)	-0.05±0.09(6)	-0.03±0.06(3)	0.16±0.05(2)	0.07±0.06(2)	-0.04±0.03(3)	-0.09±0.09(1)
WASP-60	0.23±0.06(15)	0.24±0.07(6)	0.19±0.09(3)	0.25±0.09(5)	0.22±0.08(46)	0.24±0.12(4)	0.28±0.10(3)	0.26±0.07(6)	0.23±0.04(3)	0.26±0.05(2)	0.29±0.09(2)	0.19±0.06(3)	0.29±0.09(1)
XO-2N	0.46±0.09(13)	0.50±0.12(6)	0.59±0.09(3)	0.49±0.09(5)	0.46±0.09(40)	0.44±0.09(1)	0.44±0.09(3)	0.41±0.11(5)	0.43±0.09(3)	0.38±0.10(2)	0.55±0.06(2)	0.35±0.09(3)	0.40±0.04(1)
XO-2S	0.39±0.08(13)	0.46±0.12(6)	0.54±0.08(3)	0.40±0.08(5)	0.40±0.09(40)	0.41±0.09(1)	0.44±0.10(3)	0.36±0.11(5)	0.33±0.08(3)	0.30±0.08(2)	0.45±0.06(2)	0.23±0.04(3)	0.35±0.04(1)

Table A.3. Stellar kinematic properties as derived in the present work. Columns list the *UVW* velocities, the thick disk-to-thin disk probability, the Galactic eccentricity, the maximum vertical distance above the Galactic plane, and the difference between the mean and the current galactocentric distances.

Name	U (km/s)	V (km/s)	W (km/s)	TD/D	e_G	Z_{max} (kpc)	$\Delta(R_{mean} - R_{GC})$ (kpc)
HAT-P-3	-6.50 ± 0.03	-13.95 ± 0.09	-7.22 ± 0.20	0.01	0.086	0.1783	-0.54
HAT-P-4	3.918 ± 0.18	-30.88 ± 0.18	24.89 ± 0.20	0.04	0.173	0.5305	-1.01
HAT-P-12	-55.42 ± 0.10	-78.87 ± 0.12	-0.63 ± 0.19	3.73	0.404	0.1598	-2.17
HAT-P-14	-9.52 ± 0.09	-2.88 ± 0.18	-7.84 ± 0.13	0.01	0.039	0.1822	-0.15
HAT-P-15	-43.61 ± 0.19	9.03 ± 0.07	6.05 ± 0.05	0.02	0.093	0.1055	0.42
HAT-P-17	57.04 ± 0.08	18.10 ± 0.20	-14.38 ± 0.10	0.05	0.274	0.2545	1.32
HAT-P-18	9.43 ± 0.10	-13.17 ± 0.14	3.91 ± 0.12	0.01	0.121	0.1378	-0.47
HAT-P-20	11.32 ± 0.38	-11.97 ± 0.11	-12.41 ± 0.13	0.01	0.121	0.1811	-0.41
HAT-P-21	4.394 ± 0.11	25.98 ± 0.12	-46.58 ± 0.26	0.52	0.169	1.2478	1.48
HAT-P-22	-26.33 ± 0.14	44.72 ± 0.06	3.10 ± 0.19	0.08	0.221	0.1447	2.27
HAT-P-26	66.50 ± 0.18	-45.10 ± 0.22	-27.74 ± 0.21	0.50	0.351	0.5654	-0.96
HAT-P-29	17.61 ± 0.16	8.99 ± 0.16	7.80 ± 0.05	0.01	0.134	0.1400	0.50
HAT-P-30	-60.33 ± 0.17	9.90 ± 0.14	18.61 ± 0.10	0.05	0.147	0.3742	0.58
HAT-P-36	-24.21 ± 0.07	10.82 ± 0.07	-13.54 ± 0.21	0.02	0.057	0.3996	0.47
KELT-6	-23.49 ± 0.05	25.18 ± 0.07	6.83 ± 0.21	0.02	0.125	0.3533	1.14
Qatar-1	-52.17 ± 0.09	-34.71 ± 0.24	10.76 ± 0.09	0.06	0.207	0.1914	-1.14
Qatar-2	-72.15 ± 0.24	-35.94 ± 0.19	-2.65 ± 0.20	0.11	0.251	0.1810	-1.05
TRES-4	31.47 ± 0.33	-24.06 ± 0.21	0.96 ± 0.16	0.02	0.209	0.2734	-0.70
WASP-10	-14.40 ± 0.05	-1.86 ± 0.19	-11.48 ± 0.10	0.01	0.022	0.1537	-0.11
WASP-11	-11.82 ± 0.18	-3.57 ± 0.16	-15.41 ± 0.18	0.01	0.033	0.2131	-0.16
WASP-13	-14.67 ± 0.15	-9.79 ± 0.10	9.92 ± 0.15	0.01	0.054	0.2485	-0.39
WASP-38	-6.52 ± 0.18	-20.32 ± 0.09	5.40 ± 0.16	0.01	0.117	0.1391	-0.76
WASP-39	-56.70 ± 0.13	10.81 ± 0.05	-31.77 ± 0.16	0.12	0.141	0.6214	0.60
WASP-43	-13.43 ± 0.06	2.92 ± 0.18	-14.20 ± 0.15	0.01	0.023	0.2109	0.09
WASP-54	-5.45 ± 0.13	-15.70 ± 0.13	-7.19 ± 0.20	0.01	0.096	0.2652	-0.59
WASP-60	-50.74 ± 0.46	-38.84 ± 0.28	-5.89 ± 0.19	0.06	0.222	0.2096	-1.28
XO2-N	-87.53 ± 0.19	-78.23 ± 0.25	-2.35 ± 0.12	13.48	0.436	0.1036	-2.01
XO2-S	-87.06 ± 0.19	-78.15 ± 0.24	-2.31 ± 0.11	13.01	0.435	0.1035	-2.01

Note: A positive or negative difference in $\Delta(R_{mean} - R_{GC})$ greater or smaller than $+1/-1$ kpc indicates possible migration from the outer or inner Galactic disk.
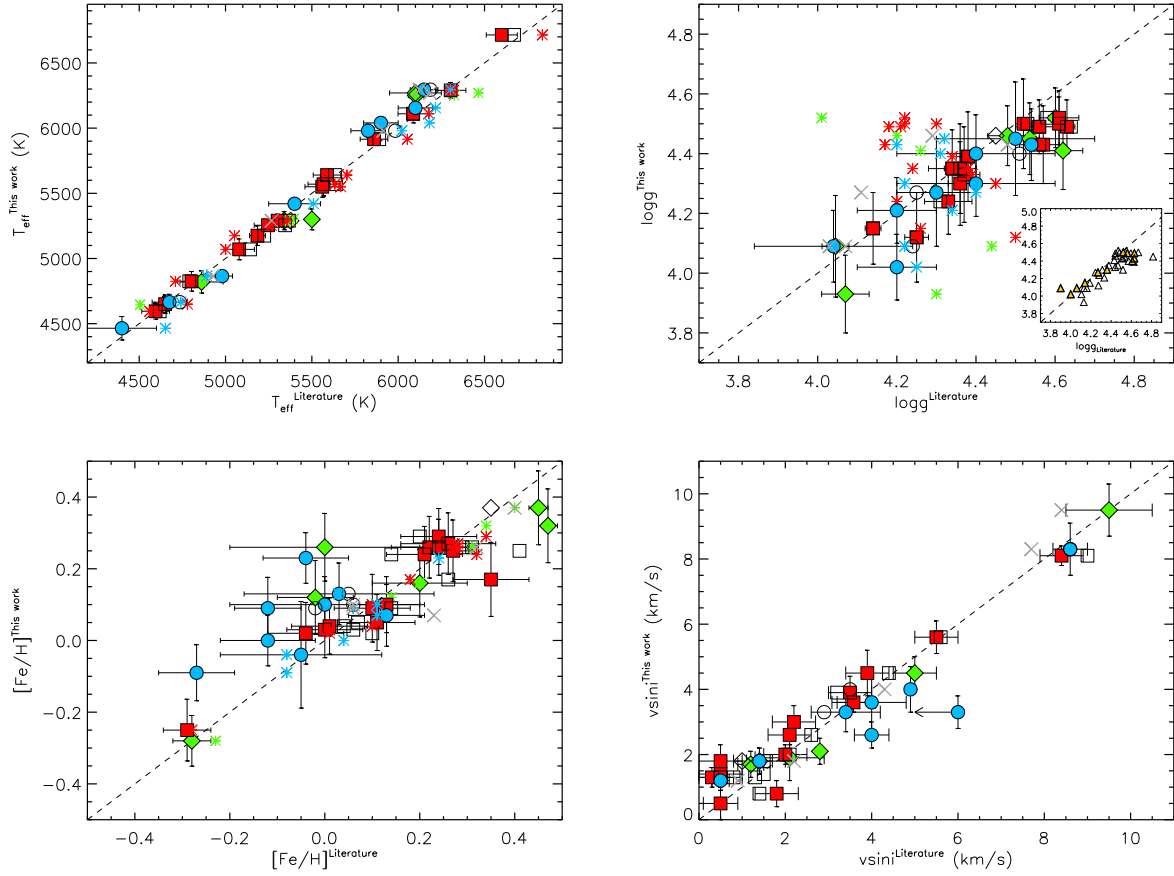
Appendix B: Comparison with previous works

Fig. B.1. Comparison between our stellar parameters ($T_{\rm eff}$, $\log g$, [Fe/H], $v \sin i$) and those from the literature. Filled and open symbols represent the comparisons with the discovery papers and Torres et al. (2012), respectively (squares indicate the HAT-P sample, circles the WASP sample, and diamonds the remaining sample). Asterisks represent the comparison with the SWEET-Cat; in the $\log g$ plot the inset shows the comparison with the measurements obtained with the light curves by Mortier et al. 2013 (filled yellow triangles) or through Gaia parallaxes by Sousa et al. 2021 (open triangles). The crosses indicate the values obtained by Brewer et al. (2016).
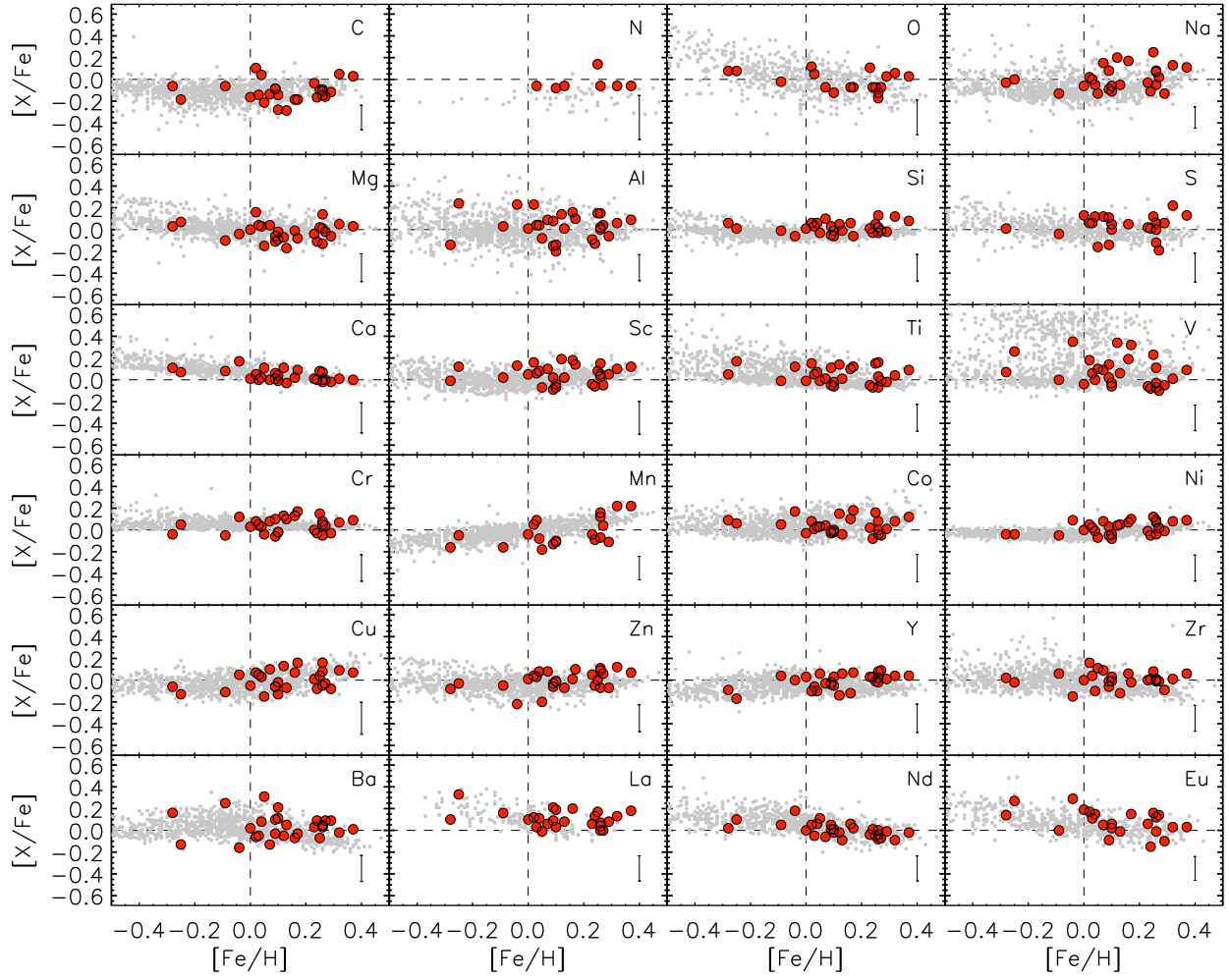
Appendix C: [X/Fe] versus [Fe/H]

Fig. C.1. [X/Fe] vs. [Fe/H] for our sample. See Fig. 4 for the references of the overplotted gray points. The mean error bars are shown at the bottom right of each panel. Solar values are indicated by dashed lines.